University of Padova

Department of Physics and Astronomy "Galileo Galilei"

Master Thesis in Physics

Search for a Josephson-like effect in the ^{116}Sn + ^{60}Ni system

Supervisor
Prof. Daniele Mengoni
University of Padova

Co-supervisor
Dr. Franco Galtarossa
Dr. Lorenzo Corradi

Master Candidate
Giuseppe Andreetta

Student ID
2027582

Academic Year
2022-2023

"The deepest solace lies in understanding this ancient unseen stream, a shudder before the beautiful"
— Tuomas Holopainen of "Nightwish"

Abstract

The pairing interaction, responsible for the two-nucleon correlation, plays a fundamental role in defining the low-energy spectra of atomic nuclei and the properties of their ground state. The effect of pairing correlations in the reaction dynamics can be explored by using heavy-ion reactions, in particular those involving a transfer of few nucleons. In this context, an interesting analogy between the nuclear pairing and the Cooper pairing in superconductors can be investigated through heavy-ion collisions, focusing on nucleon-pair transfer and searching for a possible effect, predicted by a BCS-like theory applied to nuclei: the *Josephson Effect*. The idea was already suggested in the '70s, but only recently more quantitative calculations, assisted by promising experimental results, revived the interest on the subject and ignited a more systematic research. The transfer of neutron Cooper pairs was therefore studied through the interaction between two superfluid nuclei, ^{116}Sn and ^{60}Ni, using the Advances Gamma-Ray Tracking Spectrometer AGATA and the large-acceptance magnetic spectrometer PRISMA at Legnaro National Laboratories, INFN. The work presented in this Master Thesis includes the analysis of the data obtained from the PRISMA magnetic spectrometer and preliminary results for the γ-ray spectra from the AGATA array.

Contents

Listing of figures

Listing of tables

1 Introduction

Correlations due to pairing interaction are a fundamental concept that appears in models of various scientific ambits.

In the nuclear physics framework, this interaction can be seen as a residual strong force acting between couples of nucleons. The resulting pairing correlations play a fundamental role in determining some specific characteristics in nuclei, from the spin-parity of even-even nuclei ($J^\pi = 0^+$) to the increased stability in light neutron-rich nuclei (like Borromean nuclei; e.g. bound ^{11}Li versus unbound ^{10}Li). In particular, two aspects can be highlighted: a structural one, associated to the odd-even mass staggering [11, 12], the energy-level scheme and the nuclear moment of inertia, and a dynamical one, that manifests in the transfer reactions.

In this context, a particular description of pairing leads to very interesting results. In analogy with the condensed matter physics, a Cooper-pair description [13] can be applied to nucleons. In this BCS-like (Bardeen–Cooper–Schrieffer [14]) theory for the nuclear superfluidity, nucleons in time-reversal orbitals ($\boldsymbol{k}\uparrow, -\boldsymbol{k}\downarrow$) are coupled through the pairing interaction in Cooper pairs, analogue to the electron pairs in a superconducting material. As a consequence, one could mention that the nuclear moment of inertia in the ground state (associated to the zero-temperature superfluid state) is about half of the moment of inertia of an ideal rigid quantum rotor. Pair Breaking changes the structure of the nucleus, aligning more and more nucleons to generate higher angular momenta and leading to a phase transition towards a more

rigid moment of inertia [15, 16, 17].

Following the Cooper-pair description, an analogy with the condensed matter physics can be established and a particular effect is predicted to occur, which is the main topic of this thesis work: the nuclear Josephson Effect.

In a system composed of two superconductors separated by a thin insulator, with a thickness smaller than the correlation length of the electrons in the Cooper pair ($\xi \sim 10^4$ Å), a tunneling current, the so-called *supercurrent*, is spontaneously generated. This effect takes the name of *Josephson Effect* (JE) [18]. It follows as a direct consequence of the Ginzburg-Landau theory of superconductivity [19]; more details will be provided in the following sections. In short, since the superconductors are represented as condensate of Cooper pairs (BCS condensation), a single quantum phase can be associated to each of them, and calculations show that the aforementioned supercurrent is related to the variation of the phase difference between the two condensates. This so-called *Josephson phase* enters directly the expression of the current and its derivative over time is proportional to the potential difference V between the two superconductors. In particular, if $V = 0$ a direct current (DCJE) flows from one superconductor to the other, while for $V \neq 0$ an alternate current (ACJE) is developed. In the latter case, since the electrons are moving back-and-forth through the junction, a microwave radiation is emitted.

In analogy [20], one could consider a below-barrier few-nucleon transfer process as a nuclear Josephson junction: the two nuclei represent the superconducting metals, the empty space between them acts as an insulator and the reaction Q-value would be the potential difference. In such a description, Cooper-paired nucleons could be transferred, in principle both in a back-and-forth sequential way and in a simultaneous way, from one nucleus to the other through the barrier, but still preserving their nature of paired nucleons if the distance between the nuclei is around or less than the correlation length. In this way, similarly to the condensed matter case, the emission of an electromagnetic radiation in the form of a dipole distribution is predicted.

In order to better understand the physics behind this phenomenon, a brief explanation of the superconducting Josephson Effect will be given, stressing the relevant quantities and outcomes to make the similarity with the few-nucleon transfer more robust. A simple derivation of the effect can be provided starting from the Ginzburg-Landau theory of superconductivity [19], passing through the Josephson

equations (the original demonstration was given with a slightly different formalism [18]). Finally, the analogy will be explained as suggested in [5].

1.1 The Josephson effect

In his work on superconductivity, Ginzburg applied the more general Landau theory of continuous phase transitions [21] to the transition from the normal conducting to the superconducting regime. The fundamental parameter for this description is the so-called *order parameter*, which in this case assumes the form of a complex parameter

$$\psi(\mathbf{r}) = |\psi(\mathbf{r})|e^{i\phi(\mathbf{r})} \ , \tag{1.1}$$

where $\mathbf{r}$ is the spatial coordinate and ϕ is a gauge phase. From this description, some features of superconducting materials were explained, but without a real microscopic description.

Lately, after the advent of the Bardeen-Cooper-Schrieffer (BCS) theory of superconductivity [14], a microscopic view was given to the effect through the concept of Cooper pair. A Cooper pair is composed by two electrons with opposite momentum and spin ($\boldsymbol{k}\uparrow, -\boldsymbol{k}\downarrow$) coupled through the exchange of phonons with the lattice. This pairing interaction has a characteristic distance, called *correlation length*, beyond which the two electrons cannot be considered coupled anymore. Since the total spin is zero, the pair of electrons can be described as a quasi-boson in the Bose-Einstein formalism. The superconductivity arises from the Bose-Einstein condensation of these quasi-particles.

Gor'kov derived the Ginzburg-theory equations from the BCS theory [22], demonstrating the equivalence of the two descriptions. Therefore, a quantum mechanical interpretation could be given to the Ginzburg-Landau order parameter: it represents the wave function of the Cooper-pairs condensate, with $|\psi(\mathbf{r})|$ carrying the information on the local density of pairs and $\phi(\mathbf{r})$ as quantum phase. More details on the Ginzburg-Landau theory can be found in the Appendix A. For the purposes of the discussion, the microscopic interpretation of the order parameter is sufficient. From this, the Josephson effect can be easily described.

The Josephson Effect (JE) can be derived from the Josephson equations, which describe two superconductors separated by a thin insulator and with a potential

difference V, as already mentioned above. The insulator acts as potential barrier for the carriers and its thickness must be smaller than the correlation length of the electrons inside the superconductors: in this way, the two partners of the Cooper pair remain correlated even if one of them passes through the barrier. In superconducting materials, the correlation length turns out to be around 10^4 Å. Labelling the two superconductors as A and B, the order parameters will be

$$\psi_A = |\psi_A| e^{i\phi_A(\mathbf{r})} = \sqrt{n_A} e^{i\phi_A(\mathbf{r})} \qquad \psi_B = \sqrt{n_B} e^{i\phi_B(\mathbf{r})} \ . \tag{1.2}$$

In fact, the Josephson equations are nothing but the Schrödinger equations for a system made up by two subsystems, described by the aforementioned order parameters and interacting with each other through a coupling K:

$$i\hbar\partial_t \begin{pmatrix} \sqrt{n_A} e^{i\phi_A(\mathbf{r})} \\ \sqrt{n_B} e^{i\phi_B(\mathbf{r})} \end{pmatrix} = \begin{pmatrix} eV & K \\ K & -eV \end{pmatrix} \begin{pmatrix} \sqrt{n_A} e^{i\phi_A(\mathbf{r})} \\ \sqrt{n_B} e^{i\phi_B(\mathbf{r})} \end{pmatrix} \ . \tag{1.3}$$

With some manipulations and with the definition of the Josephson phase as the phase difference between the two superconductors, namely

$$\varphi = \phi_B - \phi_A \ , \tag{1.4}$$

a simple set of equations is left:

$$\begin{cases} \dot{\sqrt{n_A}} = \frac{2K\sqrt{n_A n_B}}{\hbar} \sin\varphi \\ \dot{\phi}_A = -\frac{1}{\hbar}\left(eV + K\sqrt{\frac{n_B}{n_A}} \cos\varphi \right) \end{cases} \qquad \begin{cases} \dot{\sqrt{n_B}} = -\frac{2K\sqrt{n_A n_B}}{\hbar} \sin\varphi \\ \dot{\phi}_B = \frac{1}{\hbar}\left(eV - K\sqrt{\frac{n_B}{n_A}} \cos\varphi \right) \end{cases} \ . \tag{1.5}$$

As visible from Eq.s 1.5, both the carrier density and the phase of each superconductor depend on the Josephson phase. In practice, a single phase is sufficient to describe the system. Now, by using its definition, the time derivative of the Josephson phase becomes

$$\dot{\varphi} = \dot{\phi}_B - \dot{\phi}_A = \frac{2eV}{\hbar} \ . \tag{1.6}$$

In this way it is possible to see how the phase evolves with time. Noteworthy is the fact that the energy difference due to the presence of Cooper pairs is $\Delta E = 2eV$.

The variation of the phase induces also a variation of the carriers concentrations ($\dot{\sqrt{n_A}}$ and $\dot{\sqrt{n_B}}$), which can be seen in terms of currents, namely the *supercurrent*. Therefore the current flowing across the junction can be written as

$$I(t) = I_C \sin \varphi(t) \ , \tag{1.7}$$

where I_C is called *critical current*. Interesting features can be extracted from these results, see Appendix A for more details. The most important outcome is that a tunneling current develops spontaneously when the two superconductors are separated by the insulating barrier only due to this phase difference and to the coupling, no matter how weak it is.

The two most known effects come from two particular cases: $V(t) = 0$ (Direct Current Josephson Effect, DCJE) and $V(t) = V_0$ (Alternating Current Josephson Effect, ACJE). In the first case, being $V = 0$, the Josephson phase is kept constant ($\dot{\varphi} = 0$), so the total effect is a direct current flowing between the two superconductors. In the second case, there is a linear variation of the phase, which produces an alternating sinusoidal supercurrent. It is worth to underline that this effect is entirely due to the kinetic energy of the carriers.

This description applies for the electrons, but already in the '60s Bohr, Mottelson and Pines noticed a similarity between the excitation spectra of superconducting metallic states and those of nuclei [11]. The first real analogy between the JE in superconductors and the nucleon-pair transfer was suggested by Klaus Dietrich in the '70s [20]. His investigation was based on the previous work of Gol'danski and Larkin [23], who studied the enhancement of the cross-section in the pair transfer at lowest order in perturbation theory, and the one by Gaudin [24], which discussed the possibility of vibrations of nuclear pairs between two interacting nuclei in a time-independent description of the junction. The main result of Dietrich's semi-classical treatment was that, in a reaction between superconducting nuclei, taking into account the time dependence of the potential wells position, the transfer of a pair of nucleons in time-reversal conjugate states is considerably enhanced compared to the transfer of two uncorrelated nucleons.

In order to better explain this particular effect and its consequences, an introduction to nuclear force and pairing is given in the next Section, followed by key concepts relevant in transfer reactions.

1.2 Nuclear structure and pairing

As already mentioned, the pairing interaction manifests itself both structurally and dynamically. From the structural point of view, the pairing is added as residual interaction, along with the quadrupole (and more recently also higher multi-polarity) interaction. In particular, it enters the H_{res} correction term of the nuclear Hamiltonian

$$H = H_0 + H_{res} \ , \tag{1.8}$$

where H_0 comes from the single particle Hamiltonian for each nucleon moving in an average nuclear potential, typically described with an harmonic oscillator potential or a Wood-Saxon potential.

From H_0, by adding some corrections like the spin-orbit term and then solving the Schrödinger equations for the nucleons moving in this potential, the shell model can arise with all its quantum mechanics features. Clearly, this description is accurate only for very specific cases, near the so-called *doubly-magic nuclei*: here, the orbitals are fully occupied and therefore the single particle features are dominant when adding or subtracting few nucleons. Moving away, opening more shells and adding more nucleons, the residual interactions become more and more significant and crucial in determining some characteristics of nuclei. As already mentioned, the spin-parity of even-even nuclei, the value of the nuclear moment of inertia and the more general odd-even staggering in isotopic masses can be reproduced through the pairing interaction.

For the thesis purpose, only the pairing will be addressed, since it is the interaction responsible for the Cooper pairs formation.

The pairing interaction can be phenomenologically described through a combination of δ functions with a pairing coupling constant G, which experimentally is around $17/A$ MeV for protons and $25/A$ MeV for neutrons. The general matrix element is expressed in Eq. 1.9 [25].

$$\langle j_1 j_2 J | \, V_{Pairing} \, | j_3 j_4 J' \rangle = -G \left(j_1 + \frac{1}{2} \right) \left(j_3 + \frac{1}{2} \right) \delta_{j_1 j_2} \delta_{j_3 j_4} \delta_{J0} \delta_{J'0} \ . \tag{1.9}$$

The matrix element shows how pairs of particles can interact through pairing: the individual angular momenta must be the same for each partner in the pair state

$|j_a j_b J\rangle$ with $(a, b) = (1, 2)$ or $(3, 4)$, and the total angular momentum J of the pair must be zero, therefore favouring spherical shapes for nuclei. In particular, from the diagonal matrix elements, when $j_1 = j_3$, we obtain the energy associated to the pair of identical nucleons in a well defined state.

However, not only diagonal elements are non-zero. The off-diagonal terms couple states of nucleon pairs belonging to different shells, scattering these pairs from one orbit to the other if the energy gap is compatible with the pairing matrix element. In order to quantify the effect of the pairing on the nucleus, a simple 2-level model can be used [26]. Let us consider two single-particle levels associated to occupied and empty states. Let us then assume them to be degenerate with equal degeneration $\Omega = (2j + 1)/2$ and separated by an energy ΔE. The interplay between pairing correlations and shell effects is measured by the parameter

$$x = \frac{2G\Omega}{\Delta E} \,. \tag{1.10}$$

The magnitude of x can distinguish normal nuclei, where the shell effects are dominant ($x < 1$), from superfluid nuclei, where the coupling due to pairing overcomes the shell structure ($x > 1$).

Finally, a possible description of how the pairing interaction works in building the superfluid structure of a nucleus, within the quantum field theory landscape, is through the surface vibrations: the interaction between a nucleon and the nuclear surface sets a virtual vibration, which is then reabsorbed when another nucleon interacts with the excited surface. In this picture, the similarity with the superconducting coupling of electrons is even more visible, since the surface interaction would play the role of the phonon exchange with the lattice.

The second aspect we want to address is the dynamical one, that can be mainly seen in the 2-nucleon transfer reaction. This kind of reactions is well known to be very sensitive to pairing effects, especially for the neutron-neutron and the proton-proton pairing correlations. For example, direct reactions with light nuclei, like (p, t) and (t, p), are typically "smoking guns", since they involve very few nucleons and present clean reaction channels. Also *pn* transfer processes can be used to test the nuclear strong force in the proton-neutron correlations [27]. However, heavy-ion reactions are needed to probe the Josephson effect, since one of the main ingredients is the superfluid nature of the involved nuclei.

The next Section will therefore present a brief summary on heavy-ion reactions in order to show how pairing correlations can affect the dynamics of these processes.

1.3 Heavy-ion reactions and transfer process

Heavy-ion collisions are an important tool to probe the nuclear structure and to investigate the strong force at the nuclear level. The variety of reactions arising from these collisions is huge, changing as a function of the total energy in the center of mass E^* and the impact parameter b. In particular, the last quantity represents the minimum distance between the colliding nuclei if the trajectories were straight lines and it contributes to the total angular momentum of the reaction. Nuclear reactions can therefore be divided in different groups depending on E^* and b, from Coulomb Excitation and Peripheral interactions to Deep Inelastic Scattering and Fusion-Fission, just to mention some of them. An example of this zoology is shown in Fig. 1.1.

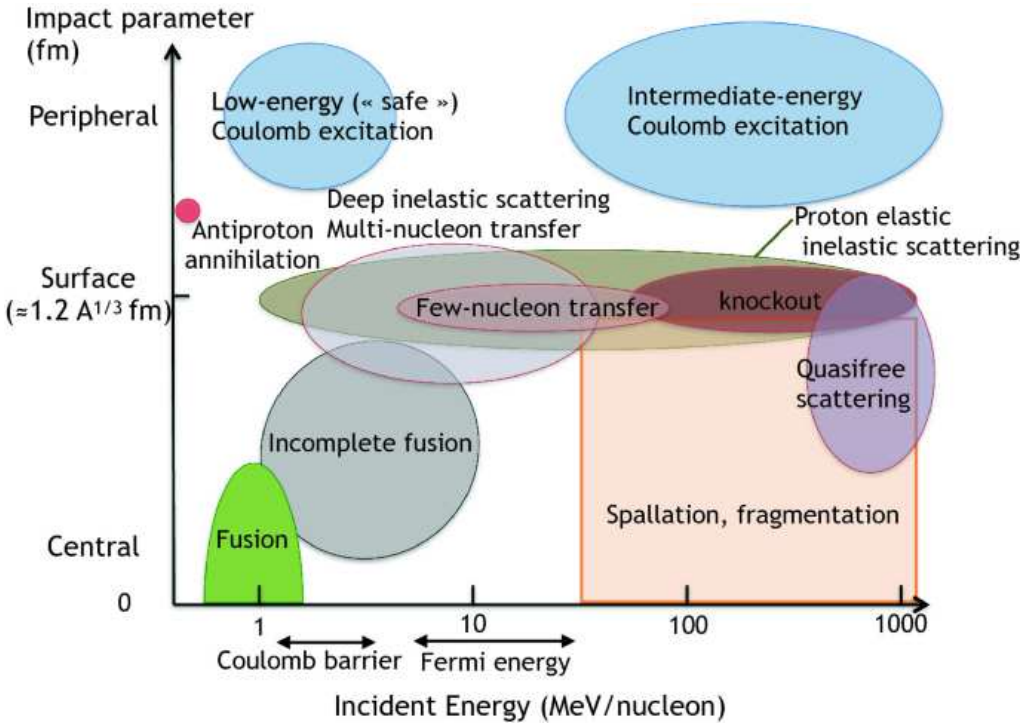

Figure 1.1: Different types of nuclear reactions in the energy - impact parameter space. Taken from [1].

Regarding the transfer process, a full quantum mechanical approach would be needed to describe the reaction in all its details. For example, a DWBA (Distorted Wave Born Approximation [28]) approach can be exploited, using an effective interaction potential. The nuclear interaction potential can be assumed as made up by three main components: the Coulomb potential, the purely nuclear potential and the centrifugal potential. The effective potential seen by a colliding nucleus in the *projectile+target* reaction is

$$V_{eff} = V_C(r) + V_n(r) + V_l(r) \tag{1.11}$$

$$= \hbar c \alpha \frac{Z_{proj} Z_{targ}}{r} + \frac{V_0}{1 + \exp\left[\frac{r-(R_{proj}+R_{targ})}{a}\right]} + \frac{l(l+1)\hbar^2}{2\mu r}\,, \tag{1.12}$$

where $R_i \simeq 1.2\, A_i^{1/3}$ is the nuclear radius, a the diffuseness of the nuclear matter, related to the surface broadening of the nucleus, l is the angular momentum quantum number and $\mu = \frac{A_{proj} A_{targ}}{A_{proj}+A_{targ}}$ is the reduced mass of the system. In this case, the nuclear potential is described with a Wood-Saxon shape, with a depth V_0 which typically ranges from 35 to 50 MeV. The combination of these three components generates the interaction potential that another nucleus sees impinging on the first one, in particular in the form of a potential barrier (Fig. 1.2).

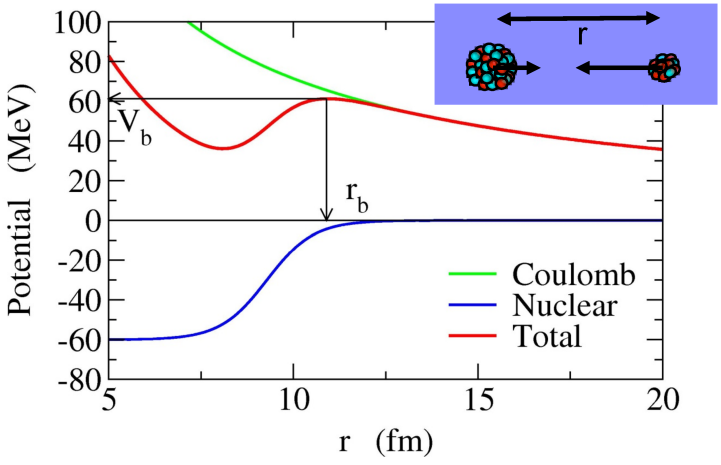

Figure 1.2: Schematic representation of the interaction potential between two colliding nuclei. Taken from [2].

Luckily, under some assumptions, a semi-classical approach can be used, in par-

ticular assuming the classical Rutherford scattering trajectory: by matching the entrance and exit trajectories, with the conservation of the total angular momentum and by using Newton's Second Law of Motion and the Coulomb's law, a simpler description can be obtained. Two relevant quantities are the *optimum Q-value* and the *distance of closest approach*.

In the reaction $a(= b + d) + A \longrightarrow b + B(= A + d)$,

$$Q_{opt} = \left(\frac{Z_d}{Z_A} - \frac{Z_d}{Z_b}\right) E_B + \left(\frac{m_d}{m_b} - \frac{m_d}{m_A}\right)(E^* - E_B) + \frac{m_d \ddot{r}_0}{m_a + m_A}(R_A m_b - R_a M_B) \ , \quad (1.13)$$

where m_d and Z_d are mass and charge of transferred particle, b and A are the cores of the involved nuclei, r_0 is the relative distance, R_i is the nucleus position, E_B is the Coulomb barrier and E^* the relative approaching energy of the colliding nuclei. The optimum Q-value corresponds to the kinematic conditions in which the cross section for the transfer reaction, and therefore its probability to occur, is higher. We talk about *Q-value matching* when the effective Q-value of the reaction is close to the optimum value (Eq. (1.14)):

$$Q = Q_{gg} - E_X \simeq Q_{opt} \ , \quad (1.14)$$

where the Q_{gg} represents the ground state-to-ground state reaction Q-value and E_X is the excitation energy of the reaction products. In such cases, the transitions that populate states at the given E_X are favoured.

The distance of closest approach is instead

$$D(\theta^*) = a_0\left(1 + \csc\frac{\theta^*}{2}\right) , \qquad 2a_0 = \frac{Z_1 Z_2 e^2}{4\pi\epsilon_0 E^*} \ , \quad (1.15)$$

where $2a_0$ is basically the distance in the pure Coulomb head-on collision and the modulation factor with the scattering angle in the center of mass frame θ^* describes the hyperbolic Rutherford trajectory. E^* is the same as in Eq. (1.13).

In this framework, also the cross-section assumes a simplified form, as shown in Eq. (1.16).

$$\frac{\mathrm{d}\sigma}{\mathrm{d}\Omega} = P_{tr}\left(\frac{\mathrm{d}\sigma}{\mathrm{d}\Omega}\right)_{Ruth} \quad (1.16)$$

The differential cross-section has the same form as in the Rutherford scattering,

corrected by a factor that accounts for the nucleon transfer, called *transfer probability* P_{tr}. This parameter contains the overlap of the wave-functions associated to the initial and final states. Most of the multi-nucleon transfer reactions can be described with a very simple model [29], considering the whole process as a combination of independent single-particle transfers. Therefore the probability factor follows a binomial distribution

$$P_{xN} = \binom{A}{x} p^x (1-p)^{A-x} \,, \tag{1.17}$$

where x is the number of transferred nucleons, A is the total number of available particles and p is the transfer probability for the single nucleon, which can be considered constant for all the nucleons in first approximation.

In the limit of transfer reactions below the Coulomb barrier, the transfer probability assumes a particular form. The process occurs as a tunneling effect of the nucleon from one nucleus to the other, described as potential wells, and it is useful to write the probability factor taking into account the penetrability of the barrier. The transfer probability can be therefore expressed as

$$P_{tr} \sim e^{-2\alpha D} \,, \qquad \alpha = \sqrt{\frac{2mB}{\hbar^2}} \,, \tag{1.18}$$

where D is the distance of closest approach and α is a parameter containing the information on the binding energy B of the nucleon inside the nucleus. Finally, m is the mass of the transferred particle.

Clearly, the transfer probability will change accordingly to the number of exchanged nucleons also in the below-barrier multi-nucleon transfer reaction. In particular, for the purposes of the present work, the 2-nucleon transfer case is addressed. Here, if no correlation is present, or in other words, if the process can be described as a combination of two completely independent single-particle transfer processes, the probability becomes

$$P_{2N} = P_{1N}^2 \,. \tag{1.19}$$

Typically, only the sequential transfer of uncorrelated particles contributes to the cross section of the reaction. Indeed, the theory that describes the transfer reactions shows that the cross section contains three main components: the sequential

transfer, the simultaneous pair transfer and the non-orthogonality correction term. At the lowest perturbation order, the last two terms cancel out completely [26, 30]. A possible interaction that provides correlations between particles will enhance the transfer, the second nucleon following the first one profiting of this correlation, introducing a non-negligible contribution from the simultaneous pair transfer mechanism. The result is therefore an enhancement of the differential cross-section, associated to an increase of the transfer probability. Eq. (1.19) has to be corrected and replaced with

$$P_{2N} = EF \cdot P_{1N}^2 \ , \tag{1.20}$$

where EF represents the enhancement factor. This increase in the cross section was experimentally observed by Montanari et al. in a 2-neutron transfer reaction [31].

Now, the role of this interaction was recently claimed to be played by the Cooper-pair correlation in superfluid nuclei, at least in a certain range of distances between nucleons. The idea was suggested by R.A. Broglia in the last few years. Keeping the analogy of weak binding of electron Cooper pairs in superconducting materials, from uncertainty-principle arguments, a correlation length can be defined as

$$\xi = \frac{\hbar v_F}{\pi \Delta} \ , \tag{1.21}$$

where v_F is the particle velocity at the Fermi surface and Δ is the so-called *pairing gap*, which typically goes as $\Delta \simeq 12 \cdot A^{-1/2}$ MeV, with values between 1 and 2 MeV for medium mass nuclei. The experimental values are shown in Fig. 1.3. The number 3 in superscript in the figure indicates that the pairing gap is computed using 3 terms: the binding energy of the nucleus (Z, N) and the binding energies of its neighbours $(Z, N \pm 1)$. Due to the weak binding, ξ is typically larger than nuclear dimensions. This peculiarity allows the two members of a Cooper pair to move between target and projectile, essentially as a whole, both in the simultaneous and successive transfer mechanisms. At this point, the analogy with superconductors will suggest the generation of the supercurrent and the associated dipole emission in the case of ACJE, similarly to what occurs in the condensed matter case.

The enhancement of the 2-nucleon transfer reaction mentioned above, and in particular the possibility to have $P_{2n} \sim P_{1n}$ at energies near the barrier and distances of closest approach around the correlation length ξ, sets the system in the best condition to observe this possible dipole emission spectrum. Indeed, such condition

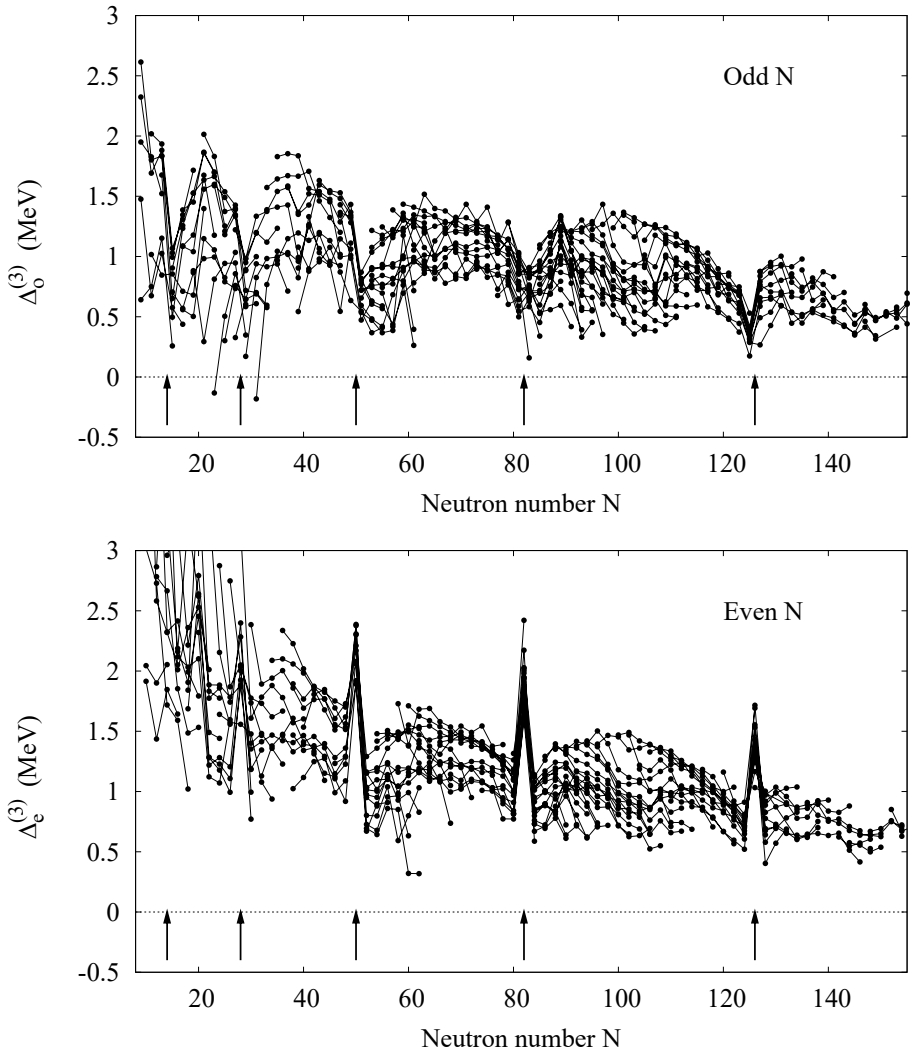

Figure 1.3: Pairing gap for nuclei with odd and even number of neutrons. Data can be found in [3].

on the transfer probabilities would mean that for the system the single-neutron transfer and the paired-neutron transfer are more or less equally favoured. Then, since the center of mass must stay fixed during the reaction, but a certain quantity of mass (2 nucleons) is moving from one nucleus to the other, the overall effect is that the charge distribution slightly moves. In particular, the center of charge motion is the responsible of the predicted dipole oscillation spectrum. In principle, the motion of the center of charge occurs in most of the cases when dealing with nuclear reactions, but the JE should favor this emission, because during the collision

time ($\sim 10^{-21}$ s) the nucleons could be transferred back and forth (instead of the typical one-way trip) a number of times thanks to the superfluid nature of the system.

1.4 The experiment

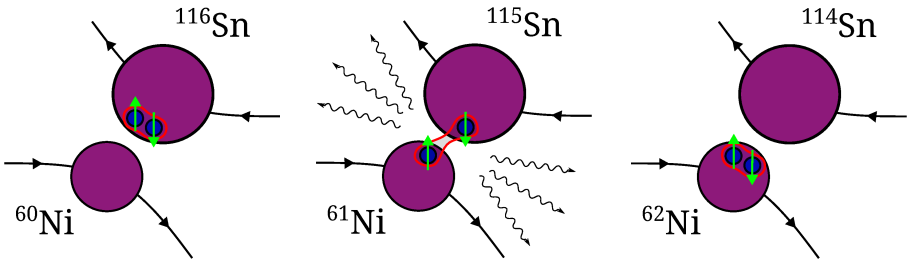

Figure 1.4: Sketch of the reaction process with the dipole emission.

In order to observe experimentally the nuclear JE, a system fulfilling a set of specific requirements must be chosen. Just to mention few of them, a sufficiently large correlation length is needed in combination with a sufficiently small distance of closest approach, but in any case avoiding that the nuclei touch each other. Moreover, the effect is predicted to occur in presence of superfluid nuclei and it is most likely to happen when the probability of two-nucleon transfer is comparable with the probability of single-nucleon transfer, indicating the presence of a correlation between the paired nucleons.

The ^{116}Sn + ^{60}Ni system matches all the conditions above (a sketch of the reaction is shown in Fig. 1.4). It is a well Q-value matched system, being the ground-to-ground Q-value of the $1n$- and $2n$-transfer reactions close to the optimum Q-value. Indeed, the ground-state-to-ground-state Q-values are respectively $Q_{1n} = -1.7$ MeV and $Q_{2n} = +1.3$ MeV, while the optimum Q-value (Eq. (1.13)) is around 0 MeV for both the channels. In particular, these values are below the 2Δ threshold, meaning that the energy at disposal is not sufficient to break the first pair. We can therefore say that the system presents a good Q-value matching and this means that the transfer strength is concentrated to the ground state. This kind of reaction is also known as *cold transfer*. In addition, the two nuclei are known to manifest superfluid characteristics: they both have a proton closed shell (magic numbers $Z = 28$ and

$Z = 50$) and neutrons in the middle of the shell, in particular in closed subshells and therefore always coupled in orbitals with opposite angular momentum, and moreover the first 2^+ excited state is almost at the same energy for each isotope, revealing a collective nature associated to pairing. The Sn isotopic chain is a famous example [32]. Indeed, the pairing interaction scatters couple of nucleons over several shells if the spacing between them is comparable to the pairing matrix element of the transition, modifying the Fermi surface of the nucleus. From a more quantitative point of view, the x parameter (Eq. 1.10) for both Sn and Ni is greater than 1, meaning that the pairing dominates over the shell effects. The neutron correlation length for this system is calculated to be 13.6 fm [5].

As mentioned above, in a previous paper by Montanari et al. [31], indications of neutron correlation were observed. This reaction was studied at LNL almost ten years ago: comparing the transfer probabilities for the $1n$- and $2n$-transfer channels (^{116}Sn + ^{60}Ni $\longrightarrow$ ^{115}Sn + ^{61}Ni and ^{116}Sn + ^{60}Ni $\longrightarrow$ ^{114}Sn + ^{62}Ni), a general enhancement was found for the $2n$-transfer and in particular, at a distance of closest approach of about 13.5 fm, the two transfer probabilities were within the same order of magnitude. This was interpreted as a fingerprint of correlation between neutrons. In Fig. 1.5 the transfer probability P_{tr} for the single-particle and for the 2-particle transfer reaction is shown as a function of the distance of closest approach D with the theoretical prediction. This enhancement was the main experimental result that motivated the proposal for the search of the Josephson Effect. For this reason, the experiment performed at LNL in February 2023 [33], topic of this thesis, was carried out in the same experimental conditions as in [31]. An important goal of this thesis will be to ensure that the current experimental results are compatible with the previous ones.

A beam of ^{116}Sn was delivered by the PIAVE-ALPI accelerator at the energy of 460 MeV, with a nominal intensity of 1.5 pnA and a +20 charge state. The energy of the beam had an uncertainty of $\sim 1.5\%$. The ^{60}Ni targets had a thickness of 100 μg/cm^2 and 200 μg/cm^2, with a carbon backing (but actually put on the upstream face of the target) of 20 μg/cm^2. The presence of the carbon foil provided the structural solidity for the target and gave also the opportunity to control the target status through the observation of the Rutherford-scattered carbon ions with a silicon detector.

For this particular system, at distances of closest approach sufficiently small,

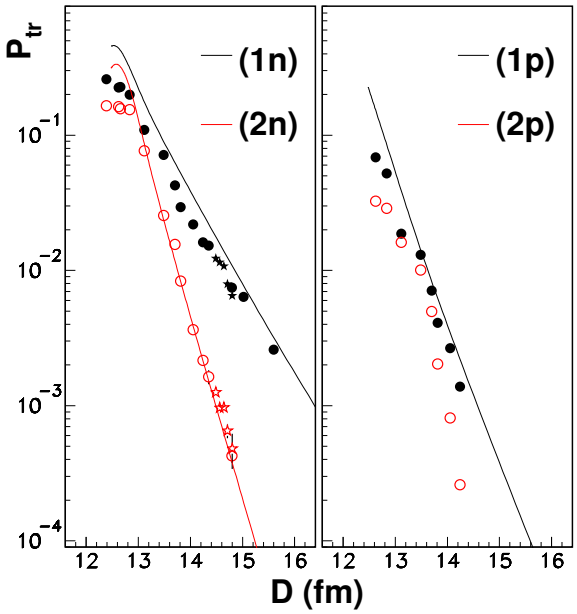

Figure 1.5: Transfer probability as a function of the distance of closest approach for the $1n$-, $2n$-, $1p$- and $2p$-transfer channels in the ^{116}Sn + ^{60}Ni reaction. The theoretical calculations, that include the pairing interaction at the microscopic level, are represented by the lines. Taken from [4].

calculations in [5] predict that the two neutrons could go back and forth from 2 to 3 times during the transfer, leading to a particular dipole emission γ-ray strength. This distribution is predicted to be peaked around 4 MeV with a large width, as shown in Fig. 1.6. In order to see this dipole emission, the AGATA γ-ray tracking array [9, 34] was employed, coupled to the large acceptance magnetic spectrometer PRISMA [10, 35]. The entrance window of PRISMA was placed at 20° with respect to the beam direction, as in [31], in order to reproduce the conditions to observe again the transfer probability enhancement. In particular, we wanted to obtain again the $P_{2n} \sim P_{1n}$ condition, associated to a distance of closest approach between 13.2 and 13.6 fm. Indeed, such distance should be close to the correlation length of neutrons in the studied system and therefore, if the Cooper-pair description is valid, the γ-ray emission should be favoured. The substantial difference from the previous experiment was the presence of the AGATA array, placed in the opposite direction with respect to PRISMA, at backward angles, that allowed the detection

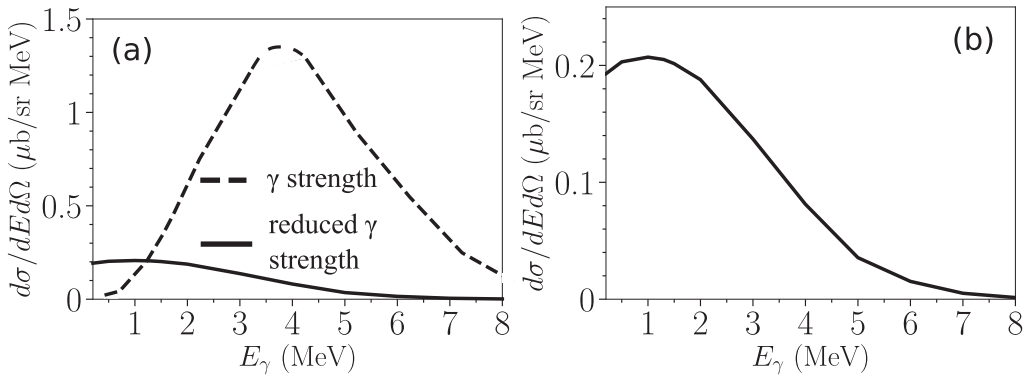

Figure 1.6: Predicted γ strength (a) and reduced γ strength (b), i.e. the γ strength divided by the phase-space factor. Taken from [5].

of the emitted γ-rays.

The aim of this thesis is therefore to analyze the data from this recent experiment, focusing on the transfer probabilities and on the γ-ray spectra in the two main channels of interest, namely the single-neutron transfer and the 2-neutron transfer, taking the elastic+inelastic channel as reference.

1.5 Outline

In this general introduction, the theory on the Josephson effect in the physics of superconductors case was presented and the role of pairing correlations in the creation of Cooper pairs of nucleons was addressed. A phenomenological description of the nuclear pairing interaction was included, as well as its effect on few-nucleon transfer reactions. In the next Chapter, the employed set-up will be described, with particular emphasis on the large acceptance PRISMA magnetic spectrometer. In Chapter 3 the calibration of the several detectors will be explained and the analysis of data from PRISMA and AGATA will be shown. Finally, in Chapter 4 the main results of this work will be presented: the mass distributions and identified γ-ray transitions will be shown, and the obtained transfer probabilities will be compared with the data coming from a previous experiment done on the same system. The conclusions will be exposed in Chapter 5.

2

Set-up

The experiment described in this thesis was performed at the INFN Legnaro National Laboratory (LNL), Italy, in February 2023, and took two weeks of data acquisition. As already mentioned, the ^{116}Sn beam impinged on several targets of ^{60}Ni with a carbon fronting. The experimental setup was composed of the PRISMA magnetic spectrometer, shown in Fig. 2.2, placed at 20° with respect to the beam direction, and the AGATA tracking array, positioned on the opposite side of PRISMA, facing the target. On the same support structure of the AGATA crystals, a set of lanthanum bromide ($LaBr_3$) scintillators was mounted. Finally, in the scattering chamber, a pin silicon detector was placed at 55° with respect to the beam line and on the opposite side of PRISMA. In this Chapter, a brief description of the entire set up will be given.

The coupling of AGATA with PRISMA (design of the coupled set-up in Fig. 2.1) represents a very powerful combination, which can exploit the ion identification of PRISMA and integrate this information with the AGATA γ-ray detection, providing the reconstruction of the reaction dynamics. Such detection and reconstruction capabilities are essential for this experiment, since we are dealing with below-barrier transfer reactions, where a large acceptance and a good efficiency are needed to detect low energy ions, and with a particular γ-ray distribution, where the energy resolution and efficiency play a major role in the discrete line identification.

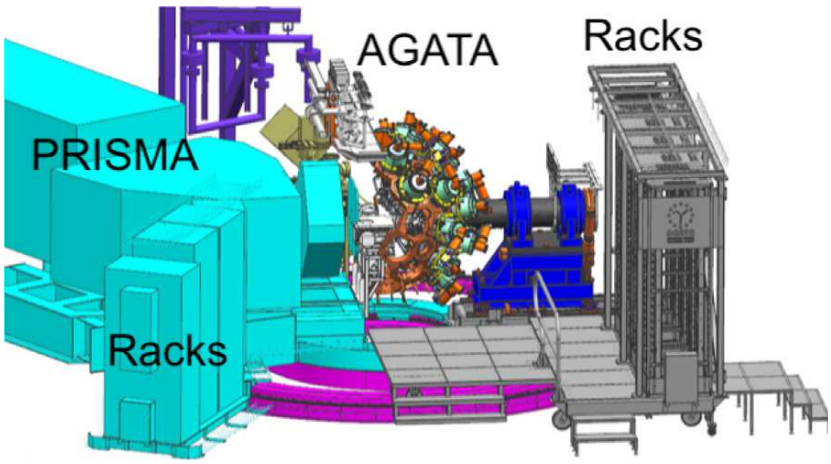

Figure 2.1: Design of the AGATA + PRISMA coupling at LNL. Taken from [6].

2.1 PRISMA

Figure 2.2: Picture of the magnetic spectrometer PRISMA at LNL.

PRISMA is a large acceptance magnetic spectrometer designed for the ion identification in the medium mass range (i.e. $20 < A < 150$) and in the $3 - 10$ MeV/u energy range. It is made up by several stages, which combined together give the information on Time of Flight (TOF), trajectory and energy of the detected particle. In Fig. 2.3 a schematic drawing of the apparatus is shown. In Tab. 2.1 the typical nuclear charge Z, mass A and energy E resolutions are reported. The subdetectors are presented in the following.

Resolution		
Z resolution	$\Delta Z/Z$	1/60
A resolution	$\Delta A/A$	1/300
E resolution	$\Delta E/E$	1/1000

Table 2.1: Typical values for Z, A, and E resolutions. Taken from [10].

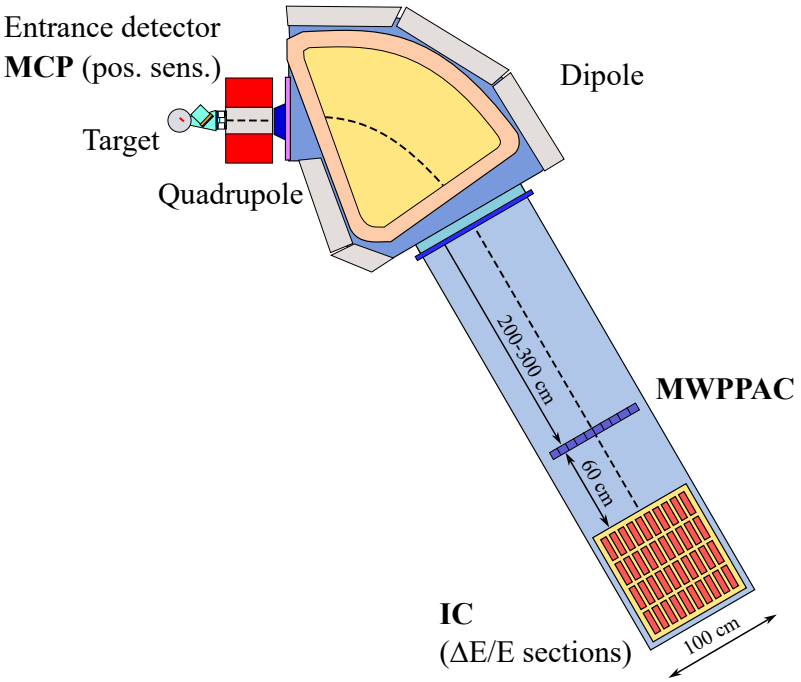

Figure 2.3: Schematic drawing of the PRISMA magnetic spectrometer, seen from above. The main elements are shown. Courtesy of Raquel :)

2.1.1 MCP

The MCP (Micro-Channel Plate) [7] detector is the first stage of PRISMA: it is mounted 250 mm from the target in the Chevron configuration, with two layers of plates having the micro-channels tilted one with respect to the other. A thin carbon foil, rotated by 45°, is placed on the path followed by the charged ions exiting the reaction chamber. When an ion passes across the foil, secondary electrons are emitted and drifted towards the position sensitive anode (biased at 2.45 kV), which is behind the micro-channel plates, through an electric field. A magnetic field directed from the carbon foil to the anode makes the electrons spiralize: in this way,

the position resolution is increased. Then, the micro-channel plates act as electron multipliers ($\sim 10^5$-10^6 factor), amplifying the signal. A sketch of the MCP detector is shown in Fig. 2.4. Two types of information are obtained from the MCP: the position where ions passed (X and Y) and a time signal, which is then delayed and used as STOP signal for the TOF.

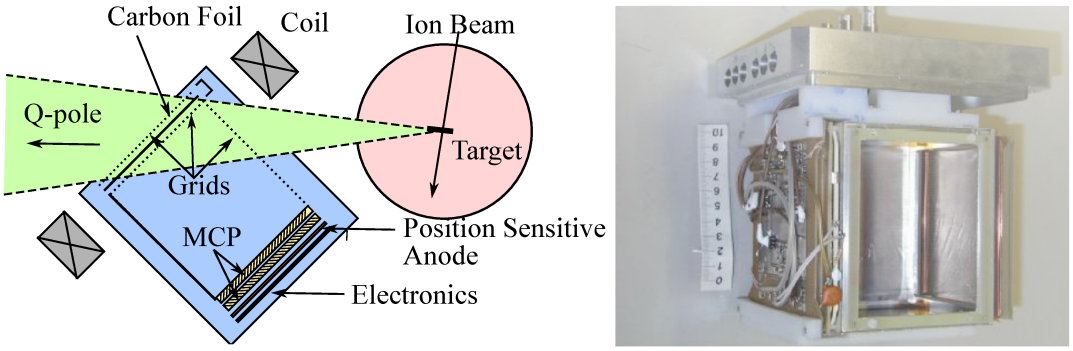

Figure 2.4: Left: sketch of the MCP detector, seen from above (courtesy of Raquel); right: a picture of the detector (taken from [7]).

The resolution in position of the MCP is approximately 1 mm both in the X and the Y directions, while the intrinsic time resolution is around 300-400 ps. Typical efficiencies for heavy-ion detection are around 90%.

2.1.2 Optical elements

In order to separate the ions for the mass identification, a couple of optical elements are placed right after the MCP. In particular, a quadrupole singlet is placed at 500 mm from the target: it acts as a focusing lens in the vertical direction, to reduce the spread of ions in the y axis, and as a defocusing lens in the horizontal axis, spreading the particles along this direction, thus increasing the angular acceptance of the whole apparatus in the polar angle. The entrance window of the magnet has a 320 mm diameter and the length of the element is 420 mm.

A large dipole magnet, placed 600 mm downstream of the quadrupole exit window, bends the trajectories of the ions according to their magnetic rigidity $B\rho$. This allows the separation of the ions on the so-called focal plane.

Typically, the magnitude of the magnetic fields is around 1 T. For the experiment, the fields were set to $B_{dip} = 0.699570$ T and $B_{quad} = 0.637796$ T in order to optimize

the detection of the ions of interest.

2.1.3 MWPPAC

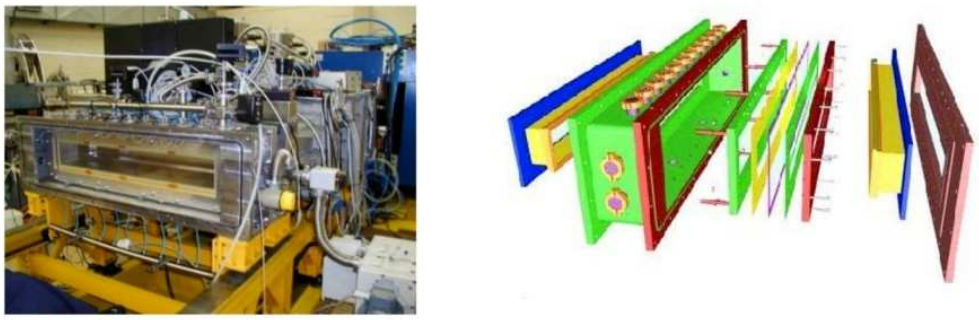

Figure 2.5: Picture (left) and design (right) of the MWPPAC of PRISMA. Taken from [8].

A large area Multi-Wire Parallel Plate Avalanche Counter (MWPPAC) [8] is placed 3.28 m after the dipole exit window, at the focal plane of PRISMA. A picture and a sketch of the detector are shown in Fig. 2.5. It is suited for the position measurement of the passing ions, in order to reconstruct the trajectory, and its cathode gives the START signal for the TOF. It consists in a volume of isobutane gas (C_4H_{10}) at 6 mbar (chamber dimensions: 1000 x 130 x 8 mm^3). The gas is separated from vacuum by two 1.5 μm thick mylar windows, supported by 100 μm thick vertical stainless steel wires, with a 3.5 mm spacing.

The inner structure is the following: a plane of gold plated tungsten wires, 20 μm thick, makes up the cathode, with a 0.33 mm pitch, while the anode is split into two parts, the X and the Y anodes, where the wires have a 1 mm spacing and a voltage of about 500 V. The cathode and the X anode, both made up by vertical wires, are divided into 10 separated sections, each one with an active area of 100 x 130 mm^2. This anode is placed 1 mm behind the cathode. The Y anode, made up by 130 horizontal wires 1000 mm long, is common for all the 10 sections. Since the Y position is not critical for the trajectory reconstruction, these wires are connected in pairs, so that the signal attenuation is decreased.

The working principle is the following: electrons are generated via ionization of the gas molecules when an ion passes and releases its energy; then, these electrons

are drifted towards the anode wires (as well as the ionized gas molecules towards the cathode) thanks to the electric field. If the field is strong enough, they can gain enough energy to ionize other molecules and create an avalanche, the *Townsend Avalanche*. This occurs near the anode wires, where the field is more intense. In this process, the signal induced in the read-out electronics is largely amplified, thanks to the large amount of collected charge.

The MWPPAC is a position-sensitive system, that exploits delay lines to reconstruct the X and Y impact coordinates. On the other hand, the cathode wires are short-circuited, in order to have a single fast position-independent signal for the TOF.

From the resolution point of view, the detector has a $\sim$ 1 mm resolution on the X axis and a $\sim$ 2 mm resolution on the Y direction. The intrinsic time resolution is around 300-400 ps, similar to the MCP, and therefore the TOF resolution comes out to be around 500 ps. Finally, the intrinsic MWPPAC efficiency is close to 100%.

2.1.4 Ionization chamber

Last stage of the PRISMA focal plane consists of an Ionization Chamber (IC) [8], 60 cm downstream of the MWPPAC detector. It is a segmented transverse-field chamber that measures the partial energy loss and the total energy of the incoming ions, thus allowing the nuclear charge identification (the Z number) through the ΔE-E technique. The sensitive volume is 1100 x 200 x 1200 mm^3 and is typically filled with high-purity methane (CH_4) or carbon tetrafluoride (CF_4), at pressures in the 15 - 100 mbar range. During the experiment presented in this thesis, CF_4 was used at a pressure of 33 mbar. These gases are chosen for their stopping powers, that depend also on the pressure, and for their particularly high electron and ion drift velocities, which allow it to stand relatively high rates ($\sim$5 kHz). The gas is separated from the vacuum by a 1.5 μm thick mylar window, placed at the entrance of the chamber and supported by 1000 stainless steel vertical wires. These wires are 1 mm apart and have diameter of 100 μm.

The charge collection is done by the electrodes, divided into 40 pads (4 rows, A, B, C, D, going downstream, and 10 columns, following the same subdivision of the MWPPAC; see Fig. 2.6). Each pad measures 10 cm x 30 cm. The chamber is closed by a set of 8 pads, 4 for each side, which work both as field-shape electrodes and as

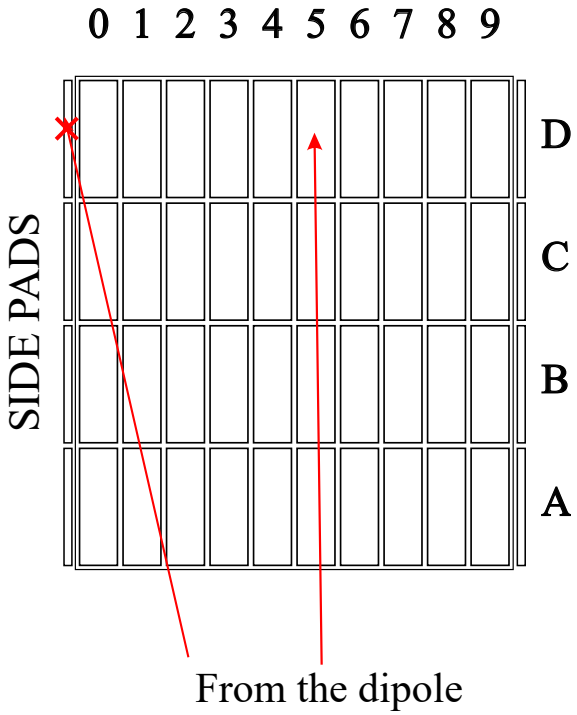

Figure 2.6: Scheme of the ionization chamber with the subdivision in sections (0-9) and rows (A-D). On the left and right parts, the side pads that act as veto detector. The red arrows represent possible trajectories that a particle can follow entering the chamber (the red cross represents the rejection by the veto pad).

veto detectors in the data processing. The working voltage is around 660 V for the anode and 330 V for the Frisch grid placed before the pads.

As already mentioned, the IC works as ΔE-E telescope: the reaction products entering the chamber gradually lose their energy until they stop in the gas. The energy loss information contains the Z dependence, according to the Bethe equation [36]:

$$-\frac{\mathrm{d}E}{\mathrm{d}x} \approx \left(\frac{1}{4\pi\varepsilon_0}\right)^2 \frac{4\pi e^2}{m_e} \frac{(Ze)^2}{c^2\beta^2} n Z_{medium} \ln\left(\frac{2m_e c^2\beta^2}{W}\right) \propto \frac{AZ^2}{E} \,, \tag{2.1}$$

where the stopping power (energy loss per unit length) is expressed as a function of several parameters, both from the medium the particle passes across and the particle of interest itself. Let us underline that the equation is written in its non-relativistic version, since PRISMA works typically with particle at low velocities ($\beta \lesssim 0.1$). In particular, as written in Eq. (2.1), this quantity is proportional to A and Z^2 of the reaction product and it is also related to the energy itself of the

particle. Therefore, plotting ΔE as a function of E, the Z separation becomes visible.

2.2 AGATA

AGATA (Advanced GAmma Tracking Array) is a γ-ray detector made up by electrically segmented High-Purity Germanium (HPGe) crystals. An algorithm exploits the segmentation to reconstruct the events inside the crystals, achieving a high resolution in combination with the Doppler correction algorithm. In particular, the tracking algorithm is based on the Pulse Shape Analysis (PSA), through which a grid search comparison between experimental and simulated signals from the segments gives the most probable reconstructed path followed by the γ-ray inside the detector. Thank to this tracking algorithm, AGATA can achieve values of FWHM (Full Width at Half Maximum) of few keV also for in-beam detection, where the Doppler effect is dominant, providing an excellent energy resolution. This array represents the state of the art in the γ-ray spectroscopy field with its American counterpart GRETA [37].

This projects is supported by an European collaboration and AGATA has been moving between several facilities in the past years (INFN Legnaro National Laboratories, Italy, 2009-2011 [38]; GSI, Germany, 2012-2014 [39]; GANIL, France, 2015-2021 [40]), also increasing the number of crystals. In 2022, the apparatus was installed again at LNL and coupled with the PRISMA spectrometer. In particular, 12 ATCs were mounted, for a total number of 36 crystals, facing the target at backward angles, on the opposite side with respect to PRISMA.

In Fig. 2.7 some pictures of AGATA in its current configuration at LNL are shown, i.e. coupled to the PRISMA spectrometer and to several lanthanum bromide ($LaBr_3$) scintillators.

2.2.1 AGATA TRIPLE CLUSTER

AGATA has a modular structure - the basic unit is the AGATA Triple Cluster (ATC) [41], composed by three asymmetric hexagonal shaped n-type HPGe crystals, with their pre-amplifiers, held by the supporting structure and cooled down by a cryostat. A CAD design of an ATC is shown in Fig. 2.8, with a sketch of the single crystal.

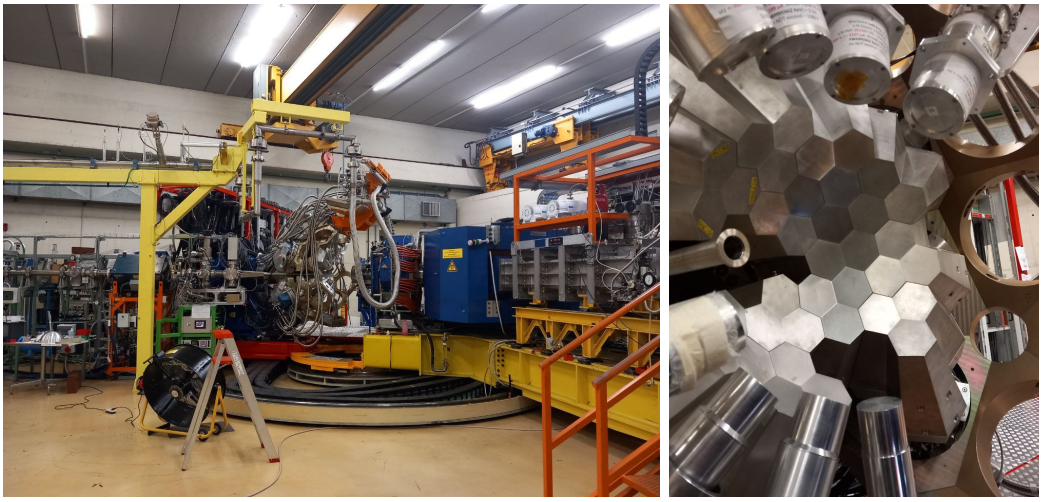

Figure 2.7: Pictures of the AGATA array coupled to the PRISMA spectrometer (left) and to the set of $LaBr_3$ scintillators at LNL (right).

In the 4π configuration, AGATA would count 60 ATCs, with a nominal coverage of 82%.

Each crystal is 36-fold segmented, six-fold in the azimuthal direction and six-fold in the longitudinal one: such segmentation provides 36 independent electrical signals for each crystal. In addition, the central contact (core) gives two signals, for a total of 38. The signal is produced by the collection of charges (electron-hole pair) generated via ionization by the incoming γ-ray. The electrons are collected by the core and they give the total energy deposited in the crystal, while the holes are collected by the single segments for the position measurement.

As already mentioned, the main feature of AGATA is the excellent Doppler-shift correction. This is achieved through the combination of segmentation and PSA, which provides the position of the interaction point, and then the tracking algorithm takes the information on the energy deposition on these hit points and finds the most probable path the photon could have followed inside the crystals. The accuracy on the hit site is around 5 mm of FWHM. The trajectory reconstruction is done by the algorithm exploiting the Klein-Nishina formula [42] for the differential cross section of Compton scattering on the electrons in the crystal. In this way, the entrance angle of the γ ray in the detector can be determined and used for the Doppler-shift correction, once the velocity of the emitting ion has been measured, for example, by the PRISMA spectrometer.

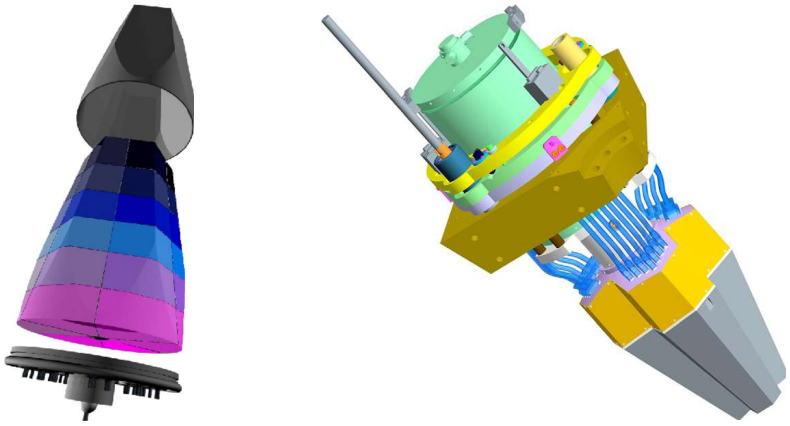

Figure 2.8: Design of the ATC, the AGATA modular unit. On the left, the electrically segmented Ge crystal. Each segment provides an independent electrical signal. On the right, the triple cluster with the liquid nitrogen Dewar and the pre-amplifiers. Taken from [9].

2.2.2 Neutron damage

During experiments, large flux of neutrons, produced in the reactions, can impinge on the AGATA crystals, eventually producing the so-called neutron damage, i.e. the dislocation of germanium atoms inside the crystal lattice. The energy measurement and the Doppler correction are worsened by these defects, which act as hole traps and lead to a reduction in the charge collection. Nevertheless, the effect can be corrected using the position information, since the fraction of charge lost due to the trapping depends mainly on the carriers type and on the path they follow from the generation point to the collection electrode [43].

2.3 LaBr scintillators and silicon detector

A set of 9 $LaBr_3$(Ce) scintillating detectors was placed around the scattering chamber, facing the target, in the 90° position with respect to the beam line. They were of two different diameters, 2 and 3 inches; the smaller detectors were supplied by a 570 V voltage, while for the larger ones it was between 700 V and 980 V. In Fig. 2.9 the design of the AGATA + $LaBr_3$ coupling is shown.

Finally, in the scattering chamber, a pin silicon detector was placed as a monitor for the beam and target conditions: during the beam-time, it could directly

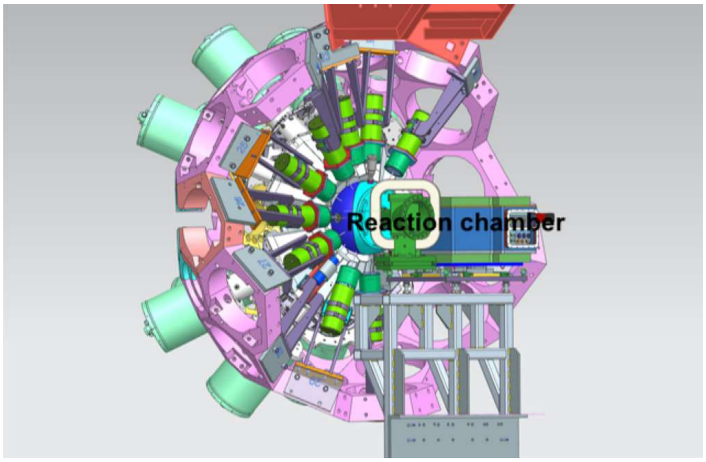

Figure 2.9: Design of the AGATA + $LaBr_3$ coupling. Taken from [6].

detect the charged particles produced in the collision, in particular the Rutherford-scattered carbon and nickel ions. Being a silicon detector, it was sensitive to the energy deposition of ions passing through. The type of signal was therefore an energy signal in channels, higher for the heavier atom (nickel), lower for the lighter one (carbon).

For the thesis purposes, a detailed analysis is not necessary. The only relevant information is that the target conditions were stable during the entire experiment.

3

Data pre-sorting and analysis

In this Chapter, the data pre-sorting and the calibration routines for the detectors are presented. The analysis of PRISMA data and of a part of the AGATA data is reported. From this preparatory work, the main results will be shown in Chapter 4.

3.1 Calibration and pre-sorting

In order to prepare the apparatus in the best conditions for acquiring data, thresholds, electronics gates and calibrations must be applied. A large fraction of this thesis work was devoted to get a proper off-line calibration of the various sub-detectors. As side note, I would like to mention that I also participated to the on-line calibration and preliminary analysis, done while the experiment was still on-going in order to obtain some preliminary results.

3.1.1 MCP

The MCP detector was calibrated exploiting some reference points given by the metallic stripes in front of the sensitive layer. In particular, the procedure consists in applying a set of rotation and deformation matrices that fit the reference points, in addition with a reflection on the y axis (see Appendix B for details). In Fig. 3.1 the MCP data are shown with the reference points in red and the calibrated points

in green. In addition to the metallic stripes, two shadows are visible in the figure: they come from two screws inside the chamber where the MCP is placed.

This calibration is important for the position measurement and therefore for the trajectory and velocity reconstruction for each ion.

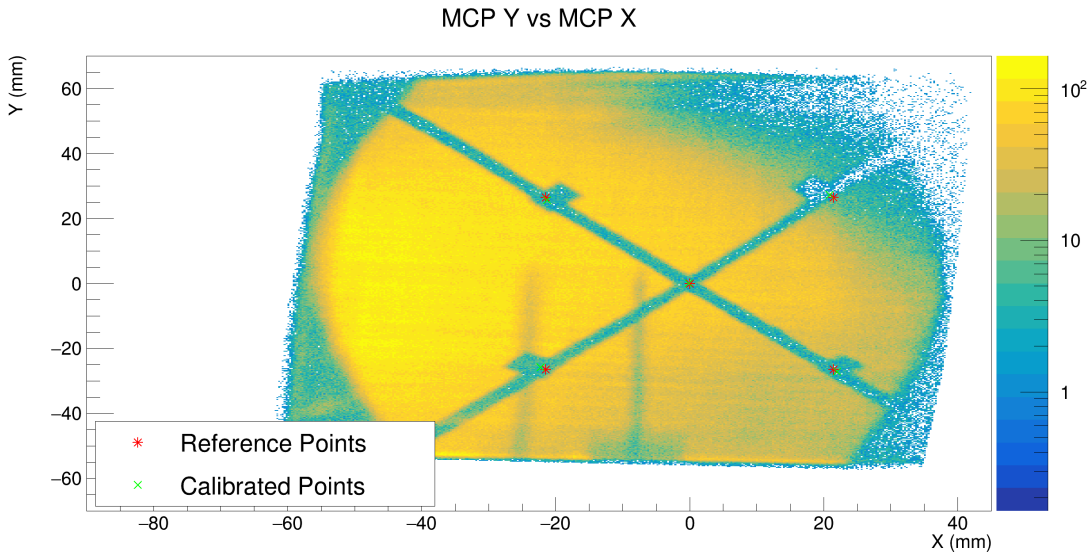

Figure 3.1: Calibrated MCP X-Y matrix with reference (red) and calibrated (green) points.

3.1.2 MWPPAC

For the MWPPAC, several checks must be done. Most of them consist in threshold evaluations, meaning that the signal has to be within two given values, or in gate application, meaning that the data have to lay inside a ROOT graphical cut. This procedure is done in order to avoid noise and pile-up data. See the Appendix B for more details.

The final goal of the MWPPAC calibration is to obtain the event distribution in the focal plane of PRISMA: the X_{FP} coordinate of the acquired data must lay in the proper range for each MWPPAC section, therefore the position (in channels) must be calibrated and converted in millimeters. The calibration procedure is done section by section; the final result is the focal plane position spectrum shown in Fig. 3.2. The spikes visible in the middle of each subdivision work as reference for the calibration.

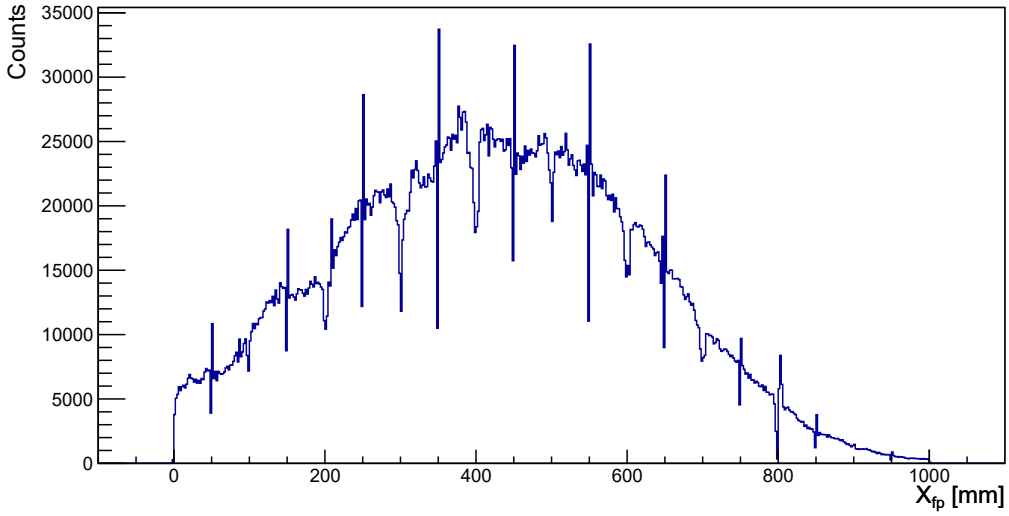

Figure 3.2: Events distribution in the focal plane, x-coordinate; the spikes are the references in the center of each section.

3.1.3 IC

The calibration of the ionization chamber consists in a gain-matching procedure. A charge injector, i.e. a simple circuit that integrates a certain amount of charge and injects it in the electrodes of the IC, is used to mimic the signal of particles passing through the chamber. Changing the amplitude of the injector pulse, the position of the associated IC peak changes. Then, a linear calibration is performed to extract the parameters for each pad. The quality of the gain matching between the different IC sections contributes to the final nuclear (Z) and atomic (q) charge resolution.

After the gain matching, some thresholds have to be set in order to reject events in the ADC pedestal and in overflow. An example of raw data from a pad is reported in Fig. 3.3 (row A, pad 0; see Fig. 2.6 for reference), with the set thresholds in red. The histogram essentially reflects the energy lost by the ions in the gas volume underneath the pad and two peaks can be seen. The one at lower energy is associated to target-like ions, the other one to beam-like ions. The thresholds are set in order to discard the noise events, especially at low energy. All the pad spectra are shown in the Appendix B.

During the procedure, an anomalous peak was seen in the C1 pad. A more

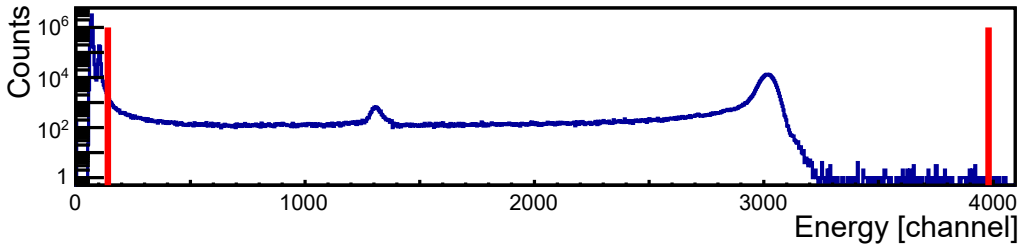

Figure 3.3: IC signals for row A, pad 0, with related thresholds.

in-depth analysis is reported in the Appendix B.

3.1.4 TOF

For the TOF, a set of thresholds must be set in order to discard the ADC pedestal and possible noise at high values of TOF in the raw signal. Then, a procedure of alignment of the TOF variable versus the position in the focal plane is performed in order to set the correct velocity β of the ions. This is done aligning the TOF spectra from all the MWPPAC sections and estimating the average time of flight of the quasi-elastic channel from kinematic considerations. This final part provides a general offset for the TOF variable. In Fig. 3.4, the TOF-X_{fp} plot is shown: the structure at higher time of flight comes from the beam-like ions, while the data on the bottom are the target-like fragments. These structures are well aligned as result of the aforementioned process.

In the case of the present experiment, the ^{60}Ni elastic channel is the dominant one and was taken as reference for setting the time-of-flight offset. In particular, simulation programs like *LISE++* [44] and *reaction* were used to determine the average velocity of the Rutherford-scattered ^{60}Ni ions; the precise value for the TOF offset was then obtained considering an effective flight base of 6 m, distance from the MCP to the MWPPAC. The reference TOF was put at 178 ns.

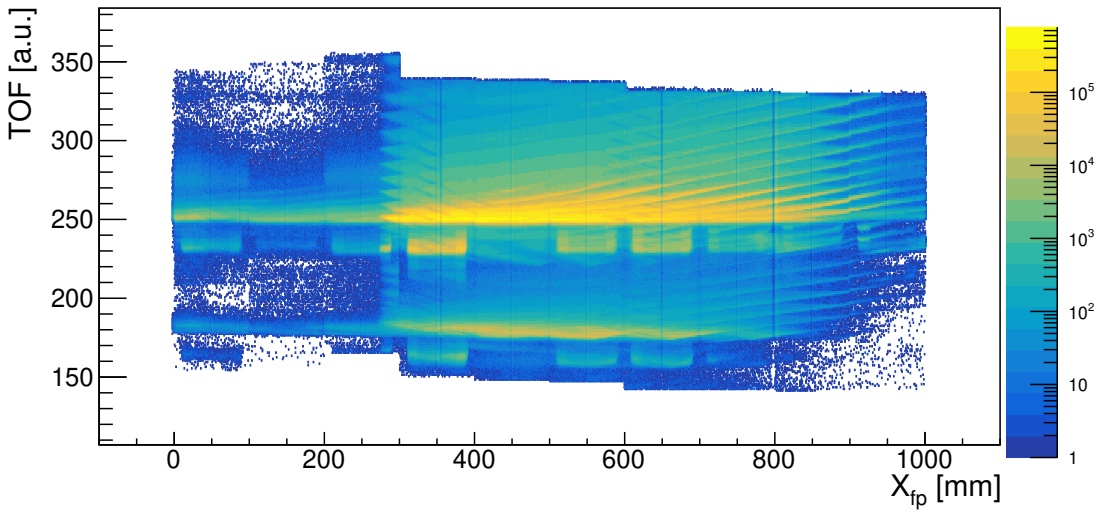

Figure 3.4: TOF versus X_{fp}. The data are divided into two regions: the upper one coming from the beam-like ions, the lower one from the target-like ions.

3.2 Analysis of PRISMA data

3.2.1 ΔE - E matrix and Z identification

The first step of the analysis on PRISMA data is the nuclear charge (Z) identification. As already mentioned in Par. 2.1.4 referring to Eq. (2.1), the different atomic numbers of the reaction products detected in PRISMA can be distinguished by looking at the ΔE-E matrix. Here, ions with different Z are placed in different regions, as shown in Fig. 3.5. In this case, the most intense channel corresponds to the target-like fragments, i.e. the nickel ($Z = 28$), also at the scattering angles covered by PRISMA (θ_{lab} ~15°-25°). By assigning the right Z to the nickel, the other nuclear charges follow, increasing with increasing energy loss. One can notice the near-diagonal structure, especially at higher energy and energy loss: it comes from the beam-like nuclei entering PRISMA. Additionally, some "shadows" can be seen, probably coming from pile-up or other electronic effects. Indeed the rate of ions at the focal plane in the present experiment was about 5-10 kHz due to the Rutherford scattered Sn ions entering PRISMA. Normally the spectrometer is operated with trigger rates of 1-2 kHz.

During the analysis, a broadening of some Z-structures was observed, especially

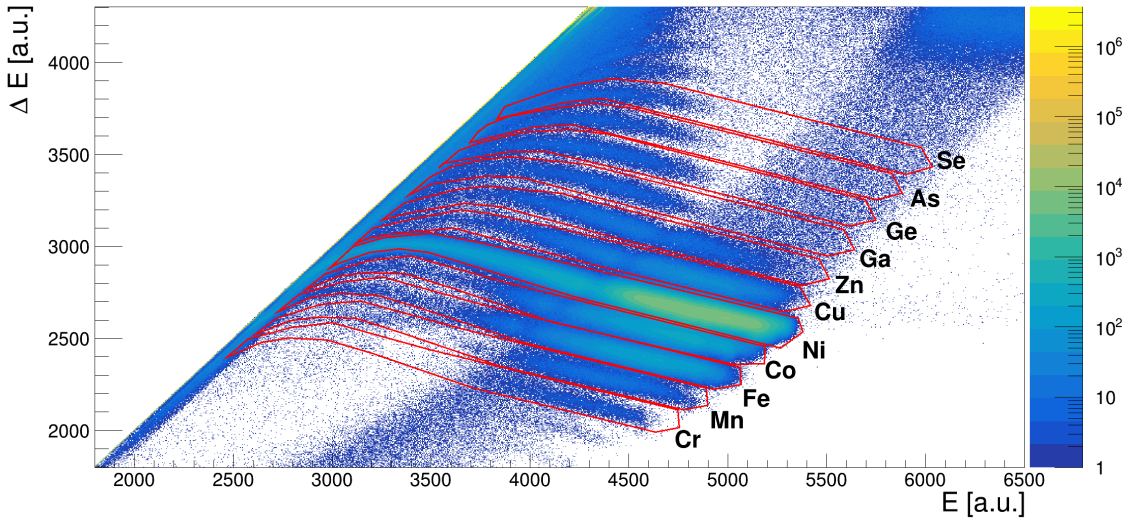

Figure 3.5: ΔE-E matrix with identified nuclear charges.

in the nickel region, probably due to a non perfect gain matching of the IC pads. In order to avoid this effect and correct the matrix, a section-by-section re-calibration was performed. Taking the central sections as reference, IC data were aligned Z by Z putting an offset in both E and ΔE variables.

Once the atomic numbers are properly set, the atomic charge states (q) must be identified.

3.2.2 Charge state identification

In order to separate the produced ions with different charge states, the E-$R\beta$ plot is built. E represents the total energy released by the ion in the IC, while $R\beta$ is the product of the curvature radius inside the bending dipole of PRISMA, obtained from the trajectory reconstruction algorithm, and the ion velocity, extracted by the TOF measurement. The two quantities are related in this way: knowing that the magnetic rigidity BR is

$$BR = \frac{p}{q} \tag{3.1}$$

and $E = \frac{1}{2}mv^2 = \frac{1}{2}p\beta c$ (typically the velocities are not relativistic in this kind of experiments, so the $\gamma \sim 1$ approximation holds), with simple manipulations one

can find

$$R\beta = \frac{p\beta}{qB} = \frac{2E}{cqB} \,, \tag{3.2}$$

from which

$$E = \frac{qBc}{2} R\beta \,. \tag{3.3}$$

Now, in the E-$R\beta$ matrix (example in Fig. 3.6) some structures are clearly visible and the different lines are therefore associated to different charge states. The re-calibration procedure presented in Par. 3.2.1 affects also this part of the analysis, providing in principle a better alignment of the charge-state structures. In practice, the situation is more complicated and in order to get a perfect alignment of the IC sections additional work should be done. Indeed, contaminations coming from neighbouring charge states and also from neighbouring nuclear charges (especially near the most intense reaction channel) will be still present in the following steps, worsening the mass resolution. Despite this fact, for this thesis purpose this perfect alignment is not essential.

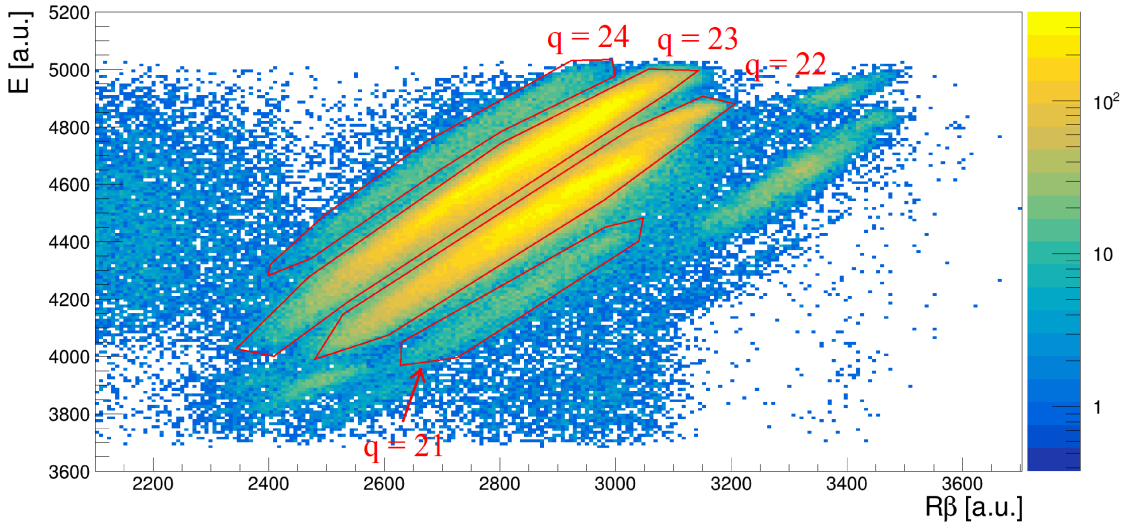

Figure 3.6: Example of E-$R\beta$ matrix with identified atomic charge states for $Z = 26$ (Fe). The other structures visible in the figure are coming from contaminants, like other elements accidentally included in the Z gates, or from the non-perfect alignment of the IC sections.

For the charge state assignation, the results from the simulation program *reaction* were used as first guess. Indeed the program gives the probability distribution of the

different charge states for a given reaction, but the actual distribution can slightly change due to the selectivity of the PRISMA spectrometer, set through its dipole and quadrupole magnetic fields.

3.2.3 A/Q ALIGNMENT

Once the charge state is assigned and the q-gates are done, the A/q spectra are analyzed. These are basically rough mass spectra sorted by atomic number and atomic charge, not yet merged together. In particular, they are extracted from the reconstructed trajectory and from the TOF using once again Eq. (3.1); now, since $p = mv = Auv$ where u is the nucleon mass, one can write:

$$\frac{A}{q} = \frac{BR}{uv} = \frac{BR}{uL} TOF \ , \tag{3.4}$$

where the velocity is calculated from the flight base and the time of flight as

$$v = \frac{L}{TOF} \ . \tag{3.5}$$

From here the importance of the time alignment in Par. 3.1.4 is evident.

At this point, it is important to calibrate them in such a way that they are coherent at given Z, varying the q, and also that the resulting mass spectrum is realistic: for instance, the highest A/q peak for $Z = 28$ should correspond to mass $A = 60$, being the elastic channel. More in general, the below-barrier transfer reaction favours the minimal exchange of particles from one nucleus to the other one (Sec. 1.3, Eq. (1.19)). For a better mass assignment, γ rays are needed.

Moreover, some optical aberrations can appear at this level. In fact, the magnetic field is not perfectly limited inside the quadrupole and dipole volumes, therefore the boundary effects of the magnetic fields must be taken into account. In order to optimize the alignment, some parameters can be adjusted, like the effective dipole length and the effective target-to-quadrupole length. These parameters can slightly change the shape of the final A/q peaks, affecting the final mass resolution. Then, if the aberration is still marked, a "by-hand" correction can be applied, forcing data to stay on a straight line. More details on the aberration correction will be given in Appendix B.

3.2.4 A/q calibration and mass assignment

The A/q calibration is an iterative process, since it is not always possible to know the correct mass from the beginning; therefore, a first guess is done in the mass assignment, which will be confirmed or corrected by looking at the γ-ray spectra. For the nickel channel, the procedure is easier, since the dominant channel is the elastic one. Therefore the mass assignment is straightforward for this species.

By assigning a mass to each peak in the A/q spectrum, an expected value for the A/q itself is obtained for each peak and each charge. Therefore, a linear calibration can be done, taking the experimental A/q values and fitting them with respect to the expected ones in order to get the calibration parameters.

Moreover, after this calibration, also the charge state can be corrected to improve the accuracy of the final mass spectrum. In particular, the total calibration procedure can be expressed as

$$M = [a \cdot (A/q)_{exp} + b] \cdot q_{eff} \ . \tag{3.6}$$

In Fig. 3.7, the calibrated mass spectrum for the nickel isotopes, main focus for this thesis, is shown as an example; the mass distributions for the other elements are reported in the next Chapter. The $+1n$ and $+2n$ channels can be clearly seen on the right of the dominant peak, corresponding to the quasi-elastic channel (^{60}Ni). Small contributions from the neutron pick up of tin on nickel ($-1n$, $-2n$) are visible at lower values of mass.

3.3 Analysis of AGATA data

The calibration of AGATA was performed using radioactive sources, like ^{60}Co, AmBe and ^{226}Ra. These sources present well known transitions and span over a wide range of energies, as shown in Tab. 3.1. Noteworthy is that the AmBe source, usually employed as neutron emitter, was selected for its particularly high energy γ ray: the α particle emitted in the ^{241}Am decay interacts with the ^{9}Be through an (α,n) reaction, populating the 2^+ state of ^{12}C at 4438 keV.

After the calibration, and once the analysis of PRISMA data is concluded, the γ-ray analysis can be performed including the information extracted from the spec-

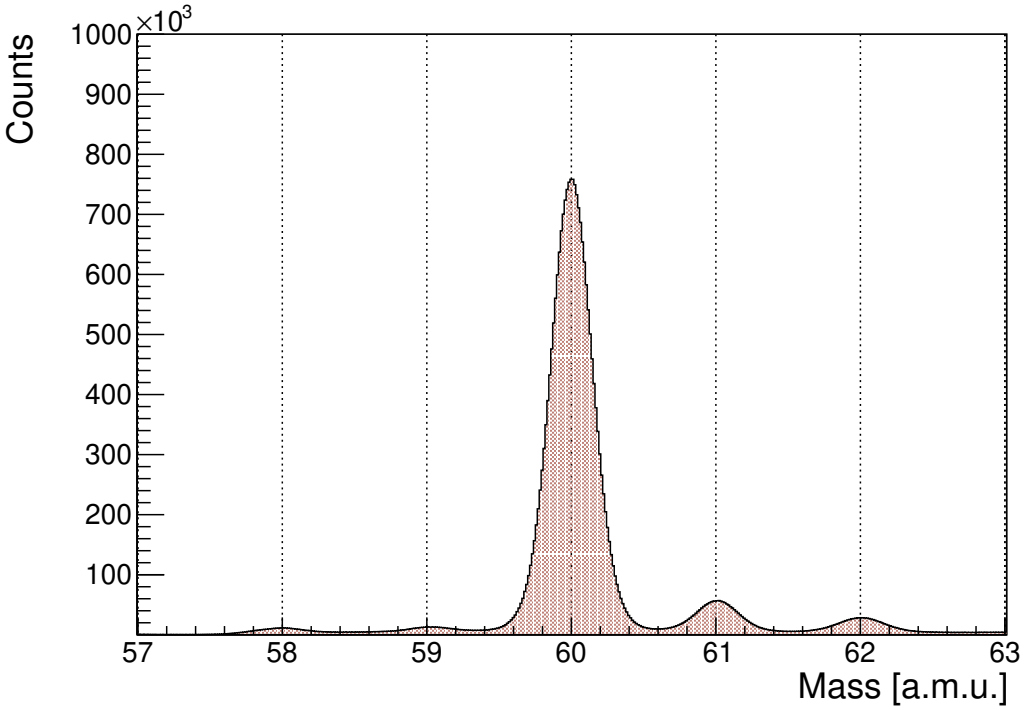

Figure 3.7: Mass distribution for $Z = 28$ (nickel).

Source	Energy [keV]
^{60}Co	1173, 1333
^{241}Am^{9}Be	4438
^{226}Ra	295, 352, 609, 1120, 1765, 2204

Table 3.1: γ-ray calibration sources and their associated energies.

trometer, in particular the velocity β of the ions and their scattering angle. Indeed, these quantities are the essential ingredients for the Doppler correction of the peaks, done on an event-by-event basis.

The resulting γ-ray spectra should be already calibrated and Doppler corrected by the analysis program, but some parameters can be still optimized to align the peaks at best. For example, in Fig. 3.8 the Doppler-corrected energy of the γ rays detected in coincidence with the ^{60}Ni (identified with PRISMA) is plotted as a function of the variation of the time of flight ΔTOF. The yellow line is associated to

the peak from the first 2^+ state of ^{60}Ni. The energy correction depends on β, which is obtained through the TOF measurement: a change in the global offset produces a shift in velocity and therefore in the energy correction. Since the energy of the 2^+ excited state is well known (1332.5 keV), it can be taken as reference: in this way, the proper TOF offset can be chosen as the correction needed to reproduce the energy of the transition, i.e. the abscissa coordinate of the intersection between the peak line and the reference red line in Fig. 3.8. There are some simple explanations for such corrections: the uncertainty on the energy loss in the target, the target thickness, its angle with respect to the beam and other effects. For example, in this work the online configuration was used for the analysis, including calibration and settings (like neutron damage correction), but in principle one should improve and optimize the parameters in an off-line analysis. Another factor could be the beam energy uncertainty ($\sim 1.5\%$), which then reflects itself in the velocity of the particle and therefore in the TOF: a lower energy would correspond to a larger time of flight. In general, the combination of all these effects could produce this shift.

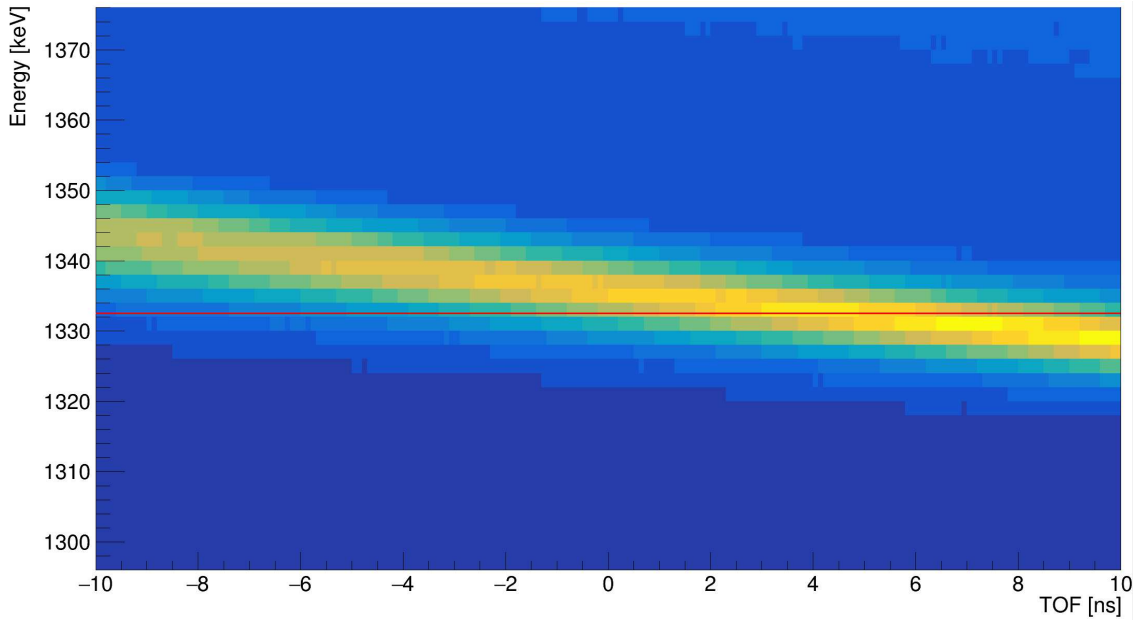

Figure 3.8: Example of detected γ-ray energy vs ΔTOF for the ^{60}Ni. The red line represents the energy of the first 2^+ state (1332.5 keV) used as reference.

In Fig. 3.9, the resulting γ-ray spectrum of ^{60}Ni is shown with (red) and without (blue) the Doppler correction. The capabilities of AGATA in terms of Doppler

correction can be clearly appreciated observing the highest peak, coming from the de-excitation of the already mentioned first 2^+ state of ^{60}Ni. In the non-corrected spectrum, the peak is broadened and shifted in energy, while, after the correction, a FWHM of about 10 keV is obtained.

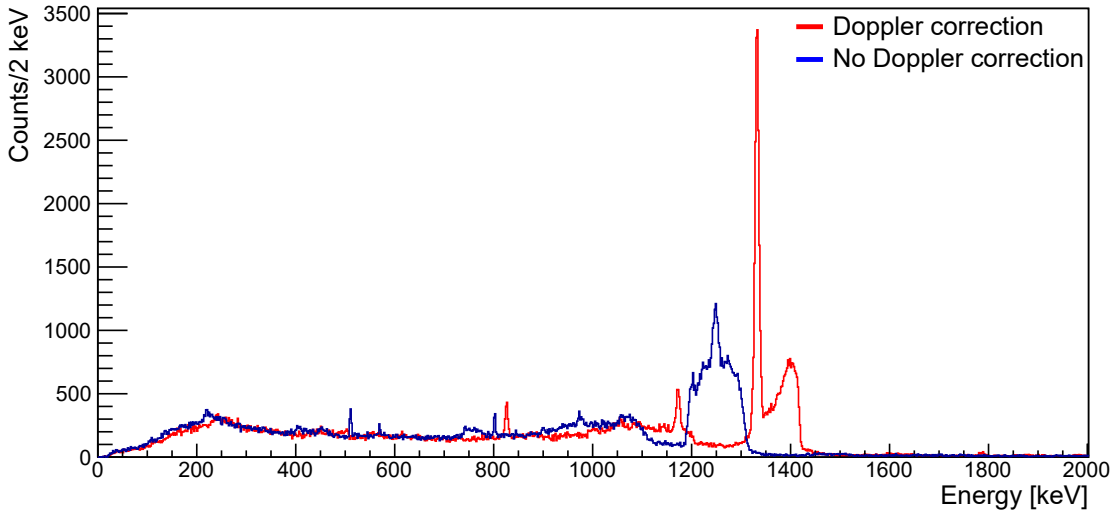

Figure 3.9: γ-ray spectrum for ^{60}Ni. In blue, the non-corrected spectrum; in red, the Doppler-corrected one.

4

Results

In this Chapter, the main results of the thesis work are presented. In particular, the mass distribution for the relevant isotopes produced in the reaction will be presented, followed by the extraction of the transfer probabilities and the discrete line identification performed with AGATA.

4.1 Mass distributions

The first result of the analysis presented in this work is the mass distribution for elements going from $Z = 24$ to $Z = 30$, produced via transfer reactions. In Fig. 4.1 all the mass spectra are presented in logarithmic scale. Some of them are cleaner than others, for example a contamination can be clearly seen between mass 60 and mass 61 for the Cu isotopes ($Z = 29$). This comes presumably from the nickel channel as the Z and q gates could include data from the neighbouring loci. Nonetheless, some physics considerations can be done directly from these distributions. For example, in the copper mass spectrum, the $+(1p2n)$ channel that populates ^{63}Cu is enhanced with respect to the $+(1p1n)$: this could be seen as a proton + paired-neutrons transfer, indicating again the presence of pairing correlations between neutrons. Then, regarding the iron isotopes, the $-(2p2n)$ process has an enhancement as well. In this case, one could also suggest the idea of α-cluster transfer, populating ^{56}Fe. Any-

way, a more in-depth analysis should be performed in order to obtain more stringent conclusions on the nature of these enhancement effects, including the contributions given by detector acceptance, kinematic relations and Q-value considerations.

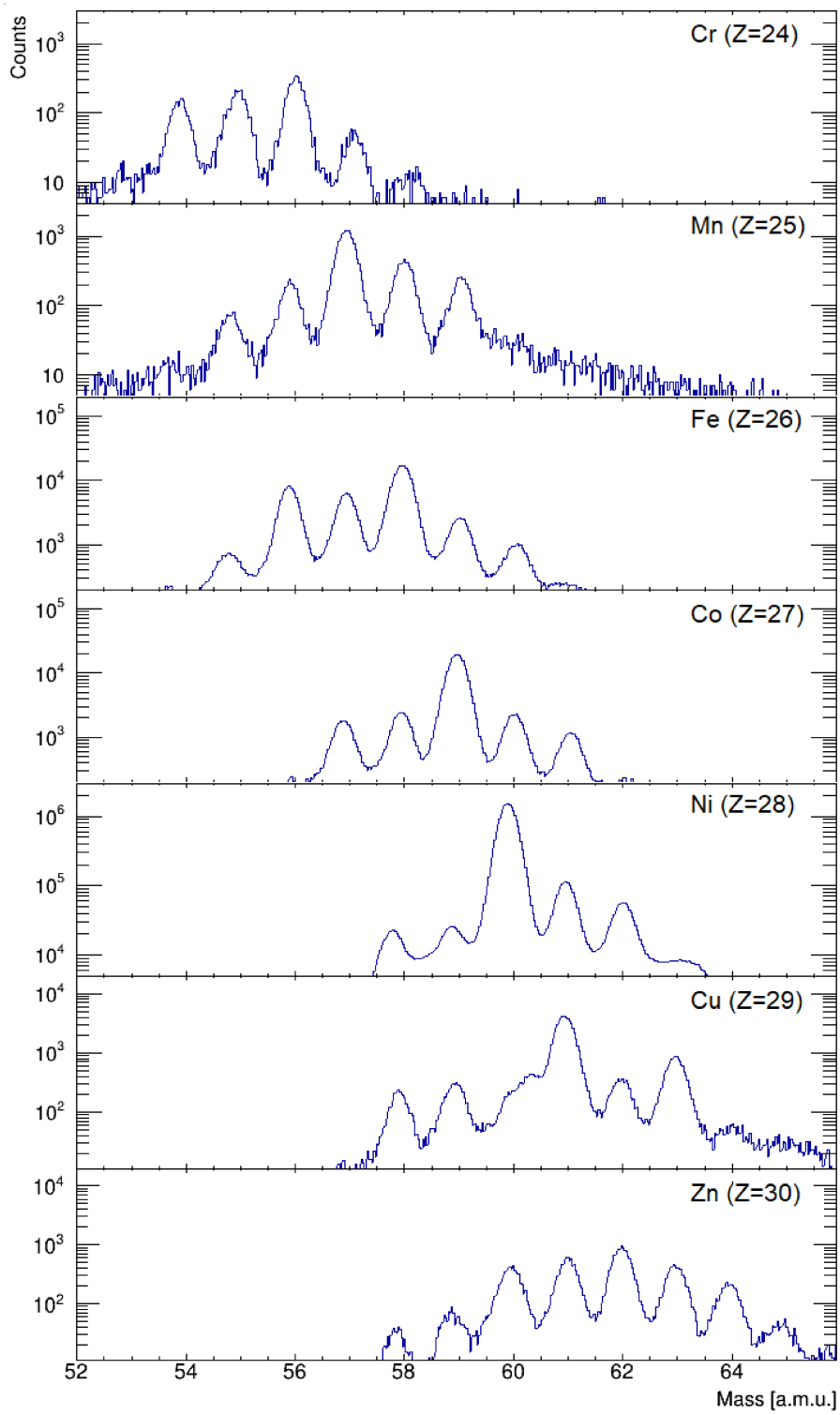

Figure 4.1: Mass distributions in logarithmic scale for Z from 24 (Cr) to 30 (Zn).

4.2 Transfer probabilities

From the analysis of PRISMA data, the transfer probabilities can be extracted integrating the peaks in the mass distributions. In particular, since we are interested in the $1n$- and $2n$-stripping channels, the data are gated on $Z = 28$ (nickel). As already mentioned a number of times, the elastic + inelastic ^{60}Ni channel is the dominant one; for a better view it is worth to plot the mass spectrum in logarithmic scale (Fig. 4.2).

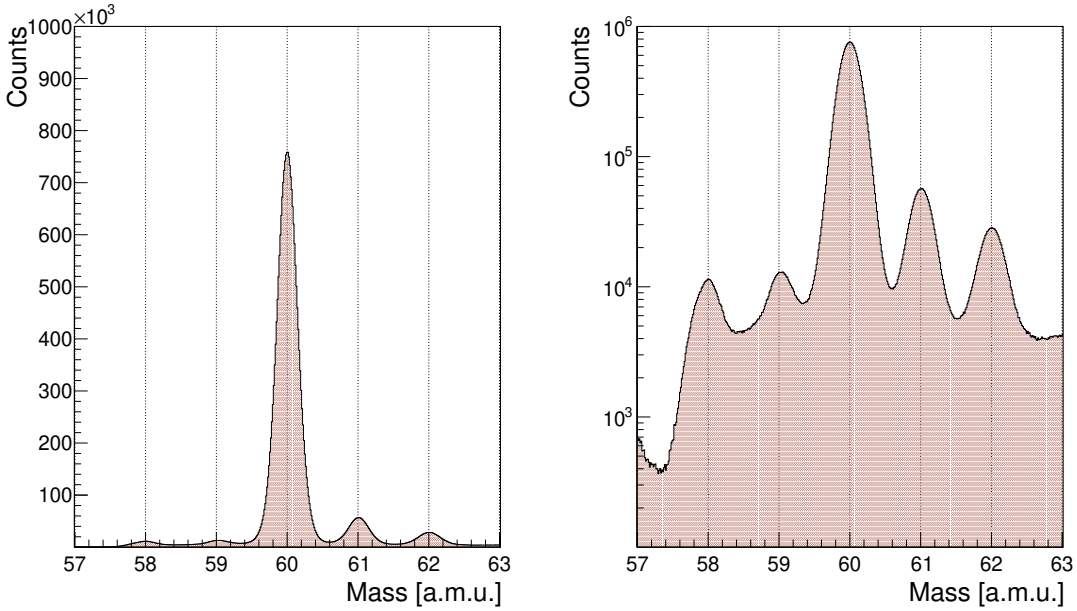

Figure 4.2: Mass distribution for $Z = 28$ (nickel) in linear scale (left) and logarithmic scale (right).

By using a multi-Gaussian fit with background subtraction, the area within each peak is obtained. Now, the differential cross-section for the transfer reaction follows the relation

$$\frac{\mathrm{d}\sigma}{\mathrm{d}\Omega} = P_{tr}\left(\frac{\mathrm{d}\sigma}{\mathrm{d}\Omega}\right)_{Ruth}, \tag{4.1}$$

as already mentioned in Section 1.3. Then, the differential cross-section is proportional to the reaction yield in a given solid angle and at a given energy. Therefore, the relation above holds also for the yield, i.e. for the amount of counts for each

mass number (Eq. (4.2)).

$$\int \frac{\mathrm{d}\sigma}{\mathrm{d}\Omega}\,\mathrm{d}\Omega \propto N_{events} \longrightarrow N_{tr} = P_{tr} N_{elastic}\ . \tag{4.2}$$

Consequently, as a preliminary result, one can calculate the relative transfer probabilities taking the ratio between the integrals for $A = 61$-62 and the integral of the $A = 60$ channel:

$$P_{xn} = \frac{I_{60+x}}{I_{60}}\ , \tag{4.3}$$

where x represents the number of transferred neutrons. Considering all the PRISMA angular acceptance, a single value is obtained for each process, associated to the angular position $\theta_{lab} = 20.48°$.

$$P_{1n} = (7.085 \pm 0.004) \cdot 10^{-2} \qquad P_{2n} = (3.499 \pm 0.003) \cdot 10^{-2}\ . \tag{4.4}$$

The interesting result is that $P_{2n}/P_{1n} \simeq 0.5$: in a simple independent $2n$ transfer (Sec. 1.3) we would have obtained

$$P_{2n} = P_{1n}^2 \simeq 5 \cdot 10^{-3}\ , \tag{4.5}$$

while here there is an enhancement of the transfer probability. This is in agreement with what already observed by Montanari et al. [31], suggesting the presence of a correlation between the neutrons. In order to better compare the results with the previous experiment, the transfer probability has to be plotted as a function of the distance of closest approach.

Being a two-body reaction, the kinematic quantities are well defined and fixed at given energy and angle. In particular, the scattering angles θ^* for Sn and Ni are evaluated in the center of mass (CM) reference frame taking the Sn trajectory as reference for the 0° direction (Fig. 4.3). Therefore, the angular variable entering Eq. (1.15) for the distance of closest approach is $\theta^*_{Sn} = 180 - \theta^*_{Ni}$, with θ^*_{Ni} calculated using Eq. (4.6),

$$\theta^* = \theta_{lab} + \arcsin(\eta \sin\theta_{lab})\ , \qquad \eta = \frac{v_{cm}}{v^*}\ , \tag{4.6}$$

where η is the ratio between the velocity *of* the center of mass and the velocity of the

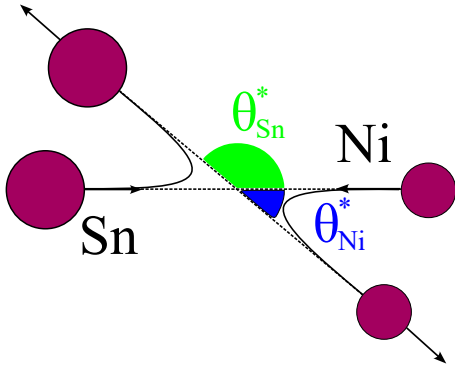

Figure 4.3: Schematic picture of the scattering process with the different angles.

particle *in* the center of mass reference frame. By using the average reconstructed velocity of the nickel ions, the angle in the CM frame is $\theta^*_{Ni} = 37.6°$ (in blue in Fig. 4.3), which corresponds to $\theta^*_{Sn} = 142.4°$ (in green in Fig. 4.3) and therefore to a distance of closest approach of 13.20 fm. In Fig. 4.4 the results of this work are shown together with the data from the reference experiment.

It is clearly visible that the full dots are slightly shifted with respect to the empty ones. This deviation can probably be related to the calculation of the distance of closest approach: in particular, one source of error is the beam energy, which is typically a bit lower than nominal. As already mentioned, a $\sim 1.5\%$ uncertainty on the beam energy must be considered. Therefore, changing the energy with $E \longrightarrow E - 1.5\%$, a new value for the distance of closest approach is obtained and the results are shown in Fig. 4.5. Moreover, the angle determination could be affected by the uncertainty on the position of the reaction site, which is just assumed to be in the middle of the target. The effect of this uncertainty cannot be easily estimated. For this thesis purposes, the simpler effective correction on the energy is sufficient.

Keeping this energy correction, a further analysis can be performed dividing the acceptance of PRISMA in angular sectors. In particular, the entrance position given by the MCP can be translated in terms of entrance angle. The total MCP angular coverage goes from 11.7° to 31.2°. With a $\Delta\theta_{MCP} = 1.95°$, the same aforementioned procedure can be followed, integrating the mass peaks for each angular sector.

In Tab. 4.1 the angular subdivision is reported with the calculated scattering angles in the center of mass frame for both beam-like and target-like ions. With

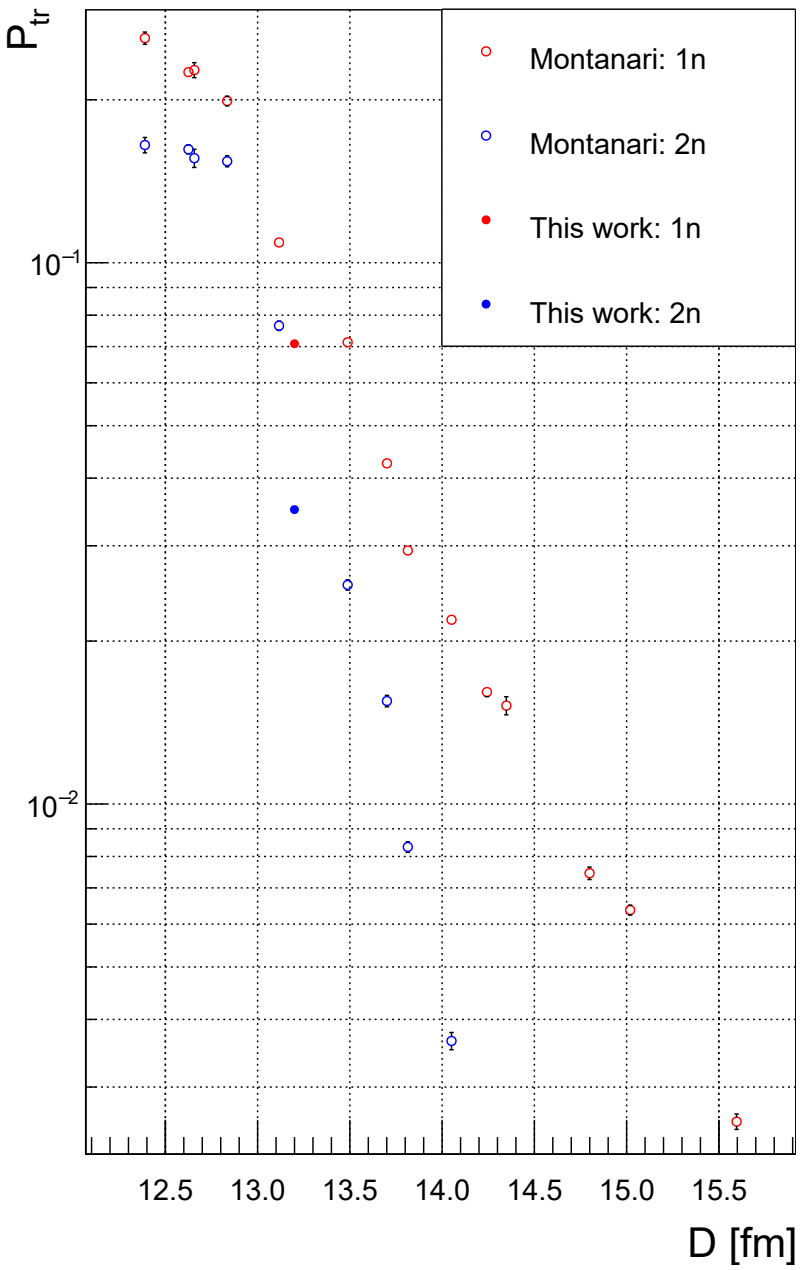

Figure 4.4: Transfer probability plotted as a function of the distance of closest approach for the $1n$- and the $2n$-transfer channels (respectively, red and blue full circles). The data from the previous experiment (empty circles) are shown for comparison.

θ_{center} we indicate the angle associated to the center of the angular sector, i.e. the mean between the two $\theta_{extremes}$. All the quantities are evaluated following the same

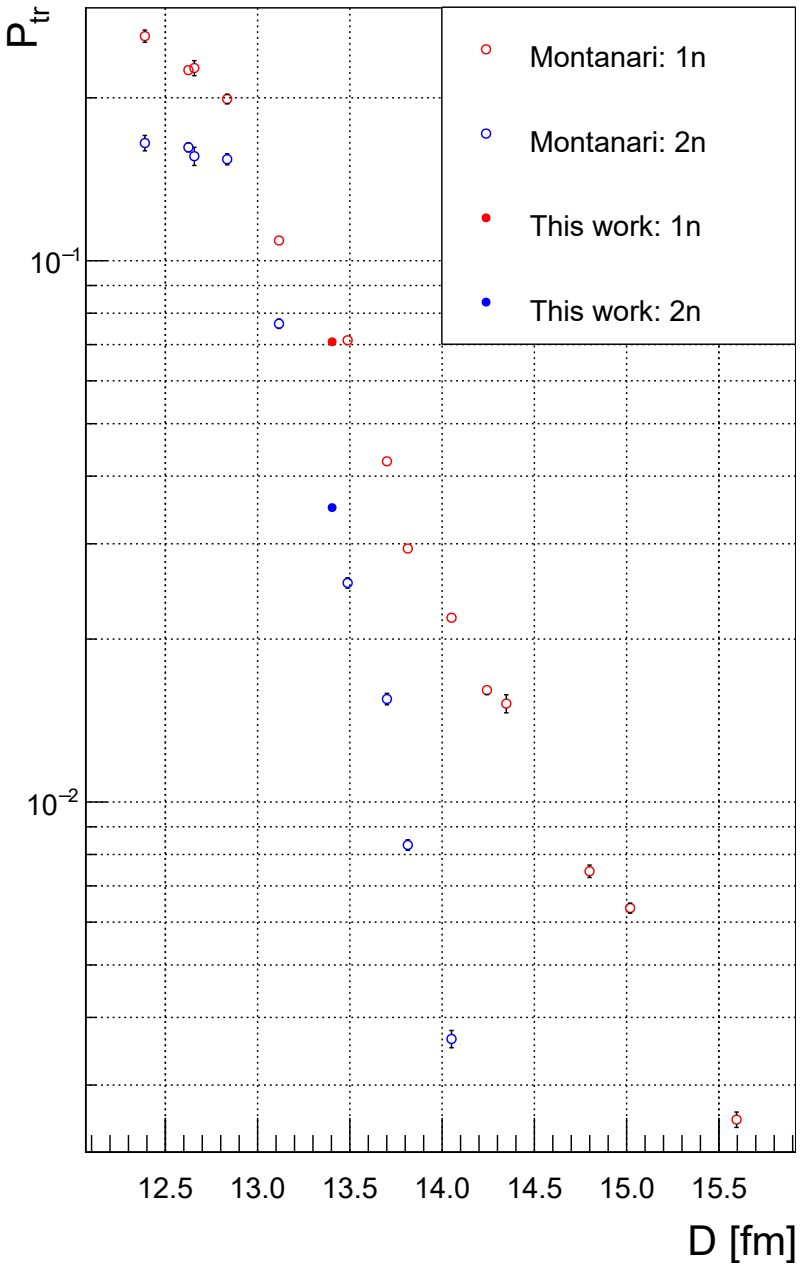

Figure 4.5: Transfer probability plotted as a function of the distance of closest approach for the $1n$- and the $2n$-transfer channels (respectively, red and blue full circles) after the energy correction. The data from the previous experiment (empty circles) are shown for comparison.

steps done for the previous part of the analysis. In Fig. 4.6 the angular subdivision is graphically shown. The $\Delta\theta_{MCP} = 1.95°$ was chosen as a compromise between

the request of a fine mapping and the need of enough integrated statistics not to be totally dominated by fluctuations.

	LAB		CM		
n	$\theta_{extremes}$ [°]	θ_{center} [°]	θ^*_{Ni} [°]	θ^*_{Sn} [°]	$D(\theta^*)$ [fm]
0	11.70				
1	13.65	12.675	25.7	154.3	13.00
2	15.60	14.625	29.7	150.3	13.06
3	17.55	16.575	33.7	146.3	13.12
4	19.50	18.525	37.6	142.4	13.20
5	21.45	20.475	41.6	138.4	13.28
6	23.40	22.425	45.6	134.4	13.38
7	25.35	24.375	49.5	130.5	13.49
8	27.30	26.325	53.5	126.5	13.61
9	29.25	28.275	57.5	122.5	13.74
10	31.20	30.225	61.5	118.5	13.89

Table 4.1: Angular subdivision of the MCP with the calculated scattering angles in the center of mass frame for both beam-like and target-like ions. For each angular sector, the corresponding distance of closest approach D is reported.

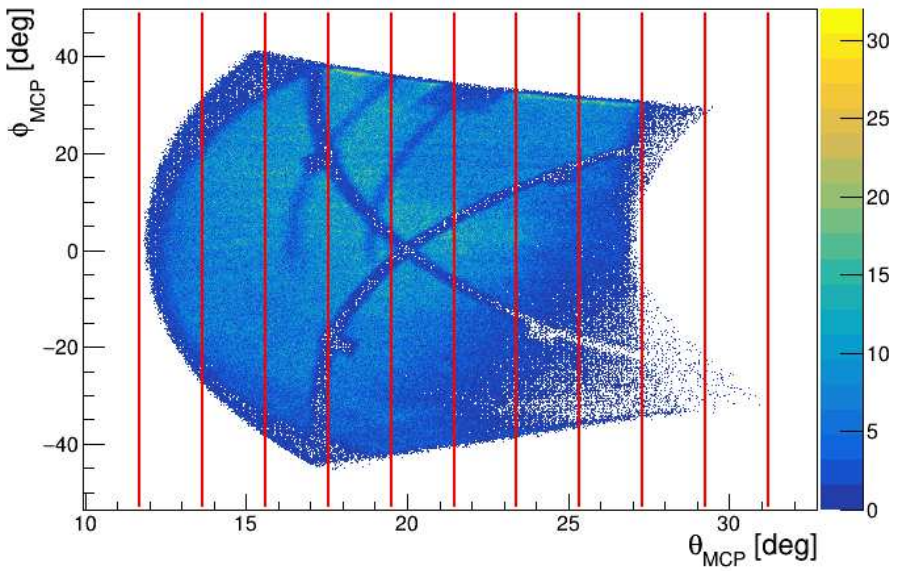

Figure 4.6: θ subdivision of the MCP angular acceptance.

Following this subdivision, the mass distribution are obtained and the peaks are

fitted with the usual procedure. As clearly visible in Fig. 4.6, the angular sectors at higher θ (and consequently lower distance of closest approach) present a lower density of events. This situation led to a mass distribution where it was impossible to fit any peak (see Fig. 4.8) and therefore the last three section are discarded from the plot. The transfer probabilities are therefore obtained and plotted with the previous experiment results for comparison in Fig. 4.7. The results are in good agreement with the previous ones, reproducing the same trend (the slope in logarithmic scale due to the particular form of the transfer probability, see Eq. (1.18)). A deviation can be seen in the last two points at lower distance of closest approach, probably due to boundary effects in the detection (for example, the shape of magnetic and electric fields at the limits of the angular acceptance of the several subdetectors).

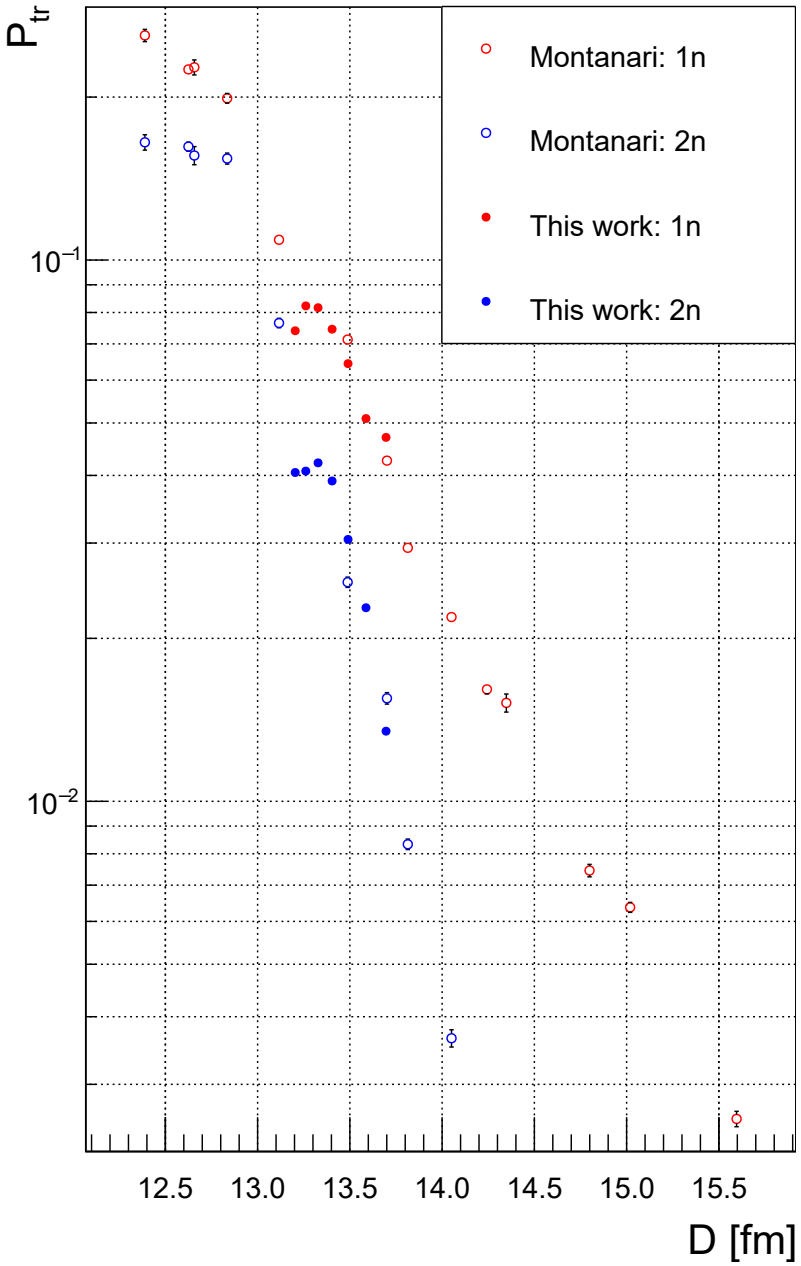

Figure 4.7: Transfer probability plotted as a function of the distance of closest approach for the $1n$- and the $2n$-transfer channels (respectively, red and blue full circles) after the energy correction. The data from the previous experiment (empty circles) are shown for comparison.

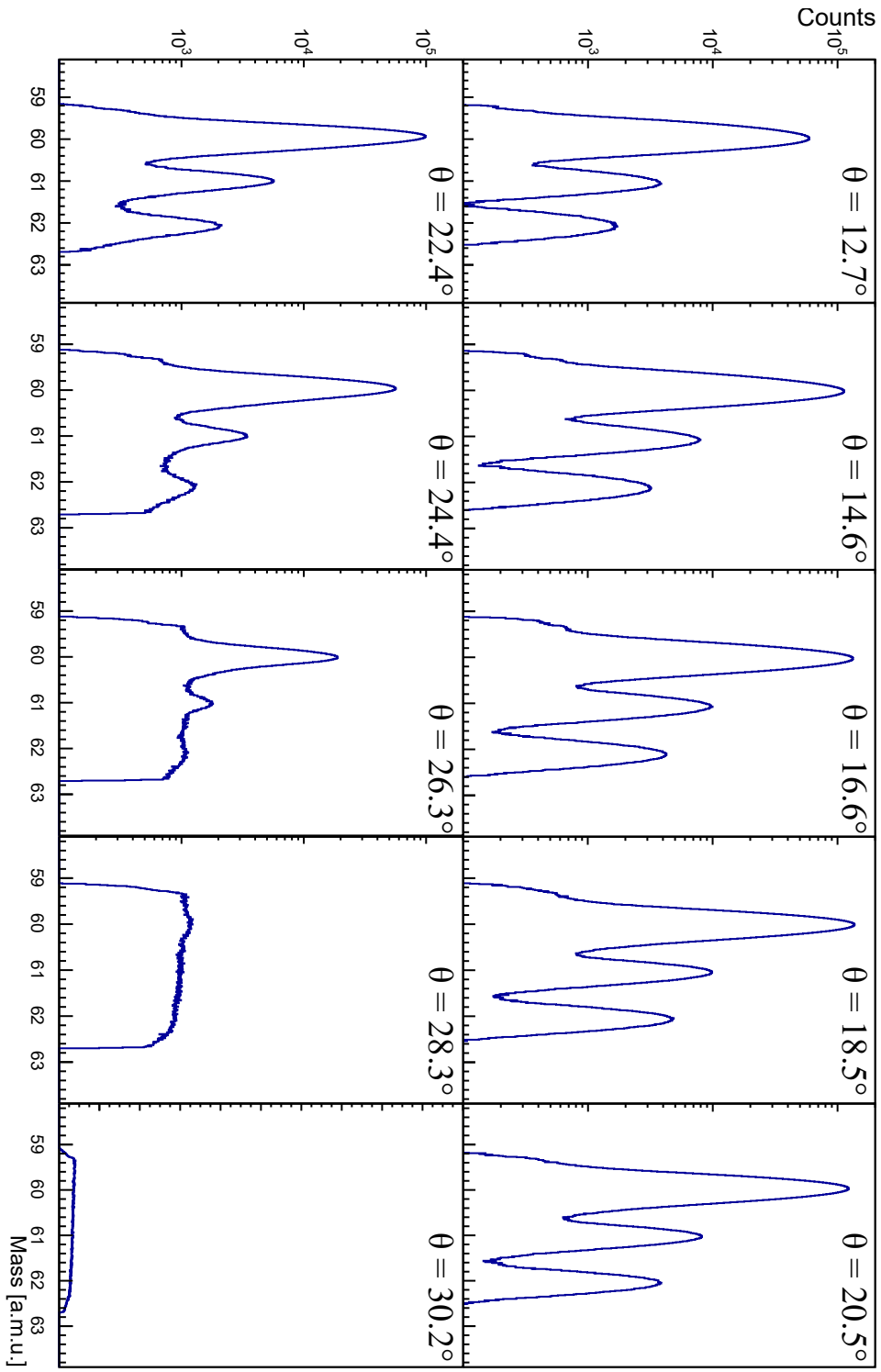

Figure 4.8: Mass distribution, in logarithmic scale, for $Z = 28$ (nickel) gated on the angular variable (MCP angle). At larger angles, the peaks were not recognizable.

4.3 Discrete lines identification

After the calibration and the Doppler-correction optimization of AGATA, information on the observed transitions can be obtained.

The Josephson effect emission is predicted to occur in a wide energy range, including the region where discrete transitions are found. Therefore, the discrete line identification plays a relevant role in the search for the Josephson effect, since a characterization of the γ-ray spectra is necessary to have all the parameters for simulations under control.

As already mentioned, the reaction was performed at sub-barrier energies and with a Q-value matched system: therefore one could expect that most of the $1n$ and $2n$ transfer strength goes to the ground state, with little population of excited states, as was shown in [45]. However, several transitions can be observed; as an example, the Coulomb excitation of both target and projectile. Moreover, the optimum Q-value introduced in Chapter 1 gives a kinematic window for the reaction to occur, and it does not exclude the possibility to produce excited isotopes in the exit channel.

In Fig. 4.10, 4.13 and 4.16 the γ-ray spectra for ^{60,61,62}Ni and for their binary partners (respectively ^{116,115,114}Sn) are presented, with the identified transitions. Let us notice that in all the spectra it is possible to see the contribution of both particles: one of them with the proper Doppler correction, giving rise to the narrow peaks, the other partner with the wrong correction, visible from the broadened structures.

In Tab. from 4.2 to 4.7 the identified transitions are reported, taking the information on the states from the *nndc* database [3], and finally in Fig. from 4.11 to 4.18 the reconstructed level schemes are shown with the observed γ-ray transitions. The dashed lines represent states which were only indirectly observed, since it was not possible to associate γ-rays to the de-excitation of those states.

An interesting feature of the identified transitions is that the reactions populated several states at low angular momentum, in particular 2^+ states. For example, in the ^{114}Sn the sixth 2^+ state was observed. A possible explanation is the fact that the measurements were taken at small angles, in the forward direction, favouring small angular momentum transfer (for large angular momenta, typically one has to detect particles at larger polar angles).

The information obtained from the discrete line identification will be used in the simulation to reproduce the γ-ray spectrum in the channels of interest, combined with the cosmic-ray background, always present. Then, the expected contribution from the Josephson effect could be included: in particular, as already mentioned in the Introduction, the predicted γ-ray distribution is peaked at 4 MeV and has a very large width. However, at those energies the dominant interaction mechanism with the crystals of AGATA is the Compton scattering, therefore a shift towards lower energies is expected in the distribution. The effect can be evaluated through a simple simulation: a Gaussian distribution (blue), that reproduces approximately the predicted JE, is convoluted with the detector response, giving the new distribution (red) shown in Fig. 4.9.

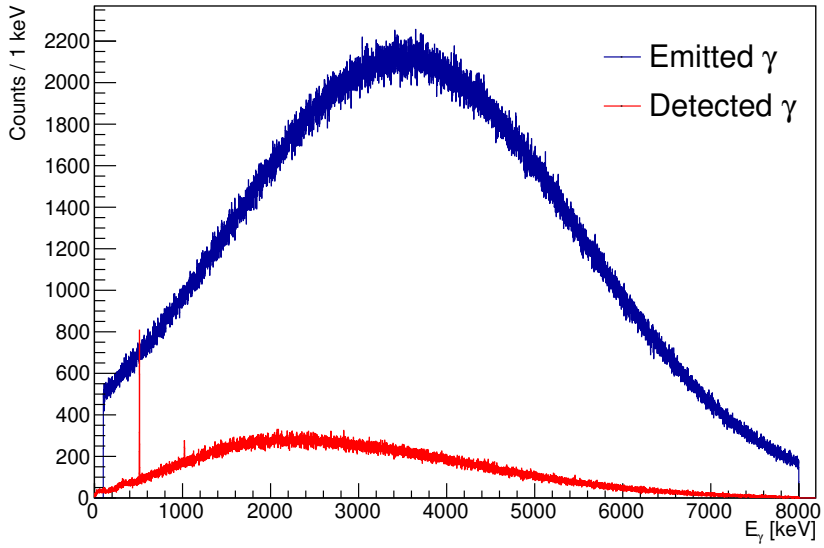

Figure 4.9: Simulated γ-ray strength distribution (blue) and expected shape when convoluted with the detector response (red). Courtesy of Dr. Alain Goasduff.

As visible in the figure, the maximum moved from 4 to around 2 MeV, much closer to the region where the discrete lines lay. This is the main reason why a proper characterization of the spectrum is needed. With this simulations, the high energy region will be investigated, looking for a deviation from the usual cosmic-ray exponential background that could be compatible with the presence of the JE contribution. Finally, a further step will be the angular distribution analysis. Since

this effect is predicted to occur in the fashion of dipole distribution, it could be possible to exploit the AGATA segmentation to reconstruct the angular distribution in θ and ϕ.

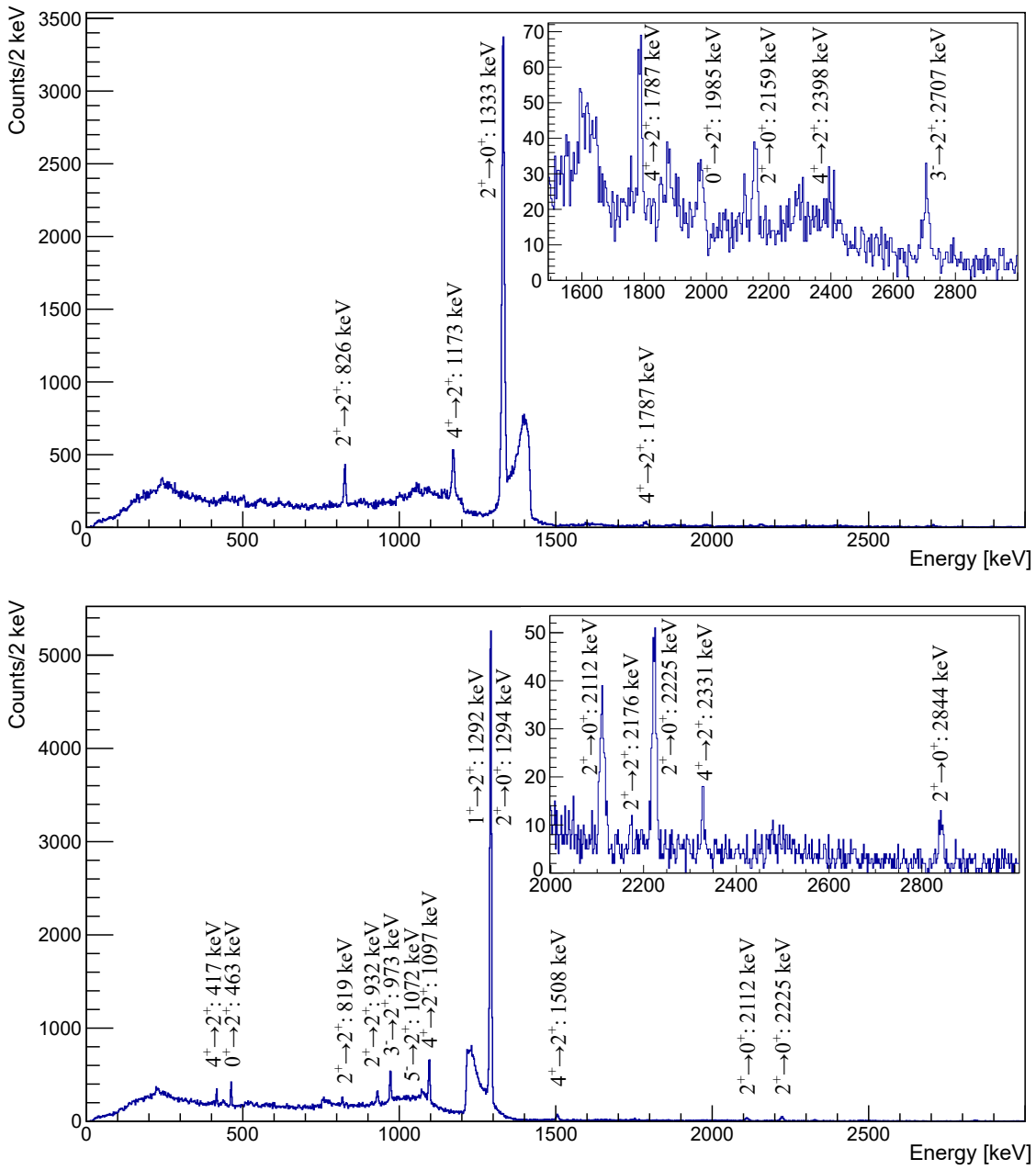

Figure 4.10: γ-ray spectra for ^{60}Ni (top) and ^{116}Sn (bottom) with the identified transitions.

^{60}Ni				
initial level	E_i [keV]	final level	E_f [keV]	E_γ [keV]
2_1^+	1332.5	0_1^+	0.0	1332.5
2_2^+	2158.6	2_1^+	1332.5	826.0
2_2^+	2158.6	0_1^+	0.0	2158.6
4_1^+	2505.8	2_1^+	1332.5	1173.2
4_2^+	3119.9	2_1^+	1332.5	1787.2
0_3^+	3317.8	2_1^+	1332.5	1985.3
4_4^+	3730.8	2_1^+	1332.5	2398.4
3_1^-	4039.9	2_1^+	1332.5	2707.4

Table 4.2: Identified γ-transitions and associated initial and final levels (energy, spin-parity) for ^{60}Ni.

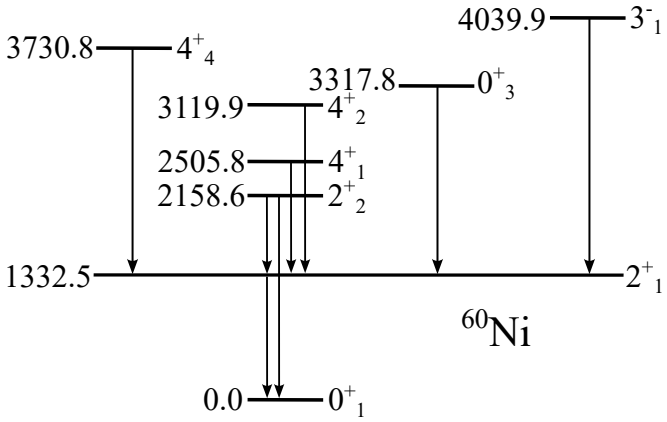

Figure 4.11: Reconstructed ^{60}Ni level scheme from the observed and identified transitions.

^{116}Sn

initial level	E_i [keV]	final level	E_f [keV]	E_γ [keV]
2_1^+	1293.6	0_1^+	0.0	1293.6
0_2^+	1756.9	2_1^+	1293.6	463.3
2_2^+	2112.3	2_1^+	1293.6	818.7
2_2^+	2112.3	0_1^+	0.0	2112.3
2_3^+	2225.4	2_1^+	1293.6	931.8
2_3^+	2225.4	0_1^+	0.0	2225.3
3_1^-	2266.2	2_1^+	1293.6	972.6
5_1^-	2366.0	2_1^+	1293.6	1072.4
4_1^+	2390.9	2_1^+	1293.6	1097.3
4_2^+	2529.2	2_2^+	2112.3	416.9
1_1^+	2585.6	2_1^+	1293.6	1292.0
4_3^+	2801.3	2_1^+	1293.6	1507.7
2_5^+	2843.8	0_1^+	0.0	2843.9
2_{11}^+	3469.6	2_1^+	1293.6	2175.9
4_7^+	3624.6	2_1^+	1293.6	2331.0

Table 4.3: Identified γ-transitions and associated initial and final levels (energy, spin-parity) for ^{116}Sn.

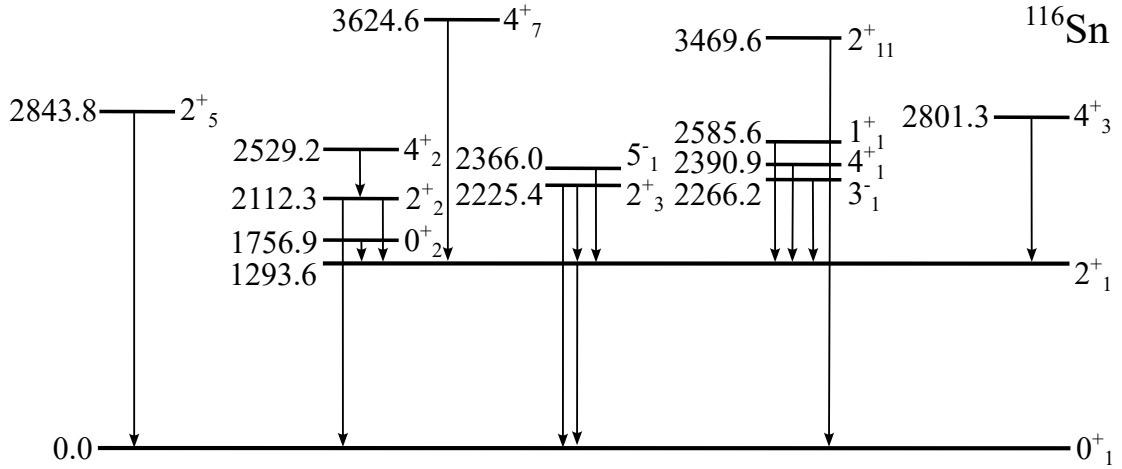

Figure 4.12: Reconstructed ^{116}Sn level scheme from the observed and identified transitions.

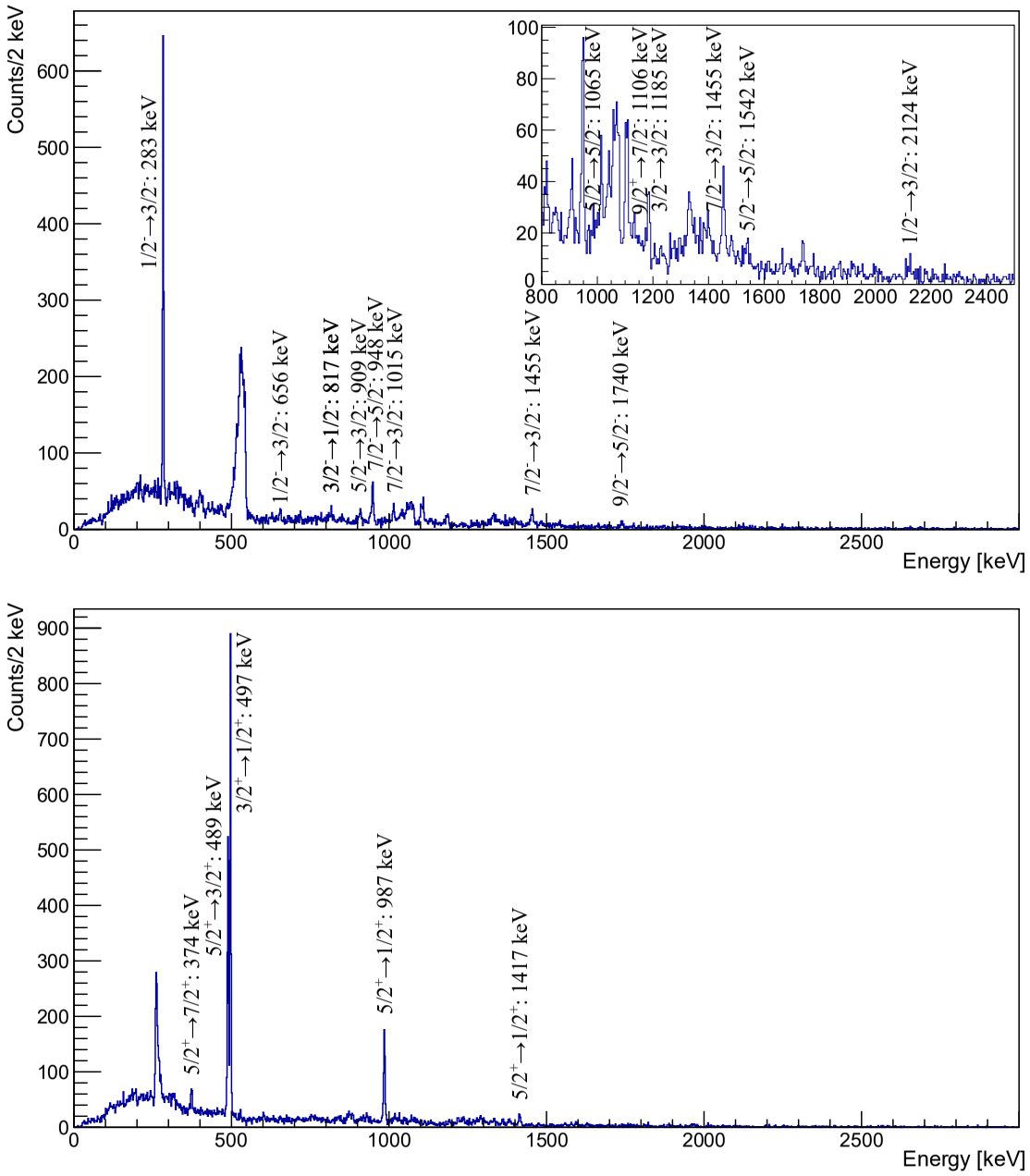

Figure 4.13: γ-ray spectra for ^{61}Ni (top) and ^{115}Sn (bottom) with the identified transitions.

^{61}Ni

initial level	E_i [keV]	final level	E_f [keV]	E_γ [keV]
$1/2^-_1$	283.0	$3/2^-_1$	0.0	283.0
$1/2^-_2$	656.0	$3/2^-_1$	0.0	656.0
$5/2^-_2$	908.6	$3/2^-_1$	0.0	908.6
$7/2^-_1$	1015.2	$5/2^-_1$	67.4	947.9
$7/2^-_1$	1015.2	$3/2^-_1$	0.0	1015.1
$3/2^-_2$	1099.6	$1/2^-_1$	283.0	816.7
$5/2^-_3$	1132.3	$5/2^-_1$	67.4	1064.9
$3/2^-_3$	1185.3	$3/2^-_1$	0.0	1185.2
$7/2^-_2$	1454.8	$3/2^-_1$	0.0	1454.8
$5/2^-_4$	1609.7	$5/2^-_1$	67.4	1542.3
$9/2^-_1$	1807.9	$5/2^-_1$	67.4	1740.3
$9/2^+_1$	2121.5	$7/2^-_1$	1015.2	1106.3
$1/2^-_3$	2123.9	$3/2^-_1$	0.0	2123.9

Table 4.4: Identified γ-transitions and associated initial and final levels (energy, spin-parity) for ^{61}Ni.

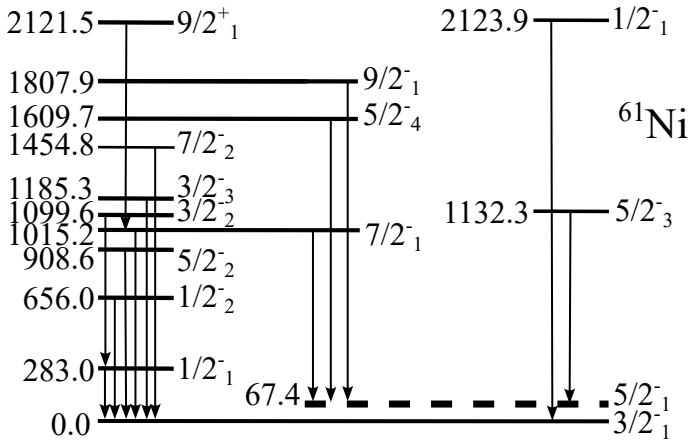

Figure 4.14: Reconstructed ^{61}Ni level scheme from the observed and identified transitions.

^{115}Sn				
initial level	E_i [keV]	final level	E_f [keV]	E_γ [keV]
$3/2_1^+$	497.3	$1/2_1^+$	0.0	497.4
$5/2_1^+$	986.6	$7/2_1^+$	612.8	373.8
$5/2_1^+$	986.6	$3/2_1^+$	497.3	489.3
$5/2_1^+$	986.6	$1/2_1^+$	0.0	986.5
$5/2_2^+$	1416.9	$1/2_1^+$	0.0	1416.8

Table 4.5: Identified γ-transitions and associated initial and final levels (energy, spin-parity) for ^{115}Sn.

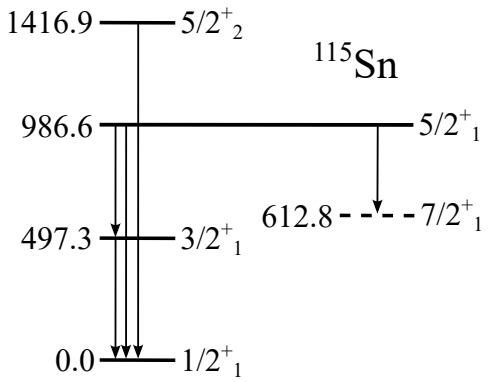

Figure 4.15: Reconstructed ^{115}Sn level scheme from the observed and identified transitions.

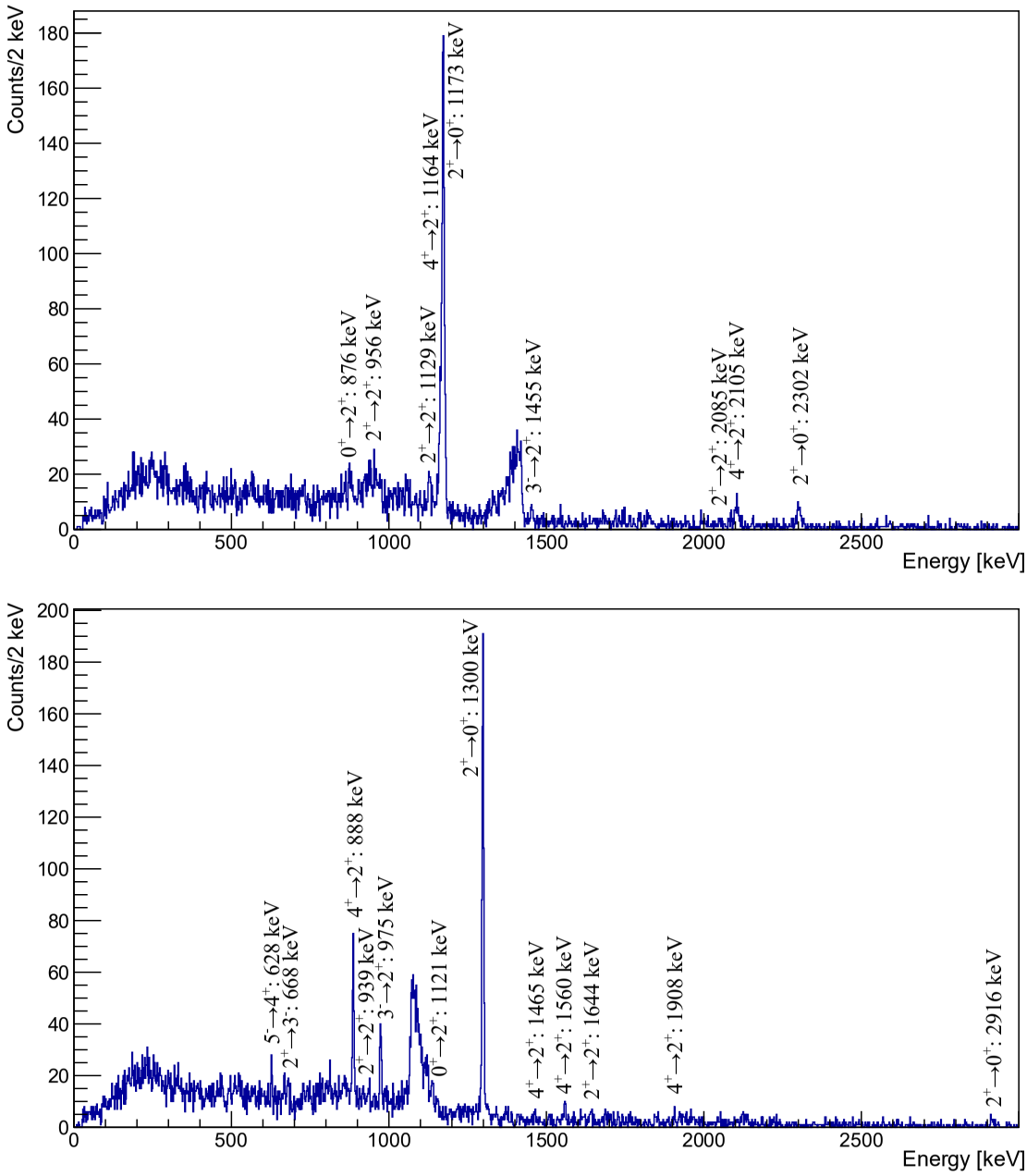

Figure 4.16: γ-ray spectra for ^{62}Ni (top) and ^{114}Sn (bottom) with the identified transitions.

^{62}Ni

initial level	E_i [keV]	final level	E_f [keV]	E_γ [keV]
2_1^+	1173.0	0_1^+	0.0	1173.0
0_2^+	2048.7	2_1^+	1173.0	875.7
2_2^+	2301.8	2_1^+	1173.0	1128.8
2_2^+	2301.8	0_1^+	0.0	2301.8
4_1^+	2336.5	2_1^+	1173.0	1163.5
2_4^+	3257.6	2_2^+	2301.8	955.7
2_4^+	3257.6	2_1^+	1173.0	2084.8
4_3^+	3277.7	2_1^+	1173.0	2104.5
3_1^-	3756.5	2_2^+	2301.8	1454.5

Table 4.6: Identified γ-transitions and associated initial and final levels (energy, spin-parity) for ^{62}Ni.

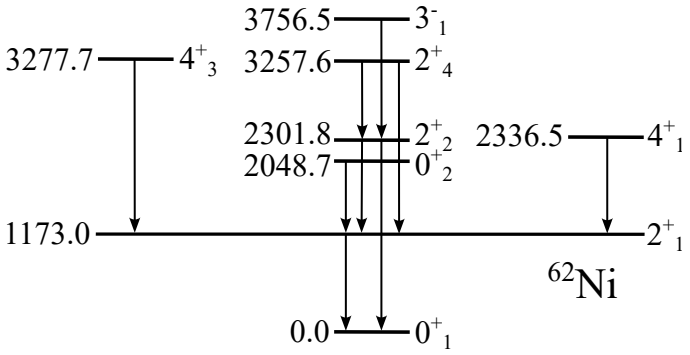

Figure 4.17: Reconstructed ^{62}Ni level scheme from the observed and identified transitions.

^{114}Sn

initial level	E_i [keV]	final level	E_f [keV]	E_γ [keV]
2_1^+	1299.9	0_1^+	0.0	1299.9
4_1^+	2187.6	2_1^+	1299.9	887.7
2_2^+	2239.0	2_1^+	1299.9	939.0
3_1^-	2275.0	2_1^+	1299.9	975.1
0_4^+	2421.7	2_1^+	1299.9	1121.4
4_3^+	2765.4	2_1^+	1299.9	1465.4
5_1^-	2815.1	4_1^+	2187.6	627.5
4_4^+	2859.8	2_1^+	1299.9	1559.9
2_5^+	2915.7	0_1^+	0.0	2915.6
2_6^+	2943.4	3_1^-	2275.0	668.4
2_6^+	2943.4	2_1^+	1299.9	1643.6
4_5^+	3207.6	2_1^+	1299.9	1907.8

Table 4.7: Identified γ-transitions and associated initial and final levels (energy, spin-parity) for ^{114}Sn.

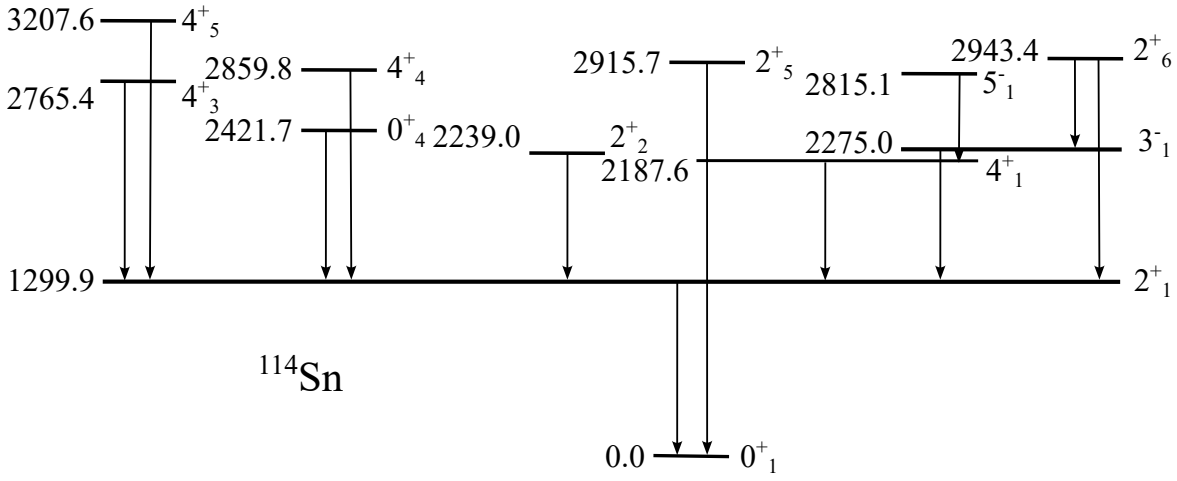

Figure 4.18: Reconstructed ^{114}Sn level scheme from the observed and identified transitions.

5

Conclusions and perspectives

In this work, the data analysis from the ^{116}Sn + ^{60}Ni experiment performed in February 2023 was presented. The coupling of the PRISMA magnetic spectrometer and the AGATA γ-ray tracking array was employed for the data acquisition, in combination with a set of $LaBr_3$ scintillators and a pin silicon detector for measuring the elastic scattering. The aim of the experiment was to observe a nuclear Josephson effect, predicted by a BCS-like theory for atomic nuclei. The reaction of interest involved two superfluid nuclei interacting at an energy below the Coulomb barrier, in order to reproduce a nuclear analogue of the Josephson junction, where Cooper pairs of identical particles are transferred from one system to the other via tunneling across a thin potential barrier. Among all the possible reactions, the quasi-elastic channel and the one- and two-neutron transfer processes, populating three different nickel isotopes (^{60,61,62}Ni), were studied.

The calibration of all detectors was performed online during the experiment and then improved in the offline analysis. Exploiting the ΔE-E and the E-$R\beta$ matrices, data were sorted in order to select the nuclear charge Z and the atomic charge state q. A consistent part of the work included the aberration correction of magnetic fields, the optimization of the PRISMA optical parameters and the alignment and calibration procedures for the TOF and the A/q variables. For AGATA, the TOF correction was applied in order to obtain a Doppler-corrected energy of the detected γ-rays.

The mass distributions were obtained from PRISMA data and, hence, a first effect of the pairing interaction was observed by comparing the relative height of the peaks associated to different reaction channels. In the case of Fe and Cu isotopes, the mass spectra indicated an enhanced 2-neutron transfer channel with respect to the single-neutron transfer process. The transfer probabilities for the Ni isotopes align with reference values, obtained from a former experiment, that proved the presence of pairing correlation between pair of transferred neutrons. Such an agreement is essential since it ensures favorable conditions for the measurement of the γ-ray emission associated with the Josephson Effect.

Finally, the γ-ray spectra were obtained from AGATA and, by selecting the reaction channels, discrete lines were identified for the following nuclear systems: ^{60,61,62}Ni and ^{116,115,114}Sn. This is a fundamental step for the analysis. In fact, the identified discrete γ-ray transitions, together with the cosmic-ray contribution, can be included in a simulation to determine whether any significant deviation emerges from the trend of the background, especially in the high-energy region of the spectrum, where the emission due to a Josephson Effect is located. In addition, the angular distribution of the emission could be measured and checked against the expected dipole behaviour, after having identified the fraction of γ rays due to the Josephson Effect.

References

[1] A. Obertelli and H. Sagawa, *Nuclear Reactions*. Singapore: Springer Singapore, 2021, pp. 535–634. [Online]. Available: https://doi.org/10.1007/978-981-16-2289-2_8

[2] G. Montagnoli, "Lecture notes in nuclear reactions," September 2020.

[3] "NNDC," July 2023. [Online]. Available: https://www.nndc.bnl.gov/nudat3/

[4] L. Corradi, S. Szilner, and G. Pollarolo, "Evidence of proton-proton correlations in the ^{60}Ni $+^{116}$ Sn transfer reactions," *Physics Letters B*, vol. 834, p. 137477, 2022. [Online]. Available: https://www.sciencedirect.com/science/article/pii/S0370269322006116

[5] G. Potel, F. Barranco, and E. Vigezzi, "Quantum entanglement in nuclear Cooper-pair tunneling with γ rays," *Phys. Rev. C*, vol. 103, p. L021601, Feb 2021. [Online]. Available: https://link.aps.org/doi/10.1103/PhysRevC.103.L021601

[6] J. Valiente-Dobón, R. Menegazzo, and A. Goasduff, "Conceptual design of the AGATA 2π array at LNL," *Nuclear Instruments and Methods in Physics Research Section A: Accelerators, Spectrometers, Detectors and Associated Equipment*, vol. 1049, p. 168040, 2023. [Online]. Available: https://www.sciencedirect.com/science/article/pii/S016890022300030X

[7] G. Montagnoli, A. Stefanini, and M. Trotta, "The large-area micro-channel plate entrance detector of the heavy-ion magnetic spectrometer PRISMA," *Nuclear Instruments and Methods in Physics Research Section A: Accelerators, Spectrometers, Detectors and Associated Equipment*, vol. 547, no. 2, pp. 455–463, 2005. [Online]. Available: https://www.sciencedirect.com/science/article/pii/S0168900205009241

[8] S. Beghini, L. Corradi, and E. Fioretto, "The focal plane detector of the magnetic spectrometer PRISMA," *Nuclear Instruments and Methods in Physics Research Section A: Accelerators, Spectrometers, Detectors and Associated Equipment*, vol. 551, no. 2, pp. 364–374, 2005. [Online]. Available: https://www.sciencedirect.com/science/article/pii/S0168900205013501

[9] S. Akkoyun, A. Algora, and B. Alikhani, "AGATA—Advanced GAmma Tracking Array," *Nuclear Instruments and Methods in Physics Research Section A: Accelerators, Spectrometers, Detectors and Associated Equipment*, vol. 668, pp. 26–58, 2012. [Online]. Available: https://www.sciencedirect.com/science/article/pii/S0168900211021516

[10] A. Stefanini, L. Corradi, and G. Maron, "The heavy-ion magnetic spectrometer PRISMA," *Nuclear Physics A*, vol. 701, no. 1, pp. 217–221, 2002, 5th International Conference on Radioactive Nuclear Beams. [Online]. Available: https://www.sciencedirect.com/science/article/pii/S0375947401015780

[11] A. Bohr, B. R. Mottelson, and D. Pines, "Possible analogy between the excitation spectra of nuclei and those of the superconducting metallic state," *Phys. Rev.*, vol. 110, pp. 936–938, May 1958. [Online]. Available: https://link.aps.org/doi/10.1103/PhysRev.110.936

[12] T. Duguet, P. Bonche, and P.-H. Heenen, "Pairing correlations. II. Microscopic analysis of odd-even mass staggering in nuclei," *Phys. Rev. C*, vol. 65, p. 014311, Dec 2001. [Online]. Available: https://link.aps.org/doi/10.1103/PhysRevC.65.014311

[13] L. N. Cooper, "Bound electron pairs in a degenerate Fermi gas," *Phys. Rev.*, vol. 104, pp. 1189–1190, Nov 1956. [Online]. Available: https://link.aps.org/doi/10.1103/PhysRev.104.1189

[14] J. Bardeen, L. N. Cooper, and J. R. Schrieffer, "Theory of superconductivity," *Phys. Rev.*, vol. 108, pp. 1175–1204, Dec 1957. [Online]. Available: https://link.aps.org/doi/10.1103/PhysRev.108.1175

[15] B. R. Mottelson and J. G. Valatin, "Effect of Nuclear Rotation on the Pairing Correlation," *Phys. Rev. Lett.*, vol. 5, pp. 511–512, Dec 1960. [Online]. Available: https://link.aps.org/doi/10.1103/PhysRevLett.5.511

[16] F. Stephens and R. Simon, "Coriolis effects in the yrast states," *Nuclear Physics A*, vol. 183, no. 2, pp. 257–284, 1972. [Online]. Available: https://www.sciencedirect.com/science/article/pii/0375947472906586

[17] A. Johnson, H. Ryde, and J. Sztarkier, "Evidence for a "singularity" in the nuclear rotational band structure," *Physics Letters B*, vol. 34, no. 7, pp. 605–608, 1971. [Online]. Available: https://www.sciencedirect.com/science/article/pii/037026937190150X

[18] B. Josephson, "Possible new effects in superconductive tunnelling," *Physics Letters*, vol. 1, no. 7, pp. 251–253, 1962. [Online]. Available: https://www.sciencedirect.com/science/article/pii/0031916362913690

[19] V. L. Ginzburg and L. D. Landau, "On the theory of superconductivity," D. T. Haar, Ed. Pergamon, 1965, pp. 546–568. [Online]. Available: https://www.sciencedirect.com/science/article/pii/B978008010586450078X

[20] K. Dietrich, "Semiclassical theory of a nuclear Josephson effect in reactions between heavy ions," *Annals of Physics*, vol. 66, no. 2, pp. 480–508, 1971. [Online]. Available: https://www.sciencedirect.com/science/article/pii/0003491671900674

[21] L. Landau, "The Theory of Phase Transitions," *Nature*, vol. 138, pp. 840–841, 11 1936. [Online]. Available: https://doi.org/10.1038/138840a0

[22] L. P. Gor'kov, "Developing BCS ideas in the former Soviet Union," in *BCS: 50 Years*. World Scientific, nov 2010, pp. 107–126. [Online]. Available: https://doi.org/10.1142%2F9789814304665_0007

[23] V. L. Pokrovskii, "Works by A. I. Larkin on the theory of phase transitions," *Journal of Experimental and Theoretical Physics*, vol. 117, pp. 387–391, 2013. [Online]. Available: https://doi.org/10.1134/S1063776113110149

[24] M. Gaudin, "Fission: Asymétrie de masse et superconductivité," *Nuclear Physics A*, vol. 144, no. 1, pp. 191–199, 1970. [Online]. Available: https://www.sciencedirect.com/science/article/pii/0375947470905002

[25] R. F. Casten, *Nuclear Structure from a Simple Perspective; 1st ed.* New York, NY: Oxford Univ. Press, 1990. [Online]. Available: https://cds.cern.ch/record/1034679

[26] G. Potel, A. Idini, and F. Barranco, "Cooper pair transfer in nuclei," *Reports on Progress in Physics*, vol. 76, no. 10, p. 106301, oct 2013. [Online]. Available: https://dx.doi.org/10.1088/0034-4885/76/10/106301

[27] S. Frauendorf and A. Macchiavelli, "Overview of neutron–proton pairing," *Progress in Particle and Nuclear Physics*, vol. 78, pp. 24–90, 2014. [Online]. Available: https://www.sciencedirect.com/science/article/pii/S0146641014000465

[28] M. Born, "Quantenmechanik der Stoßvorgänge," *Zeitschrift für Physik*, vol. 38, pp. 803–827, 1926.

[29] L. Corradi, G. Pollarolo, and S. Szilner, "Multinucleon transfer processes in heavy-ion reactions," *Journal of Physics G: Nuclear and Particle Physics*, vol. 36, no. 11, p. 113101, sep 2009. [Online]. Available: https://dx.doi.org/10.1088/0954-3899/36/11/113101

[30] W. von Oertzen and A. Vitturi, "Pairing correlations of nucleons and multi-nucleon transfer between heavy nuclei," *Reports on Progress in Physics*, vol. 64, no. 10, p. 1247, sep 2001. [Online]. Available: https://dx.doi.org/10.1088/0034-4885/64/10/202

[31] D. Montanari, L. Corradi, and S. Szilner, "Neutron pair transfer in ^{60}Ni $+^{116}$ Sn far below the coulomb barrier," *Phys. Rev. Lett.*, vol. 113, p. 052501, Jul 2014. [Online]. Available: https://link.aps.org/doi/10.1103/PhysRevLett.113.052501

[32] S. Raman, C. Nestor, and P. Tikkanen, "Transition probability from the ground to the first-excited 2^+ state of even-even nuclides," *Atomic Data and*

Nuclear Data Tables, vol. 78, no. 1, pp. 1–128, 2001. [Online]. Available: https://www.sciencedirect.com/science/article/pii/S0092640X01908587

[33] L. Corradi, S. Szilner, and E. Fioretto, "Search for a Josephson like effect in the ^{60}Ni +^{116} Sn system," February 2021, proposal n. 28 for a PRISMA+AGATA experiment, LNL PAC.

[34] "Advanced GAmma Tracking Array (AGATA) - official website," August 2023. [Online]. Available: https://www.agata.org

[35] L. Corradi, S. Szilner, and G. Pollarolo, "Multinucleon transfer reactions: Present status and perspectives," *Nuclear Instruments and Methods in Physics Research Section B: Beam Interactions with Materials and Atoms*, vol. 317, pp. 743–751, 2013, XVIth International Conference on ElectroMagnetic Isotope Separators and Techniques Related to their Applications, December 2–7, 2012 at Matsue, Japan. [Online]. Available: https://www.sciencedirect.com/science/article/pii/S0168583X13006976

[36] H. Bethe, "Bremsformel für Elektronen relativistischer Geschwindigkeit," *Zeitschrift für Physik*, vol. 76, pp. 293–299, 1932.

[37] S. Paschalis, I. Lee, and A. Macchiavelli, "The performance of the Gamma-Ray Energy Tracking In-beam Nuclear Array GRETINA," *Nuclear Instruments and Methods in Physics Research Section A: Accelerators, Spectrometers, Detectors and Associated Equipment*, vol. 709, pp. 44–55, 2013. [Online]. Available: https://www.sciencedirect.com/science/article/pii/S0168900213000508

[38] A. Gadea, E. Farnea, and J. Valiente-Dobón, "Conceptual design and infrastructure for the installation of the first AGATA sub-array at LNL," *Nuclear Instruments and Methods in Physics Research Section A: Accelerators, Spectrometers, Detectors and Associated Equipment*, vol. 654, no. 1, pp. 88–96, 2011. [Online]. Available: https://www.sciencedirect.com/science/article/pii/S0168900211011132

[39] C. Domingo-Pardo, D. Bazzacco, and P. Doornenbal, "Conceptual design and performance study for the first implementation of AGATA

at the in-flight RIB facility of GSI," *Nuclear Instruments and Methods in Physics Research Section A: Accelerators, Spectrometers, Detectors and Associated Equipment*, vol. 694, pp. 297–312, 2012. [Online]. Available: https://www.sciencedirect.com/science/article/pii/S0168900212009102

[40] E. Clément, C. Michelagnoli, and G. de France, "Conceptual design of the AGATA 1 array at GANIL," *Nuclear Instruments and Methods in Physics Research Section A: Accelerators, Spectrometers, Detectors and Associated Equipment*, vol. 855, pp. 1–12, 2017. [Online]. Available: https://www.sciencedirect.com/science/article/pii/S0168900217302590

[41] A. Wiens, H. Hess, and B. Birkenbach, "The AGATA triple cluster detector," *Nuclear Instruments and Methods in Physics Research Section A: Accelerators, Spectrometers, Detectors and Associated Equipment*, vol. 618, no. 1, pp. 223–233, 2010. [Online]. Available: https://www.sciencedirect.com/science/article/pii/S0168900210003384

[42] O. Klein and Y. Nishina, "Über die Streuung von Strahlung durch freie Elektronen nach der neuen relativistischen Quantendynamik von Dirac," *Zeitschrift für Physik*, vol. 52, pp. 853–868, 1929.

[43] R. M. Pérez Vidal, "Collectivity along N=50: Nuclear Structure studies on the neutron-magic nuclei ^{92}Mo and ^{94}Ru with AGATA and VAMOS++," October 2019, PhD Thesis.

[44] "LISE++," September 2023. [Online]. Available: https://lise.nscl.msu.edu/lise.html

[45] D. Montanari, L. Corradi, and S. Szilner, "Pair neutron transfer in ^{60}Ni + ^{116}Sn probed via γ-particle coincidences," *Phys. Rev. C*, vol. 93, p. 054623, May 2016. [Online]. Available: https://link.aps.org/doi/10.1103/PhysRevC.93.054623

A

Appendix: the Ginzburg-Landau theory and the JE derivation

A.1 The Ginzburg-Landau theory

From Ginzburg-Landau theory [19], the free energy of the system can be written as

$$F = F_n + \alpha|\psi|^2 + \frac{\beta}{2}|\psi|^4 + \frac{1}{2m^*}|(-i\hbar\nabla - e^*\mathbf{A})\psi|^2 + \frac{|\mathbf{B}|^2}{2\mu_0} \tag{A.1}$$

where F_n is the free energy in the normal phase, α and β are two phenomenological parameters to account for the superconducting phase, m^* and e^* are respectively the effective mass and charge in the kinetic term, and finally the last term is the magnetic term.

In the formula above, $\psi = |\psi|e^{i\phi(\mathbf{r})}$ is a complex *order parameter*, which contains the information on the electron density ($|\psi|^2$).

Requiring an invariance condition, i.e.

$$\frac{\partial F}{\partial \psi} = 2\alpha\psi + 2\beta|\psi|^2\psi + \frac{1}{m^*}|(-i\hbar\nabla - e^*\mathbf{A})|^2\psi = 0 \tag{A.2}$$

and the validity of Maxwell equations, a system of coupled equations is obtained:

$$\begin{cases} \alpha\psi + \beta|\psi|^2\psi + \frac{1}{2m^*}|(-i\hbar\nabla - e^*\mathbf{A})|^2\psi = 0 \\ \nabla \times \mathbf{B} = \mu_0\mathbf{j}\ , \quad \mathbf{j} = \frac{e^*}{m^*}\mathfrak{Re}[\psi^*(-i\hbar\nabla - e^*\mathbf{A})\psi] \end{cases} \tag{A.3}$$

where the $\mathbf{j}$ assumes the meaning of superconducting current.

In the case of no net current ($\mathbf{j} = 0$), the equations reduce to $\alpha\psi + \beta|\psi|^2\psi = 0$, which has two possible solutions:

- $\psi \equiv 0$: normal conducting, $T > T_c$
- $|\psi|^2 = -\frac{\alpha}{\beta}$: superconducting, $T < T_c$, with

$$\alpha(T) = \alpha_0(T - T_c)\ ,\ \frac{\alpha_0}{\beta} > 0\ ,\ |\psi|^2 = -\frac{\alpha_0(T - T_c)}{\beta} \tag{A.4}$$

The phase transition between normal-conducting and superconducting regime is therefore associated to the change in order parameter, from 0 to a non-zero value.

At this point, a couple of characteristic lengths can be defined:

- Coherence length:

$$\xi = \begin{cases} \sqrt{\frac{\hbar^2}{2m^*|\alpha|}}\ ,\ T > T_c \\ \sqrt{\frac{\hbar^2}{4m^*|\alpha|}}\ ,\ T < T_c \end{cases} \quad . \tag{A.5}$$

- (London) Penetration length:

$$\lambda = \sqrt{\frac{m^*}{\mu_0 e^{*2}\psi_0^2}} = \sqrt{\frac{m^*\beta}{\mu_0 e^{*2}|\alpha|}} \tag{A.6}$$

The coherence length is the characteristic quantity that sets the exponential law according to which small perturbations of density of superconducting electrons recover their equilibrium value. From a microscopic point of view, it represents the maximum spatial dimension of a Cooper pair, i.e. the maximum distance at which two electrons can be described as a single coherent quantum state. Instead, the penetration depth id related to the exponential law describing the decay of an external magnetic field inside the superconductor.

A.2 The Josephson Effect

Starting from the Schr odinger equation for the two coupled superconductors

$$i\hbar\partial_t \begin{pmatrix} \sqrt{n_A}e^{i\phi_A(\mathbf{r})} \\ \sqrt{n_B}e^{i\phi_B(\mathbf{r})} \end{pmatrix} = \begin{pmatrix} eV & K \\ K & -eV \end{pmatrix} \begin{pmatrix} \sqrt{n_A}e^{i\phi_A(\mathbf{r})} \\ \sqrt{n_B}e^{i\phi_B(\mathbf{r})} \end{pmatrix} \tag{A.7}$$

and by using

$$\partial_t\psi_A = \dot{\sqrt{n_A}}e^{i\phi_A} + \sqrt{n_A}i\dot{\phi}_A e^{i\phi_A} = (\dot{\sqrt{n_A}} + \sqrt{n_A}i\dot{\phi}_A)e^{i\phi_A} \tag{A.8}$$

the first element of the matrix reads

$$(\dot{\sqrt{n_A}} + \sqrt{n_A}i\dot{\phi}_A)e^{i\phi_A} = \frac{1}{i\hbar}(eV\sqrt{n_A}e^{i\phi_A} + K\sqrt{n_B}e^{i\phi_B}) \tag{A.9}$$

The Josephson phase can be defined as $\varphi = \phi_B - \phi_A$; in this way, a single phase is sufficient to describe the system. Taking Eq. (A.9) and its complex conjugated:

$$\begin{cases} \dot{\sqrt{n_A}} + i\sqrt{n_A}\dot{\phi}_A = \frac{1}{i\hbar}(eV\sqrt{n_A} + K\sqrt{n_B}e^{i\varphi}) \\ \dot{\sqrt{n_A}} - i\sqrt{n_A}\dot{\phi}_A = -\frac{1}{i\hbar}(eV\sqrt{n_A} + K\sqrt{n_B}e^{-i\varphi}) \end{cases} \tag{A.10}$$

Summing up the two equations,

$$2\dot{\sqrt{n_A}} = \frac{K}{i\hbar}\sqrt{n_B}(e^{i\varphi} - e^{-i\varphi}) = 2\frac{K\sqrt{n_B}}{\hbar}\sin\varphi \tag{A.11}$$

The derivative of the square root is $\dot{\sqrt{n_A}} = \frac{\dot{n_A}}{2\sqrt{n_A}}$, therefore

$$\dot{\sqrt{n_A}} = \frac{2K\sqrt{n_A n_B}}{\hbar}\sin\varphi \tag{A.12}$$

By subtracting the two equations in Eq. (A.10),

$$2i\sqrt{n_A}\dot{\phi}_A = \frac{1}{i\hbar}(2eV\sqrt{n_A} + K\sqrt{n_B}\cos\varphi) \tag{A.13}$$

from which the time derivative of the phase ϕ_A reads

$$\dot{\phi}_A = -\frac{1}{\hbar}\left(eV + K\sqrt{\frac{n_B}{n_A}}\cos\varphi\right) \tag{A.14}$$

The same procedure can be applied for the superconductor B, leading to this set of equations:

$$\begin{cases} \dot{\sqrt{n_A}} = \frac{2K\sqrt{n_A n_B}}{\hbar}\sin\varphi \\ \dot{\phi}_A = -\frac{1}{\hbar}\left(eV + K\sqrt{\frac{n_B}{n_A}}\cos\varphi\right) \end{cases} \qquad \begin{cases} \dot{\sqrt{n_B}} = -\frac{2K\sqrt{n_A n_B}}{\hbar}\sin\varphi \\ \dot{\phi}_B = \frac{1}{\hbar}\left(eV - K\sqrt{\frac{n_B}{n_A}}\cos\varphi\right) \end{cases} \tag{A.15}$$

Now, the time derivative of the Josephson phase becomes

$$\dot{\varphi} = \dot{\phi}_B - \dot{\phi}_A = \frac{2eV}{\hbar} \tag{A.16}$$

In this way it is possible to see how the phase evolves with time; this will lead also to the variation of the carriers concentrations ($\dot{\sqrt{n_A}}$ and $\dot{\sqrt{n_B}}$), which are basically related to a current. Therefore,

$$I(t) = I_C \sin\varphi(t) \tag{A.17}$$

where I_C is the critical current. A new parameter can be defined: the Josephson constant $K_J = \frac{2e}{h}$, which is in practice an inverse magnetic flux; indeed, $\Phi_0 = 1/K_J = \frac{h}{2e} = 2\pi\frac{\hbar}{2e}$ (magnetic flux quantum, *fluxon*). Therefore, the Josephson phase variation can be expressed in terms of this parameter as

$$\dot{\varphi} = 2\pi[K_J V(t)] = \frac{2\pi}{\Phi_0}V(t) \tag{A.18}$$

and

$$\Phi = \Phi_0\frac{\varphi}{2\pi} \tag{A.19}$$

from which

$$V = \frac{\Phi_0}{2\pi}\dot{\varphi} = \dot{\Phi} \tag{A.20}$$

which resembles a Faraday-like law.

This derivation is general. The two most known effects come from two particular

cases: $V(t) = 0$ (Direct Current Josephson Effect, DCJE) and $V(t) = V_0$ (Alternate Current Josephson Effect, ACJE). In the first case, being $V = 0$, the Josephson phase is kept constant ($\dot{\varphi} = 0$), so the total effect is a direct current flowing between the two superconductors. In the second case, there is a linear variation of the phase, which produces an alternating sinusoidal current.

Another interesting quantity can be defined studying the problem from the energetic point of view. Since $I = I_C \sin\varphi$ and $V = \frac{\mathrm{d}\Phi}{\mathrm{d}t}$, a change of phase $\varphi_1 \longrightarrow \varphi_2$ (from t_1 to t_2 in time) can be associated to a variation in energy:

$$\Delta E = \int_{t_1}^{t_2} IV \,\mathrm{d}t = \int_{\Phi_1}^{\Phi_2} I \,\mathrm{d}\Phi = \int_{\varphi_1}^{\varphi_2} I_C \sin\varphi \,\mathrm{d}\left(\Phi_0 \frac{\varphi}{2\pi}\right) = -\frac{\Phi_0 I_C}{2\pi} \Delta \cos\varphi \quad \text{(A.21)}$$

This shows that the energy stored in the junction is a state function, depending only on the initial and final states. An energy can be defined:

$$E(\varphi) = -E_J \cos\varphi \qquad \text{or} \qquad E_J(1 - \cos\varphi) \quad \text{(A.22)}$$

where the amplitude is the *Josephson energy* and is the characteristic energy of the system

$$E_J = |E(0)| = \frac{\Phi_0 I_C}{2\pi} \quad \text{(A.23)}$$

This energy comes from the kinetic energy of the paired electrons inside the superconductor and not to the magnetic field in the free energy expression.

B

Appendix: Calibration an settings of PRISMA

B.1 MCP

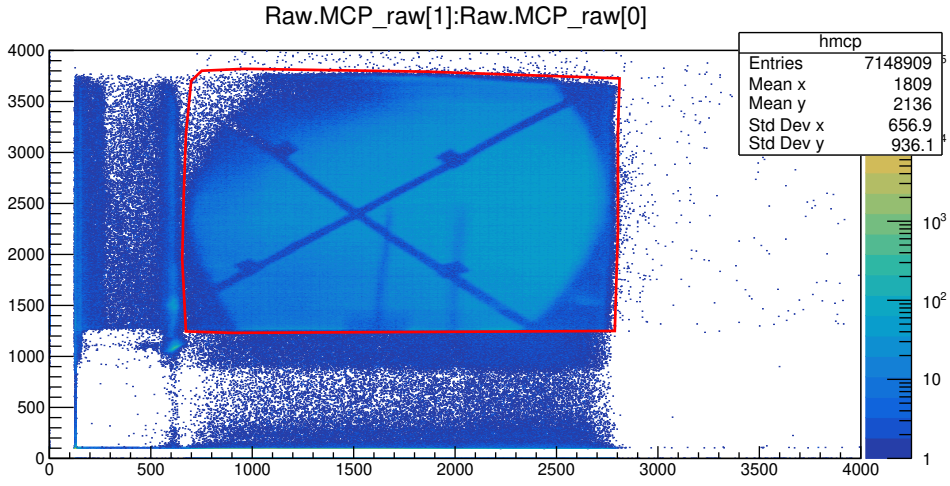

Figure B.1: X-Y matrix for the MCP raw data. The shadows from the metallic stripes and from the two screws are visible.

The MCP is the first subdetector of PRISMA that comes into play. A proper

calibration is crucial for a good trajectory reconstruction. After gating to cut the noise (Fig. B.1), the procedure consists in applying a series of transformations, summarized in Eq. (B.1), (B.2) and (B.3), done using some reference points, reported in Tab. B.1.

$$\begin{pmatrix} X' \\ Y' \end{pmatrix} = \begin{pmatrix} x_0 & x_1 \\ y_0 & y_1 \end{pmatrix} \begin{pmatrix} X_{raw} \\ Y_{raw} \end{pmatrix} \tag{B.1}$$

$$\begin{cases} X'' = a + bX' + c(X')^2 \\ Y'' = d + eY' \end{cases} \tag{B.2}$$

$$\begin{pmatrix} X_f \\ Y_f \end{pmatrix} = \begin{pmatrix} \cos\theta & \sin\theta \\ -\sin\theta & \cos\theta \end{pmatrix} \begin{pmatrix} X'' \\ Y'' \end{pmatrix} \tag{B.3}$$

Position	X (mm)	Y (mm)
Center	0.0	0.0
Top Left	-21.5	+26.5
Top Right	+21.5	+26.5
Bottom Left	-21.5	-26.5
Bottom Right	+21.5	-26.5

Table B.1: MCP calibration reference points.

In order to extract the calibration parameters, a minimization of the sum of squared residues is performed (Eq. (B.4)).

$$S = \sum_{i=1}^{N} [(X_f - X_{ref})^2 + (Y_f - Y_{ref})^2] \tag{B.4}$$

The result is shown in Chapter 3, Fig. 3.1.

B.2 MWPPAC

The signals from the MWPPAC are time signals: the time difference between left and right ends gives the position on the X axis, and the same happens for the Y direction. In particular, the focal plane position is given by

$$X_{fp} = X_r - X_l \tag{B.5}$$

For the calibration, some thresholds have to be set in the raw spectra (Fig. B.2, B.3 and B.4 respectively for the cathode signal, the left signal and the right signal) and then the focal plane coordinate X_{fp} must be adjusted in order to fit in the MWPPAC subdivision. In other words, the spectrum of each section must be calibrated in order to go from the left to the right end of the section itself, i.e. section 1 from 0 to 100 mm, section 2 from 100 to 200 mm and so on. In Fig. B.5 the plots for this calibration are shown: the red lines indicate the limits of each section. In Fig. 3.2 an example of events distribution in the focal plane is shown: the spikes in the middle of each subdivision work as reference.

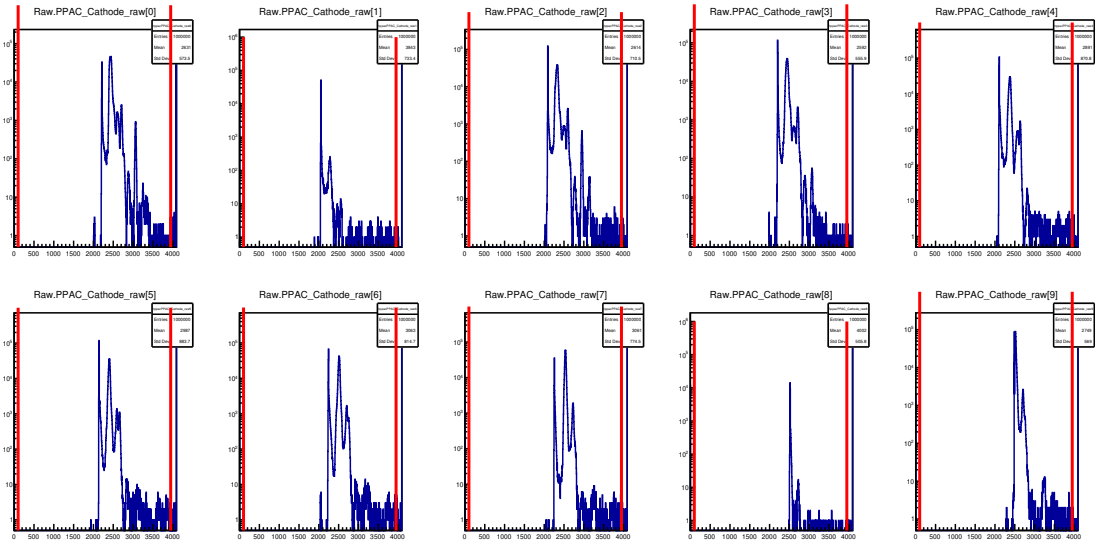

Figure B.2: Raw signal from the MWPPAC cathode with related thresholds.

There can be overflow and underflow in the data acquisition, and also attenuation along the MWPPAC can lead to missing X signals; in this case, the reconstruction

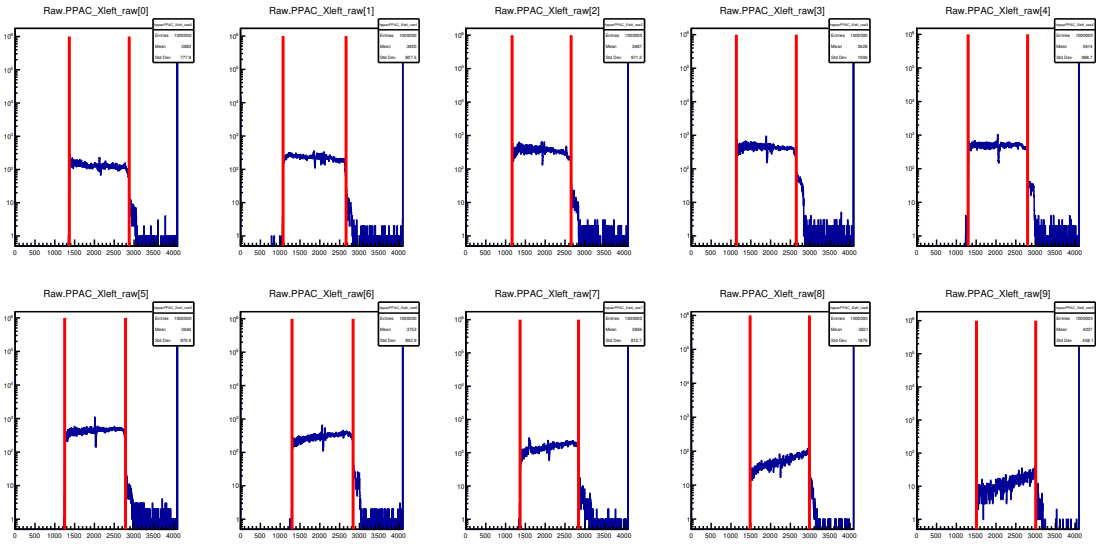

Figure B.3: Raw "left" signal from the MWPPAC anode with related thresholds.

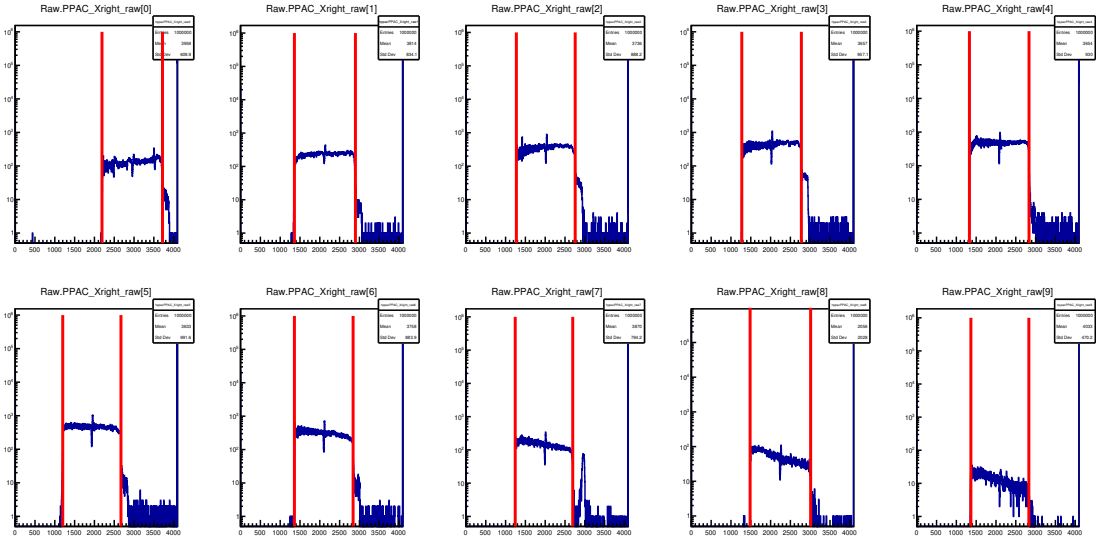

Figure B.4: Raw "right" signal from the MWPPAC anode with related thresholds.

is done using the cathode signal to recover the position without losing too much statistics. A calibration is therefore done also for the quantities

$$X_r - cath \qquad cath - X_l \tag{B.6}$$

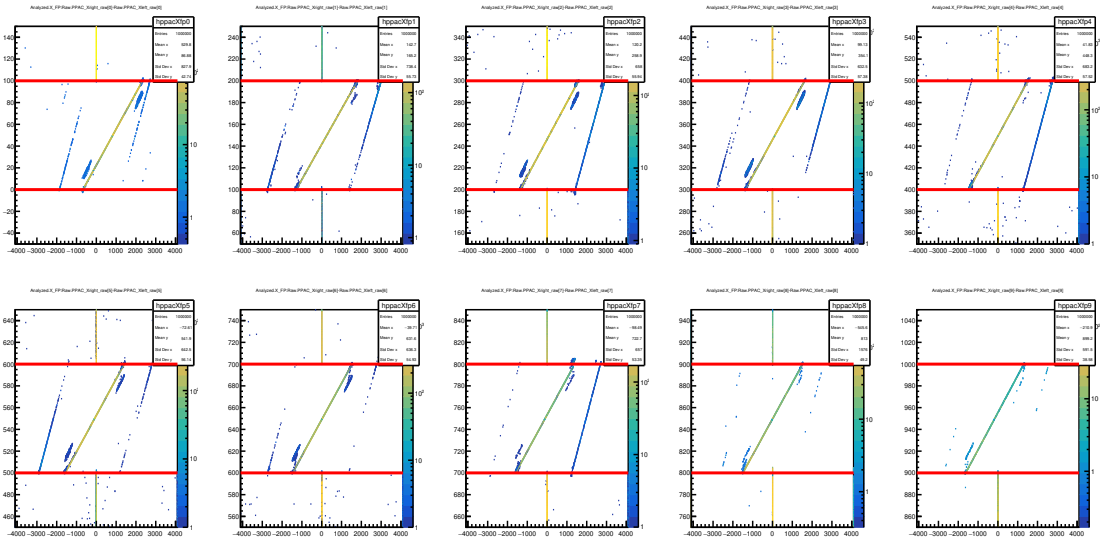

Figure B.5: Focal plane coordinate plotted as a function of the difference $X_r - X_l$. The red lines represent the dimensions of each section in the MWPPAC.

and a graphical gate is applied to the $X_l + X_r$ vs cathode (Fig B.6): in principle, this plot should present a single point, since the cathode is the trigger of the acquisition and the width of the MWPPAC ($X_l + X_r$) is fixed, but in reality the signal are not δ-function-like and there is a small dependency between the two quantities, in addition to the aforementioned overflow and underflow.

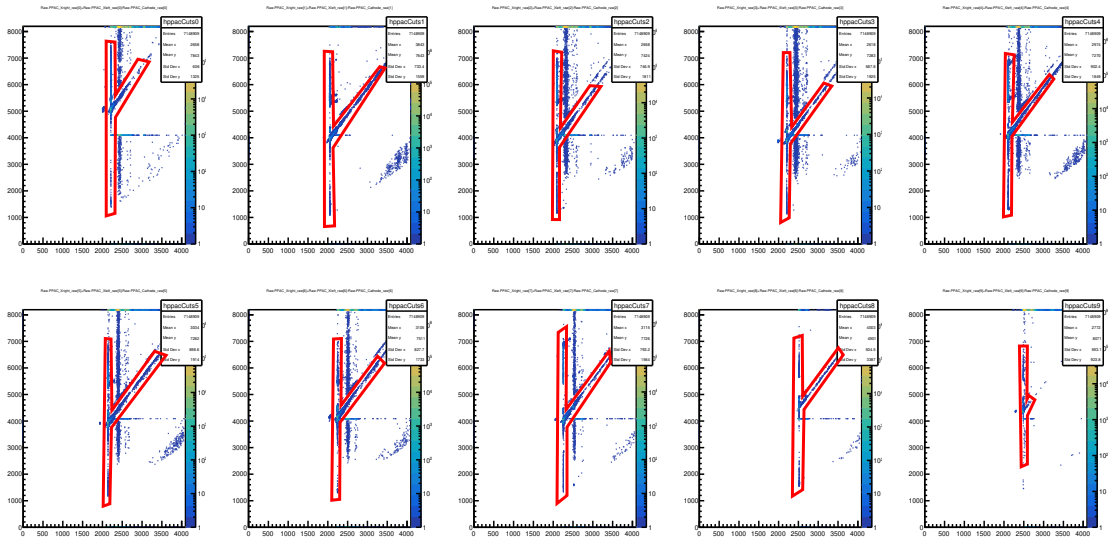

Figure B.6: Raw "left + right" signal from the MWPPAC anode vs raw cathode signal, with related graphical gates.

B.3 IC

In the following, the raw signals from the ionization chamber pads are presented: the side pads in Fig. B.7 and the other electrodes in Fig. B.8, B.9, B.10 and B.11 for row from A to D respectively (see Fig. 2.6 in Chapter 2 for reference).

During the analysis, we noticed an anomalous peak in section C left side pad and section C column 1 pad (Fig. B.12). This spike could be due to the presence of a broken pad (section C column 0): one possible explanation is that the electrons generated by the ionization of the gas are not collected by the broken pad and instead they produce a signal in the neighbouring C1 pad. Anyway, gating only on that peak, we could exclude some noise data, as shown in Fig. B.13: indeed the black points created an anomalous structure at lower energy, similar to a repetition of the real structure (coloured).

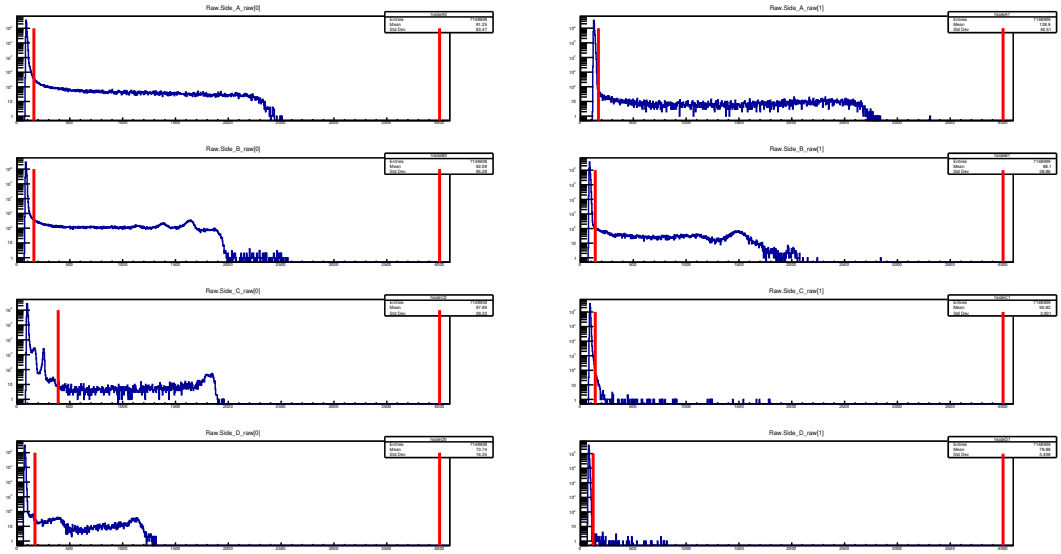

Figure B.7: IC side pads raw signals with related thresholds.

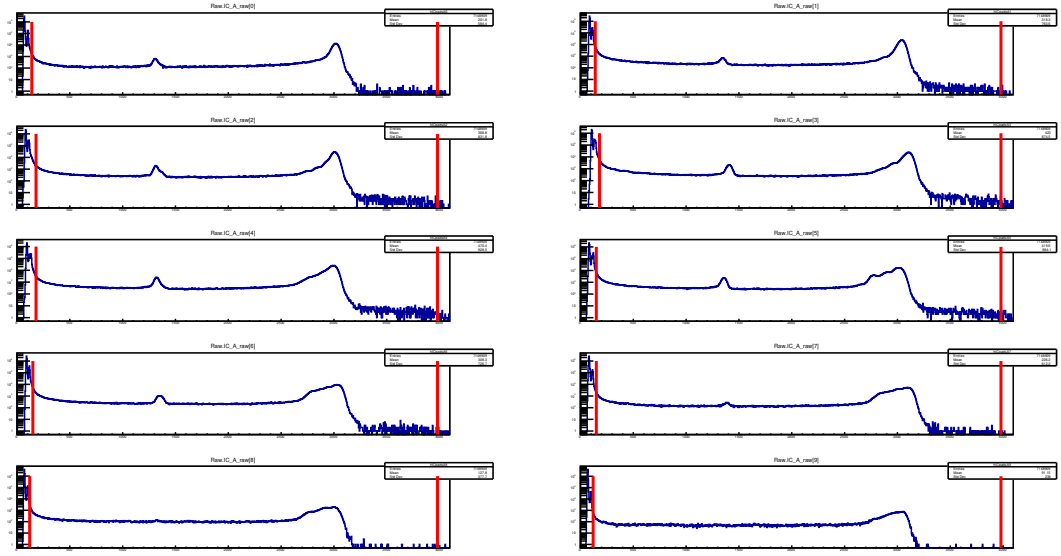

Figure B.8: IC pads signals for row A with related thresholds.

B.4 TOF

For what concerns the Time Of Flight, the raw signals are checked in order to see possible anomalies and to set very wide thresholds, as shown in Fig. B.14.

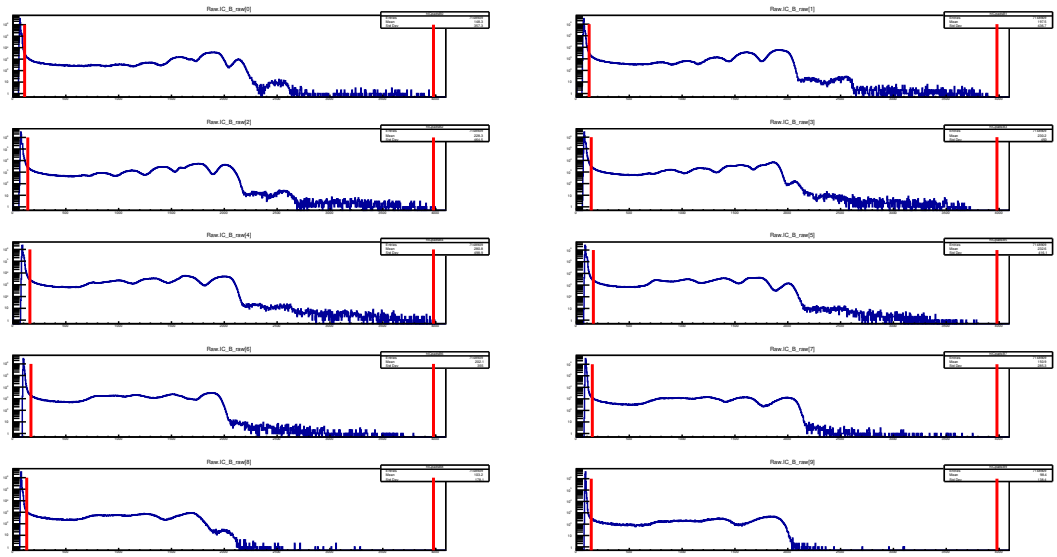

Figure B.9: IC pads signals for row B with related thresholds.

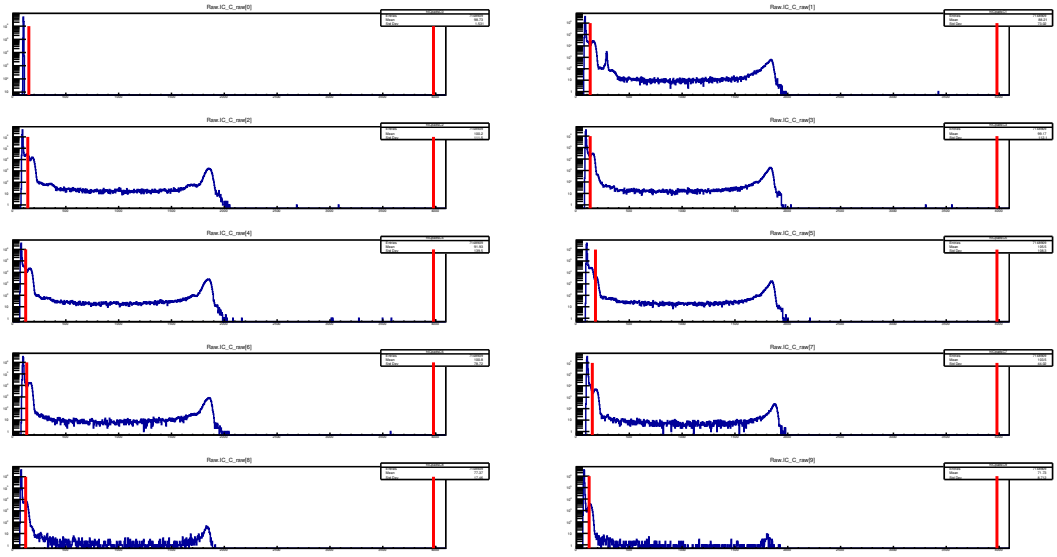

Figure B.10: IC pads signals for row C with related thresholds.

B.5 Optical parameters optimization

The optical parameters are important in the trajectory reconstruction, since they determine the curvature radius of the particle and therefore the path the ion travelled, from which the velocity is extracted. The algorithm that reconstructs the

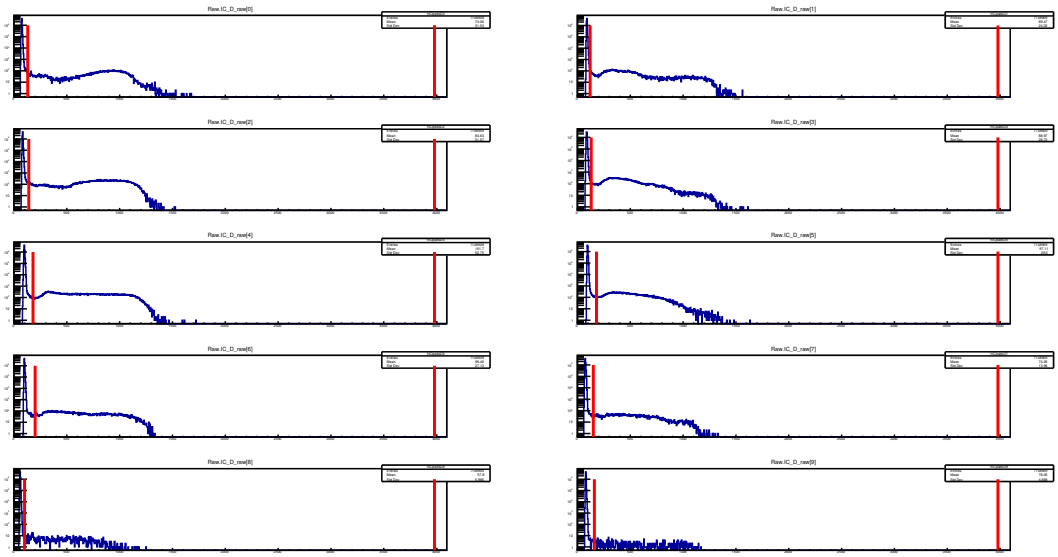

Figure B.11: IC pads signals for row D with related thresholds.

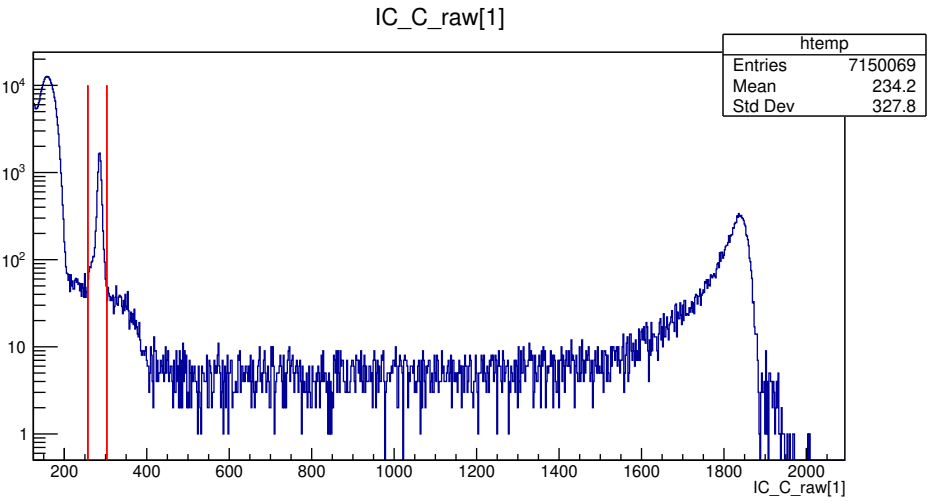

Figure B.12: IC row C pad 1 with anomalous peak.

particle trajectory is based on a mathematical model which contains those parameters as "effective" dimensions, since a perfect description of all the optical elements (dipole and quadrupole with their magnetic fields) is not available.

The presence of these effective parameters gives room for a possible optimization. Varying the value of a couple of them, some better results can be found in terms of linearization of the A/q-X_{fp} structures and therefore better resolution can be

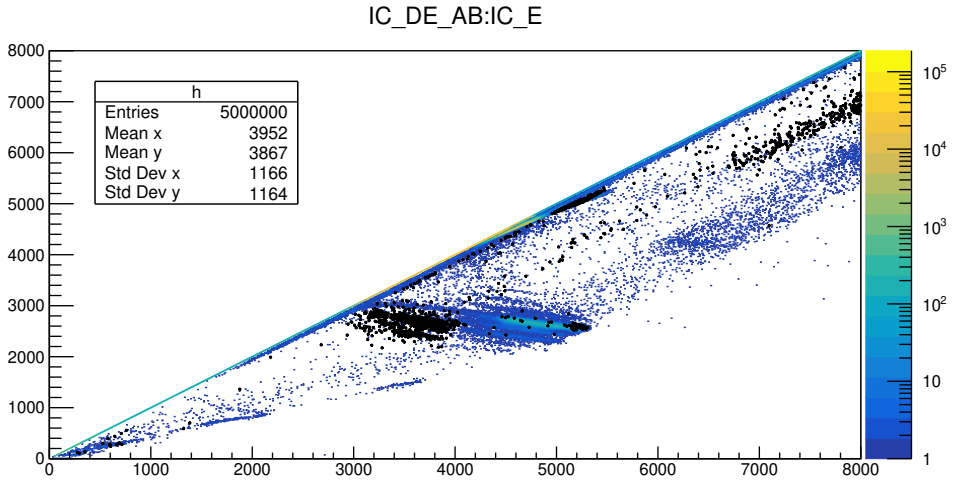

Figure B.13: ΔE-E matrix with anomalous-peak data in black.

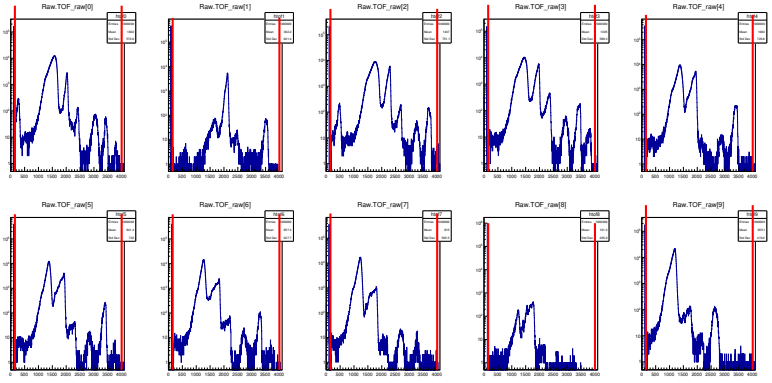

Figure B.14: Raw TOF signal with related thresholds.

achieved. In the following, the optimization procedure, which consisted of a systematic scan of values for the target-to-quadrupole effective distance d_{tq} and the effective quadrupole length l_q, is shown by mean of Fig. B.15, B.16 and B.17. The parameters obtained from the optimization are $d_{tq} = 470$ mm and $l_q = 410$ mm.

B.6 Aberration correction

Some aberrations are visible in the matrices where the A/q quantity is shown as a function of the MCP positions X and Y (Fig. B.18 and B.19, top). In particular,

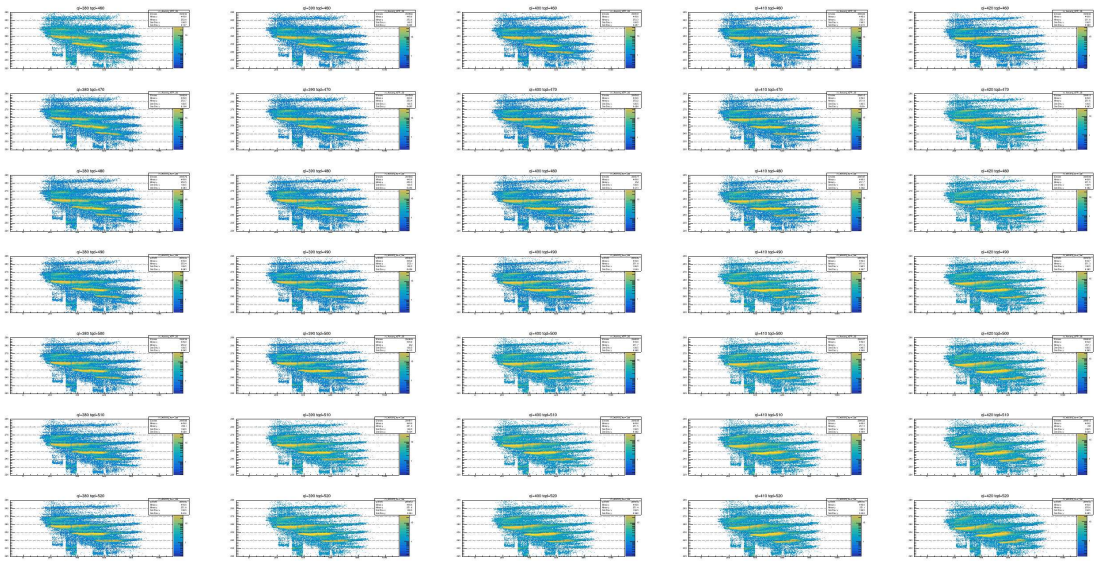

Figure B.15: Plot of A/q vs X_{fp} varying the target-to-quadrupole effective distance and the effective quadrupole length.

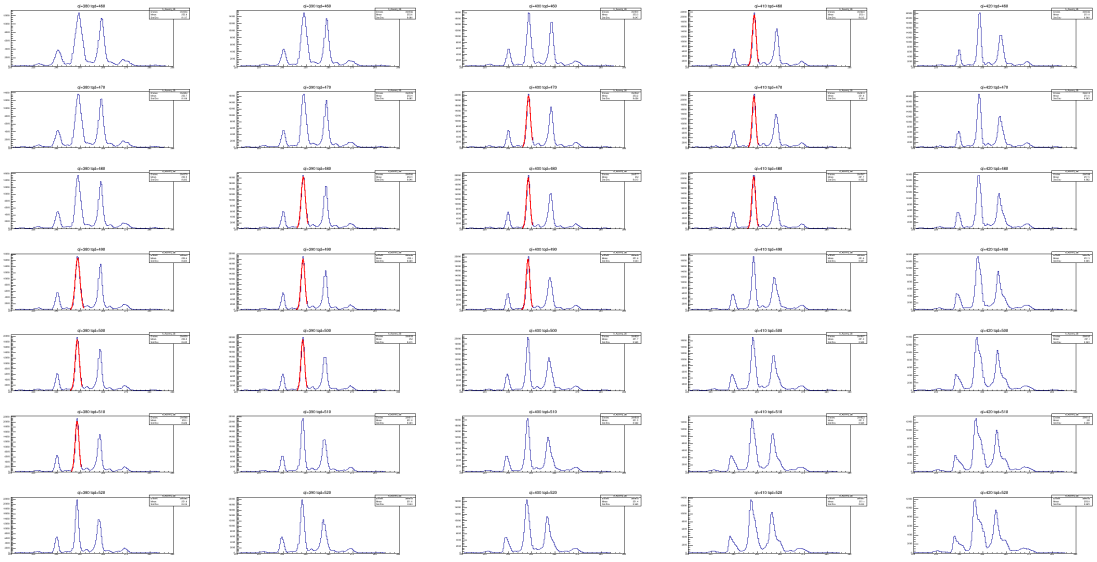

Figure B.16: A/q projection and fit for the optical parameter optimization.

since the A/q spectrum is nothing but the result of the projections of these two graphs, the aberrations can lead to tails and deformations of the peak shape. It is therefore necessary to correct these aberrations in order to improve the final mass resolution. By using polynomial fits, namely 5^{th} order in the X dimension and

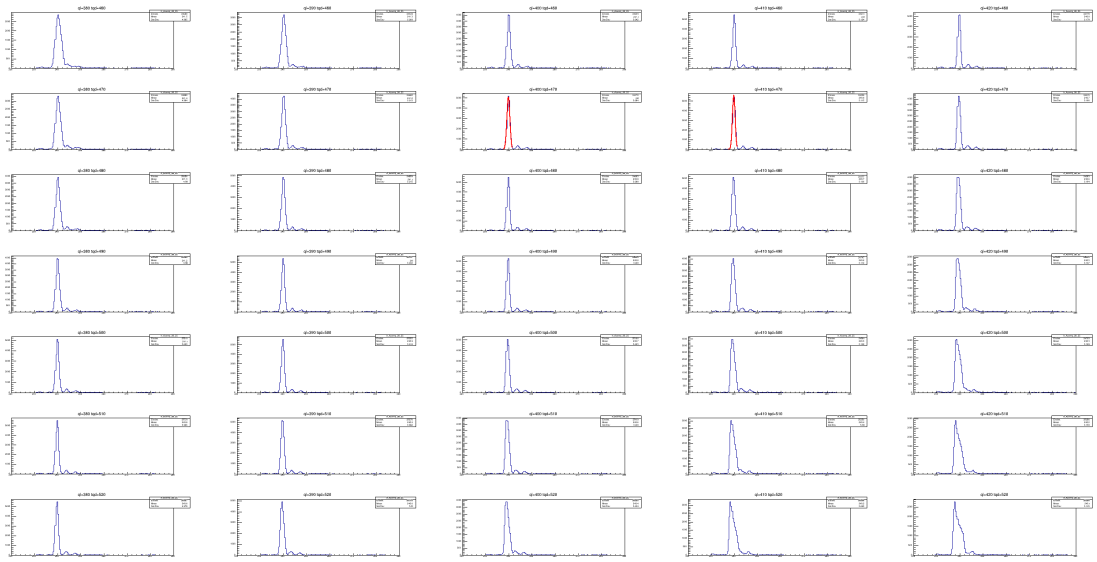

Figure B.17: A/q projection, gated on $Z = 28$, and fit for the optical parameter optimization to choose the best configuration.

2^{nd} order in the Y dimension, the A/q structures have been aligned, as shown in Fig. B.18 and B.19, bottom. In particular, these polynomials were subtracted to the data distribution in order to make them lay on a straight line. To be more precise, a perfect alignment in the MCP X variable could be done only applying the correction Z by Z and q by q, since the behaviour of the right tale changes. For the purposes of this thesis, a "first order" correction, meaning a single correction for all the Z, is sufficient.

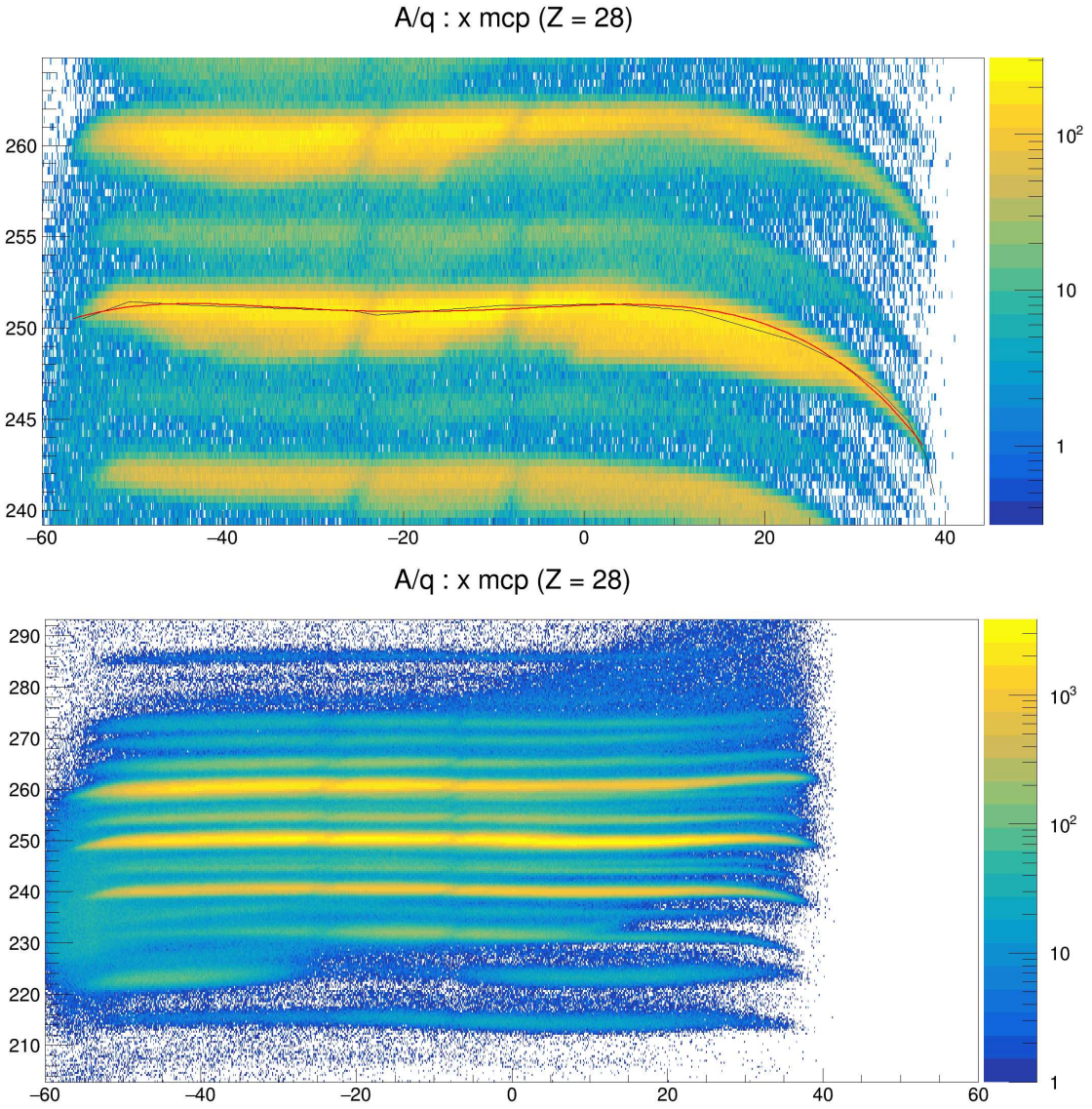

Figure B.18: Aberration correction for the A/q vs X_{mcp}: original distribution (top) and corrected distribution (bottom).

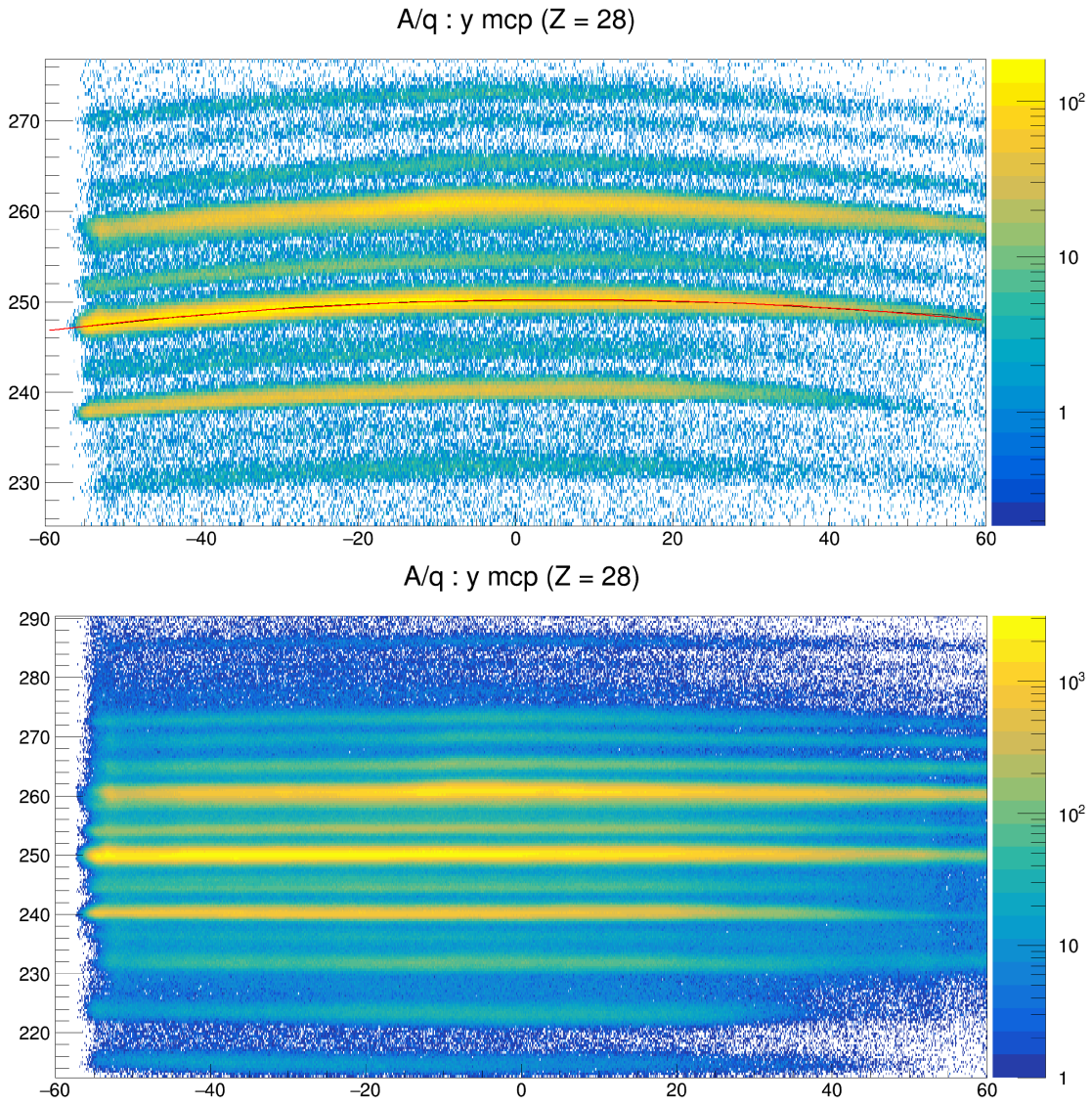

Figure B.19: Aberration correction for the A/q vs Y_{mcp}: original distribution (top) and corrected distribution (bottom).